

Monte Carlo Modelling of an Orthovoltage X-ray System Using Multiple Applications in EGSnrc

by

Dinindu B. Gunasekara

A thesis submitted to the Faculty of Graduate and Postdoctoral Affairs in partial fulfillment of the requirements for the degree of

Master of Science

in

Physics (Medical)

Carleton University

Ottawa, Ontario

© 2022

Dinindu B. Gunasekara

Abstract

Biodosimetry relies on calibration curves to convert biological damage induced by ionizing radiation to an absorbed dose. Health Canada generates these curves by irradiating biological samples with X-rays, though exposures scenarios could consist of other types of radiation which are challenging to replicate in the laboratory. The ultimate goal of this work is to model the X-ray setup using Monte Carlo methods and to validate the model using in-laboratory measurements. The model was iterated through preliminary and final testing phases in different EGSnrc applications (egs++, SpekPy and BEAMnrc) and optimized using variance reduction techniques, resulting in multiple models. The X-ray spectra produced from each model were compared and found to be equivalent. Model outputs were also compared against laboratory measurements to identify the most accurate model. The final model output will be used in the next phase of the project to model radiobiological damage.

Acknowledgements

I would like to express my deepest appreciation to my supervisor Dr. Lindsay Beaton-Green who has supported me throughout the project and taught me a lot along the way. I am also grateful for Dr. Ruth Wilkins who has basically been my co-supervisor through the project, always filling in for Lindsay when needed and always being ready to provide helpful feedback. Thank you to everyone else at the Health Canada lab as well for providing such a warm welcoming environment.

This project would not have been possible without the help of Dr. Frédéric Tessier who offered hours upon hours of his time to meet with me virtually and discuss anything and everything about EGSnrc. Thanks should also go to Dr. Ernesto Mainegra-Hing for his explanations and recommendations regarding EGSnrc applications, and providing helpful examples.

Many thanks to all of the individuals at the Carleton Laboratory for Radiotherapy Physics including Dr. Dave Rogers, Dr. Martin Martinov, Michael Thibodeau and several others for their helpful discourse and suggestions on my project. In addition, thanks to the excellent professors at Carleton including Dr. Paul Johns and Dr. Rowan Thomson for teaching me many things that I was able to apply in this thesis.

Finally, I would like to thank my family and friends, especially my parents, for supporting me throughout this degree. Last but certainly not least, I would like to thank my girlfriend, Hiruni Senarath, for believing in me and for her endless love and support throughout this endeavour.

Table of Contents

Abstract.....	ii
Acknowledgements	iii
Table of Contents.....	iv
List of Tables	vii
List of Figures	viii
List of Acronyms.....	x
1. Introduction.....	1
1.1. Basics of Biodosimetry	1
1.1.1. Why biodosimetry?	2
1.1.2. Dose Calibration for Biodosimetry Assays.....	3
1.2. Different Radiation Exposure Environments	7
1.2.1. Space Radiation	7
1.2.2. Accidental Exposures and Emergency Scenarios.....	9
1.2.3. Laboratory-based Environment.....	10
1.3. Monte Carlo Modelling with EGSnrc	11
1.3.1. Applications within EGSnrc.....	13
1.3.1.1. egs_chamber	13
1.3.1.2. BEAMnrc	16
1.3.2. Variance Reduction Techniques.....	18
1.3.2.1. Range-based Russian Roulette	21
1.3.2.2. Photon Cross Section Enhancement	23
1.3.2.3. Bremsstrahlung Splitting.....	24
1.3.2.4. Directional Bremsstrahlung Splitting	25
1.3.2.5. Bremsstrahlung Cross Section Enhancement.....	26
1.4. Thesis Statement.....	28
2. Materials and Methods	29
2.1. Health Canada’s Experimental Setup for Blood Irradiation	29
2.1.1. XRAD-320	29

2.1.2.	PTW 30010 Ionization Chamber.....	33
2.1.3.	Solid Water-Equivalent Phantoms.....	36
2.1.3.1.	Single-slot Phantom.....	36
2.1.3.2.	Multi-slot Phantom.....	37
2.1.4.	Setup Error Estimation	39
2.2.	Monte Carlo Modelling through EGSnrc.....	42
2.2.1.	Three Models.....	42
2.2.1.1.	egs++ Model.....	44
2.2.1.2.	SpekPy Model.....	47
2.2.1.3.	BEAMnrc Model	50
2.3.	Implemented Variance Reduction Techniques.....	52
2.3.1.	egs_chamber VRTs.....	53
2.3.1.1.	Range-based Russian Roulette (RR).....	54
2.3.1.2.	Photon Cross Section Enhancement (XCSE).....	55
2.3.1.3.	Bremsstrahlung Splitting.....	56
2.3.2.	BEAMnrc VRTs.....	57
2.3.2.1.	Directional Bremsstrahlung Splitting (DBS) and Bremsstrahlung Cross Section Enhancement (BCSE).....	58
2.4.	Procedures for Model Validation.....	59
2.4.1.	Spectral Comparison.....	60
2.4.2.	Phantom & Filter Comparison.....	62
2.4.3.	HVL Validation	64
3.	Results.....	65
3.1.	Code Optimization Results	65
3.1.1.	Range-based Russian Roulette (RR).....	65
3.1.2.	Photon Cross Section Enhancement (XCSE)	68
3.1.3.	Bremsstrahlung Splitting	70
3.1.4.	Directional Bremsstrahlung Splitting (DBS) combined with Bremsstrahlung Cross Section Enhancement (BCSE).....	72
3.1.5.	Summary of Optimal VRT Parameters.....	74
3.2.	Inter-model Comparison.....	75
3.2.1.	Spectral comparison.....	75
3.3.	Validating Models with Laboratory Results.....	79

3.3.1.	Setup Error Estimation	79
3.3.2.	Phantom Comparison.....	82
3.3.3.	Filter Comparison	83
3.3.4.	HVL Comparison.....	85
4.	Discussion	86
4.1.	Choosing Variance Reduction Parameters.....	86
4.1.1.	Range-based RR and XCSE	87
4.1.2.	Bremsstrahlung Splitting	89
4.1.3.	DBS and BSCE.....	91
4.1.4.	Optimized Models.....	92
4.2.	Spectral Comparison between Models	93
4.3.	Model Validation	95
4.3.1.	Phantom Comparison.....	97
4.3.2.	Filter Comparison	98
4.3.3.	Half-Value Layer (HVL) Comparison.....	100
5.	Conclusion	101
5.1.	The Best Model.....	101
5.2.	Future Work	101
6.	References	103

List of Tables

Table 1: List of materials used in EGSnrc simulations.....	47
Table 2: Summary of VRT analysis.....	75

List of Figures

Figure 1: Examples of chromosome aberrations identified in DCA and FISH	5
Figure 2: Example of dose calibration curves gathered at Health Canada.....	6
Figure 3: Images of some of the windows from the BEAMnrc GUI	18
Figure 4: Picture of the inside of the XRAD-320 cabinet.....	32
Figure 5: Schematic diagram of the X-ray machine shown in Figure 4.....	33
Figure 6: Image of the PTW 30010 ionization chamber	35
Figure 7: Images of the phantoms used to hold either the ionization chamber or blood vials for irradiation	38
Figure 8: Schematic drawing of the multi-slot phantom.....	39
Figure 9: Flowchart for creation and testing of XRAD-320 model in three different ways using applications in EGSnrc.	44
Figure 10: Partial view of the egs++ model produced using egs_view.	46
Figure 11: Example code for producing a spectrum through SpekPy.....	49
Figure 12: Schematic of the BEAMnrc model visualized using the BEAMnrc GUI	51
Figure 13: Solid water phantoms created in EGSnrc using egs++ geometry.....	63
Figure 14: Results from the preliminary phase of optimizing range-based RR	67
Figure 15: Large values for the rejection factor plotted for preliminary phase.....	67
Figure 16: Results from the final phase of optimizing range-based RR.	68
Figure 17: Large values for the rejection factor plotted for the final phase	68
Figure 18: Results from the preliminary phase of optimizing XCSE.....	69
Figure 19: Results from the final phase of optimizing XCSE.	70
Figure 20: Results from the preliminary phase of optimizing brems. splitting.....	71
Figure 21: Results from the final phase of optimizing brems. splitting	72

Figure 22: Results from optimizing the DBS combined with BCSE.....	73
Figure 23: Comparing spectra produced by all three models with only the MXR-321 simulated in vacuum at 250 kV	76
Figure 24: Comparing spectra produced by all three models with only the MXR-321 X-ray tube simulated in vacuum at 200 kV	77
Figure 25: Comparing spectra produced by all three models with only the MXR-321 X-ray tube simulated in vacuum at 300 kV	77
Figure 26: Comparison of spectra produced by each model for the full XRAD-320 simulated with Filter 1 in place.	77
Figure 27: Comparison of spectra produced by each model for the full XRAD-320 simulated with Filter 2 in place.	78
Figure 28: Comparison of spectra produced by each model for the full XRAD-320 simulated with Filter 3 in place	78
Figure 29: Estimation of the error contribution from setting the source-to-surface distance using a linear fit.....	81
Figure 30: Estimation of error contribution from setting field size using a linear fit.....	81
Figure 31: Validation results for phantom comparison.....	83
Figure 32: Percentage difference between simulations and laboratory measurements for three filters normalized to the output with no filter in place.....	84
Figure 33: Attenuation curve plotted for copper	85

List of Acronyms

ARS	Acute Radiation Syndrome
AETT	Approximate Efficiency Improvement Technique
CMs	Component modules
BCSE	Bremsstrahlung Cross Section Enhancement
DCA	Dicentric Chromosome Assay
DBS	Directional Bremsstrahlung Splitting
ECUT	Electron cutoff energy
EGS	Electron Gamma Shower
FAC	Free Air Chamber
FISH	Fluorescent In-Situ Hybridization
GCRs	Galactic Cosmic Rays
GUI	Graphical User Interface
HVL	Half-Value Layer
ISS	International Space Station
LET	Linear Energy Transfer
MC	Monte Carlo
MFP	Mean Free Path
NRC	National Research Council
PBLs	Peripheral Blood Lymphocytes
RR	Russian Roulette
SPEs	Solar particle events
SSD	Source-to-Surface Distance
TLD	Thermoluminescent dosimeter
VRTs	Variance Reduction Techniques
XCSE	Photon Cross Section Enhancement

1. Introduction

1.1. Basics of Biodosimetry

Radiation can be encountered in many facets of everyday life, ranging from food sources to the light emitted from the Sun. It can be classified into non-ionizing and ionizing radiation where exposure to the former is relatively harmless but being exposed to the latter can lead to adverse health effects in human beings. The key difference is that ionizing radiation carries enough energy to cause ionization of the atoms it interacts with, resulting in the production of free radicals that can then adversely effect the body. Free radicals refer to ionized atoms or molecules formed mainly through reactions involving water and the majority of damage caused by irradiation is through these particles. There are several mechanisms that govern how radiation will interact with biological matter, but the most important concept to consider when looking at biological effects is the damage sustained by the genetic material of irradiated cells. Incoming radiation can cause breaks in the double-helix structure of DNA [1] molecules within chromosomes and, based on how the chromosome is joined back together, this can lead to the production of different types of aberrations within this genetic material. The resulting damage could either be lethal to the cell and cause cell death, referred to as unstable damage, or leave the cell functions intact, allowing it to continue dividing and pass on the damage to its daughter cells, called stable damage [2]. This type of distinction is important when considering biological damage to genetic material as a biomarker for radiation dose absorbed. In this context, absorbed radiation dose refers to the amount of energy deposited by an incoming beam of ionizing radiation in the irradiated volume, typically measured in Gray (Gy).

Biodosimetry is a technique that quantifies the level of biological damage in an individual and converts this to an amount of dose absorbed by that individual. In broad terms, by correlating the number of chromosome aberrations produced after irradiation to the radiation dose used to produce that damage, one can determine an unknown dose to which an individual was exposed.

1.1.1. Why biodosimetry?

At the whole organism level, DNA damage will lead to cell damage that manifests in the form of Acute Radiation Syndrome (ARS) within human beings. The severity of ARS increases as the dose absorbed increases, with symptoms ranging from nausea and vomiting at low doses, all the way to strongly affected cerebral function and death in the worst of cases [3]. In addition to the short-term symptoms of ARS, exposure to ionizing radiation can result in more chronic illnesses, such as cancer and cardiovascular diseases. Proper clinical management of an individual exposed to any amount of radiation is highly dependent on quantifying the exposed dose [3], [4].

There are several ways of assessing radiation dose, but two main ways through the use of a physical dose measurement device (dosimeter), or through biodosimetry. One example of a physical dosimeter is a thermoluminescent dosimeter (TLD), which is constructed of a crystal that emits light when exposed ionizing radiation in a predictable way [5]. This light can be measured and used to quantify the dose absorbed. TLDs are typically worn in the form of badges and worn over a set period of time by nuclear energy workers, who are required to work near sources of ionizing radiation, to monitor their exposure to avoid it reaching unsafe levels. These devices provide a good idea of the level of hazard a radiation environment poses to a human being but do not consider the biological response of that individual. Therefore,

one cannot truly determine the best course of clinical action for an individual with physical dosimetry alone. It is not sufficient to quantify the amount of radiation present in one's environment, the actual damage sustained by the individual needs to be quantified to assess potential medical impact. Biodosimetry is able to fill in these gaps in physical dosimetry by taking into account factors specific to an individual, such as their inherent level of radiosensitivity and the varying degrees of shielding they could have had during the exposure [6].

1.1.2. Dose Calibration for Biodosimetry Assays

There are many types of biological damage that can be explored for use in a biodosimetry assay, each having their own advantages and disadvantages when used for this application. In addition, whether the damage is stable or not will affect the timing window in which the technique is effective. One well-studied target for biodosimetry assays are the chromosomes found within peripheral blood lymphocytes (PBLs), as they have been found to act as good biomarkers for ionizing radiation damage. In particular, dicentric chromosome aberrations are a type of unstable DNA damage found in PBLs that involve the interchange between two separate chromosomes that have sustained a break. When the pieces of each chromosome attempt to rejoin, they may rejoin with the piece of the other chromosome creating distorted chromosome with two centromeres (called a dicentric, an example of which be seen in the bottom left image of **Figure 1**) and an acentric fragment. These dicentrics can be identified and counted to quantify the dose received by the individual exposed. This assay is called the Dicentric Chromosome Assay (DCA) and it is currently the gold standard for biodosimetry [5], [7]–[12] as it is accurate, reliable, specific to ionizing radiation. Notably, the background levels of dicentrics are very low, making it more likely that changes in dicentric

frequency originate from exposure to ionizing radiation. Some limitations include that dicentric aberrations are not passed on to progeny during cell proliferation, restricting the technique to a specific time window, and it is very time-consuming and labour-intensive with the whole process taking several days from receiving the sample to getting a dose estimate. Notably, through the continued research in this field and the development of processes such as DCA QuickScan scoring [13] and automated DCA analysis [14] these limitations can be minimized. Alternatively, a stable chromosome aberration could be used for an assay, providing a less strict time window in which a sample can be analyzed. One such example is another common biodosimetry assay called translocation analysis using Fluorescent In Situ Hybridization (FISH) assay [5], [8], [15]–[18]. This technique relies on quantifying chromosome translocations, which involve a broken end of a chromosome attaching itself to another chromosome (or sometimes an exchange of broken ends between two chromosomes), resulting in chromosomes that can appear morphologically correct, having only one centromere. To identify aberrations, the chromosomes of interest are “painted” using various techniques as seen in the right side of **Figure 1**. Since this form of DNA damage is stable, the FISH assay’s main advantage is its capability to do retrospective dose assessments for years after exposure. This assay also comes with its own set of disadvantages including not being as specific as DCA to ionizing radiation and having a larger variation in background levels than DCA.

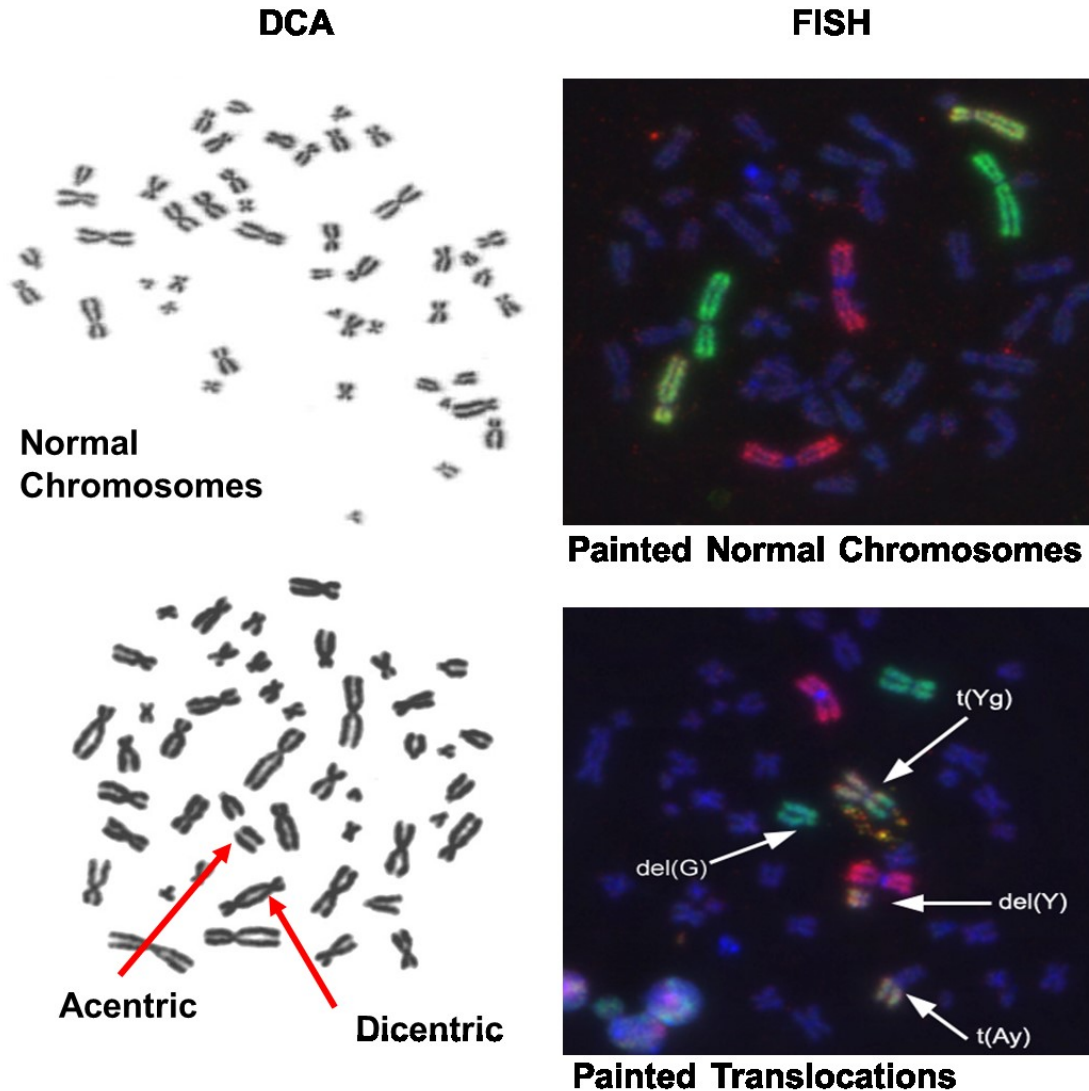


Figure 1: For DCA (left side), dicentric chromosomes (dicentric) and a paired acentric fragment (ace) are morphologically different from normal chromosomes so they can be counted to find absorbed dose. For FISH (right side), apparently stable chromosome translocations result in normal looking chromosomes so they must be “painted” to identify aberrations. In this example, chromosomes 1 (red), 2 (green) and 4 (yellow) are painted, and example damage includes deletions (del(G) and del(Y), and translocations (t(Yg) and t(Ay)). Images from Health Canada.

Both examples of assays provided, as well as many other biodosimetry assays require calibration to convert biological damage to a dose estimate. In broad terms, the basic operating principle of any biodosimetry assay is to quantify biological damage through irradiation of a biological sample to a range of doses and use the biological damage scored to plot a means of correlating damage to dose. Therefore, accurate dose calibration curves are essential for the

success of any of the biodosimetry methods. Several factors can affect a calibration curve for a given technique, ranging from the type of radiation used to the individual's inherent radiosensitivity. Typically, a dose calibration curve takes the form of a linear quadratic curve for low linear energy transfer (LET) radiation types like X-rays, given by the following Equation (1) seen below [8], [9].

$$Y = \alpha D^2 + \beta D + C \quad (1)$$

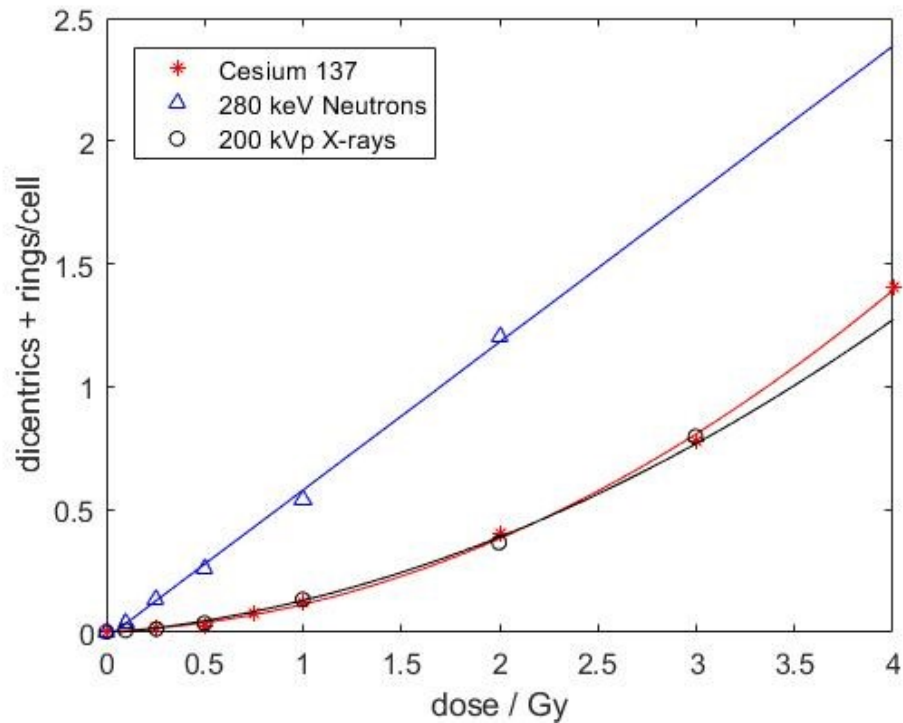


Figure 2: Example of dose calibration curves to showcase the variation in the curves between different radiation types for the biodosimetry technique DCA. Data gathered at Health Canada. Error bars not shown.

An example of such a curve for DCA is shown in **Figure 2** for several types of radiation. When considering more damaging types of radiation like alpha particles or neutrons, the curve can move towards linearity. The two constants in Equation (1), α and β , have been found to be influenced by a variety of factors including the type of ionizing radiation, the dose rate, energy, and exposure conditions [9]. Therefore, when developing a dose calibration curve

for a given biodosimetry assay, these factors must be taken into consideration as a correct estimation of this curve is important to receiving an accurate dose output from the technique.

1.2. Different Radiation Exposure Environments

In determining clinical endpoints for radiation exposures, it is important to consider that most instances of radiation exposure are unique. From the types and energies of ionizing radiation involved, to the way those doses are deposited in the individuals involved, each exposure situation must be assessed on its own. In addition, one must consider the difference between dealing with individual or population biodosimetry, as they have unique priorities when assessing biological damage. Aside from occupational and medical exposures, some examples of environments where one could potentially be exposed to ionizing radiation, or encounter ionizing radiation in general, include in outer space or in an accidental or malicious nuclear emergency. These are extreme scenarios but due to the complexity of the radiation involved, the amount of radiation involved, and the duration which these individuals would be exposed to this radiation, these environments are the overall focus of this project.

1.2.1. Space Radiation

Astronauts are exposed to an extremely complex radiation environment when traveling to the International Space Station (ISS) or beyond. Due to the lack of the protection from the Earth's atmosphere and magnetic field, sources of radiation that would otherwise not be a concern on the ground pose a real threat. The first step in assessing the health effects of an exposure to space radiation is to quantify the radiation environment and study its effects through experimentation and simulation. The characterization of space radiation is also important when considering the effect it has on the electronics on board the spacecraft. Many different types of radiation originating from the sun compose the environment seen in low-

Earth orbit and beyond. It is typically dominated by trapped particles in the Van Allen belts, galactic cosmic rays (GCRs), and solar particle events (SPEs) [19]. The Van Allen belts refer to “belts” of radiation trapped around the Earth by its magnetosphere and are composed mostly of protons and electrons. GCRs refer to the background radiation originating from far away sources and are composed of approximately 87% protons, 12% helium, and 1% heavy ions [20]. SPEs are emissions of particles during various ejection phenomena on the solar surface, with the flux being mainly composed of protons. In a paper recently published in 2020, Simonsen et al. [20] detail a complex radiobiological model of the incident radiation to critical organs of a human phantom in a deep space vehicle. They account for both the shielding provided by the spacecraft, as well as the inherent shielding provided by the body itself, with the presence of this shielding adding an extra degree of complexity. Various studies [21], [22] have been done into calculating the primary and secondary radiation, composed mostly of protons and light ions, from GCRs and SPEs interacting with the spacecraft.

With all this in mind, it is clear that the space radiation environment is complex with additional considerations required for the type of spacecraft involved, as well as the location in space. One important thing to note about space radiation is a continuous source of exposure and that cellular damage is sustained in space over a long period of time. So while various forms of physical dosimetry exist in places such as the ISS that can quantify this radiation, these devices cannot account for the complex mechanisms involved in the biological response to this protracted exposure. Physical dosimetry does not take into account biological processes such as the effects of cellular repair, prolonged stress, and microgravity. A more accurate way of estimating the effects of this complex dose is to use biological dosimetry. Assays like DCA and FISH are ideal for these scenarios, but the problem lies in producing a calibration curve that is representative of the space radiation astronauts are exposed to during their trips.

Optimally, the space radiation environment could be recreated in the laboratory to produce calibration data but this is not practical.

1.2.2. Accidental Exposures and Emergency Scenarios

Ionizing radiation exposure can occur through accidents or through intended nuclear incidents. These incidents can involve the general public being exposed in several different emergency scenarios [3], [4]. One example of such a threat are radiation dispersal devices, a conventional explosive device with some radioactive material attached to it that would cause harm to several individuals in the vicinity. The device could also just be a radiation emitting source placed in a high population area, which would instead be called a radiation exposure device, resulting in many people being exposed to unknown doses of ionizing radiation. Another larger scale example is an improvised nuclear device, a nuclear weapon that would kill thousands in the blast and irradiate many more in the fallout afterwards. In terms of accidents, one could consider the case of a critical mistake in a nuclear reactor, potentially causing an explosion of radioactive material that would be spread to the surrounding area.

Each of these events can involve different types of radiation based on the source involved and how individuals were exposed. The complexity of the radiation involved in the scenario, and the likelihood that physical dosimetry will not be available, mean that biodosimetry is optimal for dose assessment. The primary threat from most emergency scenarios is from X-rays and gamma rays, as they have the largest penetrating power compared to other types of radiation such as alpha and beta particles that would either not penetrate far enough into an individual to inflict significant damage. As previously discussed, the severity of the ARS resulting from this radiation exposure is highly dependent on the amount of radiation an individual was exposed to, so rapid biodosimetry to determine dose could be critical for clinical

management. For the purpose of dealing with large scale emergencies such as these, biodosimetry networks exist all over the world [23]. The key in conducting biodosimetry in these scenarios is speed. While the accuracy of the techniques is important as well, large scale disasters can involve thousands of people that require dose assessment and treatment, so having access to fast means of biodosimetry is important. More accurate dose estimates can be made with slower techniques after the disaster has successfully been handed. Just as mentioned for the case of space radiation, a calibration curve must be produced for these scenarios and because of the complexity of the radiation involved, it can be impractical to try to reproduce it in the laboratory to get an accurate calibration curve.

1.2.3. Laboratory-based Environment

As discussed in the previous sections, irradiation exposures in space, during nuclear accidents and nuclear incidents are complex. To use any biodosimetry technique for dose estimation, a calibration curve must be created. In most laboratories, one would use available equipment to produce these curves. For example, the biodosimetry program at Health Canada uses a cabinet X-ray machine to produce its dose calibration curves. Considering that the primary threat from large scale emergencies is from low LET radiation, this could very well be a sufficient approximation. It could also be the case that it is a sufficient approximation for space radiation with the correct shielding in place. Despite it being difficult and expensive, replicating the space environment in the laboratory is of great interest to space agencies across the world to assess the health effects to astronauts being exposed, as well as to test the radiation hardness of equipment used on these space missions [24]. Attempts have been made to replicate space radiation in the laboratory but in the past studies were done with single ion beams, but as detailed in the paper by Norbury et al. [25], technological improvements allow

us to move towards more and more complex laboratory sources. Notably, this is not without its own set of challenges.

In summation, these environments are far too complex to practically reproduce in the laboratory at Health Canada so other avenues must be explored to investigate the accuracy of generating a dose calibration curve using solely X-ray radiation. One useful way to do this is through the use of computational simulations. In particular, Monte Carlo simulations are a useful technique as they specialize in simulating random processes, like the transport of radiation through matter. Using a computational model of a complex radiation source, a calibration curve could be simulated from this complicated source and compared to the data gathered in the laboratory. This can be used to verify the efficacy of using the laboratory curve for the irradiation scenario, and if large discrepancies exist, provide a means of converting this laboratory calibration curve to a complex radiation equivalent curve.

1.3. Monte Carlo Modelling with EGSnrc

Computational modelling is useful when investigating situations that cannot feasibly be recreated in a laboratory environment, or as a point of validation for laboratory results. Monte Carlo (MC) modelling refers to the application of MC methods in computational algorithms to recreate scenarios that are inherently random in nature. MC codes are widely used for a variety radiation dosimetry purposes ranging from calculating simple quantities like perturbation factors, to fully modelling complex clinical scenarios [26]. In this context, a typical MC simulation involves the tracking of large numbers of particles, the initial number of which are called histories, through some user defined geometry. The interactions of these particles with matter are stochastic in nature, so the probability distributions that define the trajectories of these particles can be sampled using random numbers to generate the values required to

simulate transport. MC simulations have long been considered the “gold standard” for dose calculations in medical physics, and many software packages have been developed for the purpose of simulating various scenarios. One widely used example of such a software is EGSnrc [27], capable of simulating coupled electron-photon transport for particle energies ranging from 1 keV to 10 GeV. The code has a rich history with countless contributors with multiple iterations and improvements over the past few decades to get it to the place where it is today [28]–[31]. Its predecessor, Electron Gamma Shower (EGS), was developed by the National Research Council (NRC) of Canada, along with the Stanford Linear Accelerator Center, into what is now known as EGSnrc.

The underlying code for EGSnrc is written in an extension of the FORTRAN programming language called MORTRAN, more specifically Mortran3. There are several subroutines with the EGS code, but the two subroutines that can be called by the user are HATCH and SHOWER, which interact with further subroutines within the code. The HATCH subroutine initializes material data, and the SHOWER subroutine initiates a particle’s cascade through the user-defined system. To use EGSnrc code, a MAIN subroutine must be coded that can interact with the previous subroutines. In addition, there are three subroutines that must be written into the user code including HOWFAR, HOWNEAR, and AUSGAB. The first two specify the geometry involved in the simulation, while the last subroutine is used to record and output quantities of interest and control variance reduction [32]. To use EGSnrc in this fashion and write one’s own user code, a reasonable amount of knowledge of Mortran3 or another language of the user’s choosing is required. Luckily for those less knowledgeable in programming, there are several applications written for EGSnrc that require no knowledge of Mortran3, or any coding language in general to use. Particularly useful for the simulations carried out in this thesis are the array of applications written in C++ that are distributed with

EGSnrc. These applications use the C++ class library `egs++` (or `egspp`) which includes a geometry package capable of modelling a wide variety of structures, different types of particle sources, scoring classes for quantities of interest, and several other useful classes [33]. Another application of interest to this thesis is *BEAMnrc*, which will be discussed in detail later. The existence of these applications makes EGSnrc relatively easy to work with for many general medical physics needs, and there are detailed tutorials and instructions available to modify or rewrite these applications to suit the user's needs.

1.3.1. Applications within EGSnrc

EGSnrc has several powerful applications available for a variety of common applications. Some examples include the following: *cavity*, *egs_chamber*, *egs_fac*, *egs_cbct*, and *egs_kerma*. Each of these applications are specialized to serve a function in calculating a value of interest. All of these applications are based in the C++ class library `egs++` described earlier. The other application of importance to this thesis that uses EGSnrc is *BEAMnrc* [34], which specializes in modelling linear accelerators. It is an updated version of the *BEAM* code [35] and is a powerful and efficient MC tool that can be used on its own, or in conjunction with other EGSnrc applications. All of these applications require the user to define an input file to communicate the parameters of the desired simulation to EGSnrc. Despite using the same base EGSnrc transport code, the input files between the C++ applications and the *BEAMnrc* application are very different so they must be addressed separately when working with both types of applications.

1.3.1.1. `egs_chamber`

The main application used throughout this project, *egs_chamber*, is an application capable of calculating the dose deposited in the sensitive region of an ionization chamber. The

predecessor to this application, *cavity*, was also used intermittently in the project. All egs++ applications share a set of common definitions in their input files including:

1. **Geometry definition block:** elaborate geometries can be defined in EGSnrc by combining many of the different types of geometries available.
2. **Source definition block:** various sources are available ranging from a collimated point source that can be given an output spectrum to a source defined by a phase space file input by the user.
3. **Run control block:** controls the number of initial particles (histories) and other aspects of the simulation like the number of geometry errors allowed.
4. **Scoring options block:** in the case of *egs_chamber*, the user can specify the region in the geometry where dose should be scored.
5. **Transport parameters block:** each parameter defined in this block can have an impact on the accuracy and efficiency of the simulation so it is important to consider the default values set and if they work for the simulation in question.
6. **Media definition block:** if the simulation is run in “pegsless” mode, meaning that it will not be referencing a PEGS4 data file with material information, then each material used in the simulation must be defined in this block
7. **Variance reduction block:** many different techniques can be implemented in each application to increase the efficiency of the simulation by setting the correct parameters in this block.
8. **Ausgab (output) definition block:** allows the output of various quantities of interest from the simulation, like the dose in a region or the particle tracks from a simulation.

Only two of these blocks have varying options for different egs++ applications; the parameters in both the variance reduction block (discussed at length in the rest of the thesis) and the scoring options block (changes based on what the code specializes in outputting). The inputs associated with each of these blocks must be placed within a set of tags that signify the beginning and end of the block. For example, all the inputs concerning the geometry definitions should be preceded by the line “:start geometry definition:”, and the end of the block is signified by the line “:stop geometry definition:”. Everything between those two lines would be interpreted as inputs for the geometry, and notably, an entire block could be commented out by including the comment character “#” in front of the start definition block.

The most extensive part of creating an input file is typically the definition of the geometry. This refers combining relatively simple shapes in a clever way within EGSnrc to provide complex structures that reflect the simulation geometry of interest. There are a large variety of structures available that can be combined to produce a geometry of interest, but careful planning is required. One example of a very useful object is EGS_ConeStack, which allows the user to define a stack of cones, with each cone having different top and bottom radii and being composed of as many layers as desired. The medium in each of these regions can also be defined individually by the user. This is useful because it can be used to define an entire ionization chamber for simulation. A great tool to assist in making sure one’s geometry is defined correctly, as well as visualizing the defined geometry, is egs_view. By simply entering “egs_view” followed by the name of the input file into the terminal, a 3D representation of the geometry defined in that input file is displayed. With this viewer, the geometry from the input file can be checked against expectations and potential issues can be identified. It is also capable of loading particle tracks that can be output by EGSnrc into a .ptracks file, and used as another check for the geometry, to visualize where most of the radiation is being transported

and how it is behaving in the geometry. One final important note regarding *egs_chamber* is that one of the particle sources available is the EGS_BeamSource, which allows the user to use the output of a *BEAMnrc* simulation as the source for the simulation in *egs_chamber*.

Once the input file is properly setup with all required sections defined, the *egs_chamber* simulation can be run and the output analysed. For a typical simulation, the output is the dose deposited in a user-defined cavity of interest, given in Gy/particle with an associated relative uncertainty. This calculated dose is the mean energy imparted by ionizing radiation with the cavity, normalized to the number of particles incident on the volume. For the purposes of the simulations carried out for this thesis work, ratios of these quantities will be used. As long as the number of incident particles remains the same, this can be done with no issue. This will be discussed later on in the

1.3.1.2. BEAMnrc

In contrast to the input files for the *egs++* applications, *BEAMnrc* input files are much less intuitive on their own but can easily be written through the use of the *BEAMnrc* graphical user interface (GUI). This application involves putting together different component modules (CMs) to create an accelerator. A source can be defined at some point within the accelerator, then the output from this machine can be measured at various points in the geometry. There is a large array of different CMs available in *BEAMnrc*, so only the CMs used in the simulations carried out here will be discussed. The modules needed to create the model shown in this thesis are [34]:

1. **XTUBE**: simulates a user defined target and target holder in an X-ray tube.

2. **CONESTAK**: layers of cones can be defined with different top and bottom radii, but only a single cone can be defined in each layer, with the user being able to pick the media inside and outside the cone.
3. **MIRROR**: simulates the mirror that is typically present in an accelerator to deflect visible light for visualizing the field size.
4. **SYNCJAWS**: creates the geometry for a pair of static X and Y collimating jaws.

In general, while these CMs are sufficient for the construction of a cabinet X-ray machine, they offer much less geometrical freedom than *egs++* geometry. For instance, the CONESTAK CM is similar to the *EGS_ConeStack* class from *egs++* but the user can only define a single cone in each layer and has a limit on the number of layers. In addition, it is important to keep in mind that all of the CMs defined are centered on the *z*-axis. *BEAMnrc* more than makes up for this geometric restriction through the variance reduction techniques available for use, which will be discussed in the next section as well as later in the thesis.

An example image of a few screens from the *BEAMnrc* GUI are shown in **Figure 3**. Each CM is listed in the “Select Components” window, where each can individually be edited. The general parameters of the simulation, such as the number of histories, the variance reduction, and the scoring options, are all set in the “Main Inputs” window accessed through the “Edit main input parameters” button on the “Select Components” window. Each window in the GUI is accompanied by a “Help” button, which opens a window with the relevant information to that specific CM or parameter being chosen. Once parameters are chosen and saved in the GUI, an input file is generated and stored in a directory associated with the accelerator that is defined when the CMs are chosen. This input file can then be used to run a

BEAMnrc simulation to score the output of the machine, or it could be used for the EGS_BeamSource particle source in *egs_chamber*.

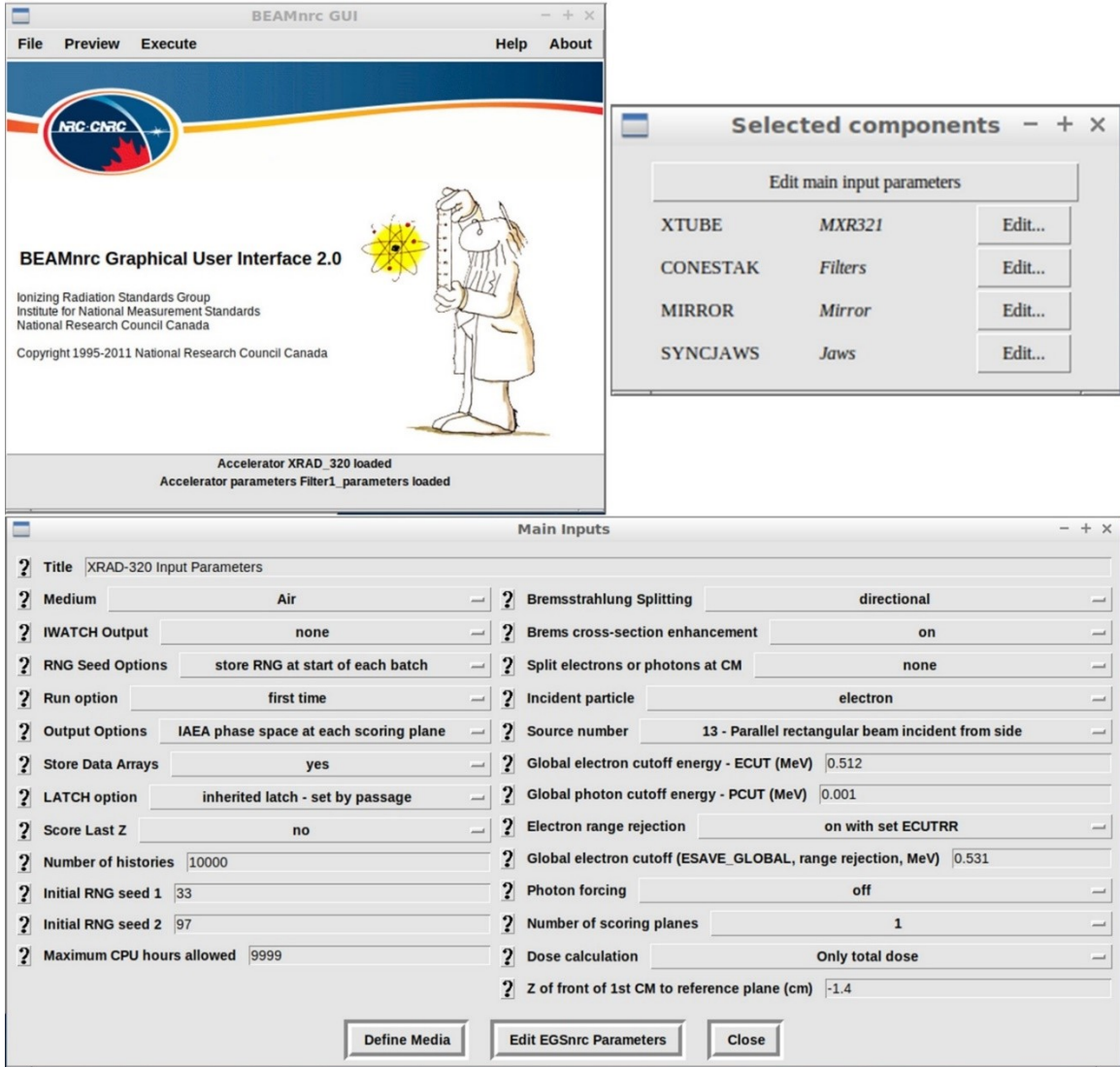


Figure 3: Images of some of the windows from the BEAMnrc GUI that is used to create accelerator modules and their associated input files for BEAMnrc simulations.

1.3.2. Variance Reduction Techniques

Transporting a large number of particles in an MC simulation can typically incur long computational times to produce values with acceptable uncertainties. This can especially be true when calculating very precise values in very complicated geometries. To help alleviate this

issue, many variance reduction techniques (VRTs) have been derived and developed throughout the years to optimize MC simulations. In general, the term VRTs refer to statistical methods that are used to increase the efficiency of code by decreasing the estimated uncertainty and/or by reducing the computational time. The efficiency of a MC simulation is affected by both computation time T , and the estimated relative uncertainty σ . These two quantities can be related through Equation (2) to calculate a MC code efficiency ϵ [36], [37]:

$$\epsilon = \frac{1}{T \cdot \sigma^2} \quad (2)$$

For all quantities simulated in this thesis work in EGSnrc, a statistical relative uncertainty is output from the code. It decreases with the number of incident particles N , as a function of $N^{-1/2}$. With the above definition, this becomes an optimization problem, to simultaneously minimize both the uncertainty and computational time, providing the maximum efficiency possible from the simulation. In addition, when optimizing a simulation with variance reduction, it is important to make the distinction between a true variance reduction technique and an approximate efficiency improvement technique (AEIT) [38]. The former does not alter the underlying physics involved in the MC calculations at all, meaning the results should not be affected in any way by the addition of variance reduction. In contrast, the latter increases the efficiency using an approximation. While this can be a valid way of increasing efficiency, the output values must be carefully tracked to ensure that the AEIT is not having a noticeable effect on the output of the simulation.

A special emphasis is placed on optimizing the MC simulations presented in this thesis because without these techniques in place, most of the simulations would not be able to produce the desired level of uncertainty in a reasonable amount of time. The desired

uncertainty was below 0.5% with a computational time on the order of a few hours. Very long simulation times were still required for two of the models presented in this thesis in order to produce any quantifiable dose output. This is due to these simulations operating in the kilovoltage range, where the process dictating the quantity of bremsstrahlung radiation, referring to the production of X-ray photons from the rapid deceleration of electrons in the X-ray tube target, is incredibly inefficient. Ali 2007 [37] exemplifies this in their M.Sc. thesis by plotting the number of bremsstrahlung photons produced as a function of the incident electron energy E_0 inside a thick tungsten target. The plot focusses more on the diagnostic range at around 100 keV, but at the maximum of the plot one can see that even at 250 keV, the efficiency is only around 17.5%. One must also consider that not all of these photons emitted are useful for irradiation as it is highly dependant on their emission angle. There is a simulation that is discussed later that removes the reliance on bremsstrahlung, which improves the efficiency of the simulation significantly, but due to the complexity of the geometry involved as well as the fact that the dose is being scored in a very small region, VRTs are still required to achieve the desired computation times and uncertainties.

There are several VRTs implemented in EGSnrc that differ between *egs++* applications and the *BEAMnrc* application. The techniques specific to *egs_chamber* that will be used here are bremsstrahlung splitting, range-based Russian roulette (RR), and photon cross section enhancement (XCSE). These VRTs, especially XCSE, can provide large efficiency gains for simulations that *egs_chamber* was designed to run and optimize the simulation around the point of measurement. The exception is bremsstrahlung splitting, which focusses on the point of radiation production in its application here. The VRTs implemented in *BEAMnrc* are different in that their main focus is to optimize the simulation around the area of radiation production. Some of these techniques do overlap with the ones mentioned previously for

egs_chamber, but the following VRTs are unique to *BEAMnrc*: directional bremsstrahlung splitting (DBS), and bremsstrahlung cross section enhancement (BCSE). When a *BEAMnrc* simulation is used as a source in *egs_chamber*, the user can take advantage of all of these VRTs simultaneously to produce maximum efficiency gains.

Most of these techniques rely on the definition of a set of parameters and it is up to the user to determine values for these parameters. Each simulation is unique so optimal values for these parameters must be found on a case-by-case basis. The best way to optimize a given VRT is to calculate the MC efficiency defined in Equation (2) for a range of different values using literature as a starting point. By examining the trends seen in the efficiency, a parameter value that maximizes this efficiency can be found. This is discussed in more detail later on in the thesis.

1.3.2.1. Range-based Russian Roulette

Since electrons are computationally expensive to transport relative to photons, it is important to address redundant electron tracks in this simulation. For example, consider an electron so far away from the sensitive region of an ionization chamber in an *egs_chamber* simulation that it could never reach the region. Tracking this electron and the calculations associated with it offer no influence on the output of the code, only serving to increase the computational time. This inefficiency can be addressed in EGSnrc through the use of the range rejection VRT. The basic idea behind electron range rejection is that at every step in the particle track, the electron's range is calculated and compared to the distance to the closest boundary [32]. If this range exceeds the distance to the closest boundary of the region the particle resides in at that point in the track, then the track is terminated and its energy is deposited in that region. Notably, this implies that range rejection is an AEIT [34], meaning

that requires some assumptions or approximations to be implemented. Discarding this electron early in its path means that any bremsstrahlung photon that could have been produced further down the line with enough energy to leave the region would not be accounted for. To curb the potential error introduced by this approximation an energy value can be set, called E_{save} in *egs_chamber*, above which range rejection is not done. This energy can be carefully chosen based on the scenario such that bremsstrahlung photons with relevant energies cannot be produced by discarded electrons.

Another way to minimize the computational cost of transporting electrons is through the use of the Russian Roulette (RR) VRT. For a given electron, a game of RR is played with the particle having a survival probability of $1/N_r$, with surviving particles having their statistical weight increased by a factor of N_r [36]. The resulting highly weighted particle, called a “fat” electron, could generate photons further down the track with a similarly high weight. To avoid the production of these “fat” photons, all radiative events experienced by the fat electron are split by a factor of N_r to give the photons the correct weighting.

The *egs_chamber* user code combines these two VRTs into effectively a singular VRT, called range-based RR [33]. In this new VRT, a cavity region can be defined in the same way one is set in the calculation geometry block and the following logic is applied for every electron tracked within the simulation in relation to this cavity. Just as was the case for range rejection, at each point in the electron’s motion, the distance it could travel with its remaining energy is calculated using the restricted stopping power of the given region. But in this VRT, the medium being considered in this calculation is defined by the user to be the region near the cavity with the lowest restricted stopping power, providing the largest electron range. If this calculated range is smaller than the distance to the cavity region, then a game of RR is played

with a survival probability of $1/N_r$ as described previously. This is the case for an electron found outside the defined cavity region. If an electron is found to be unable to escape its current region based on the calculated range, it will either enter a game of RR if it is outside the region, but if it is inside the region, it will either continue as normal when above E_{save} , or terminate its track when below.

1.3.2.2. Photon Cross Section Enhancement

In contrast to electrons, photons are relatively cheap to transport as they interact with their environment much less frequently along their track, especially at lower energies. While this is excellent for computational time, it can become a problem when considering a small region irradiated by a low energy photon beam. Many particles would need to be simulated to produce a good estimate of the dose deposited which would effectively end up requiring much more computational power to get reasonable results. To get around this issue and increase the efficiency of codes of this type, *egs_chamber* has a few unique VRT options. This includes photon cross section enhancement (XCSE), intermediate phase space scoring, and correlated sampling. The two latter VRTs focus on optimizing dose ratio calculations, where multiple correlated geometries can be defined within a single input file for percent depth dose or perturbation factor calculations. Therefore these two VRTs are irrelevant for the use in this thesis as none of the simulations are of this nature. On the other hand the first VRT in the list, XCSE, is extremely useful in this scenario and has been shown to provide large increases in MC efficiency. XCSE works by increasing the cross section of photon interaction by a user defined enhancement factor γ_{XCSE} in a given region. This results in more frequent interactions, allowing for an increased production of electrons along the beam path by a factor of γ_{XCSE} . A similar VRT exists in the *cavity* user code called photon splitting, but crucially this is not region

specific and is applied to all geometries involved. One thing to note about this factor is that when this VRT is used in conjunction with range-based RR, the rejection factor must be equal to or greater than γ_{XCSE} . This is due to the fact, as mentioned in the previous section, photons produced from fast electrons are split by a factor of N_r , so these photons cannot properly enter a region with a γ_{XCSE} value that is lower than N_r .

1.3.2.3. Bremsstrahlung Splitting

The previous two VRTs (range-based RR and XCSE) are implemented in *egs_chamber* to improve code efficiency at the point of measurement when radiation is deposited in the sensitive region of a measurement device. The other point of consideration is where the source particles for the simulation originate from. For the purposes of this thesis, the bremsstrahlung effect is mainly responsible for the production of photons in almost all simulations. Bremsstrahlung radiation can be very inefficient at low operating energies, and therefore large amounts of electrons are required to produce the photons to register a reading in a simulation. There exists a VRT usable in *egs_chamber* that is implemented in EGSnrc that tackles this issue called bremsstrahlung splitting. With this technique enabled, each bremsstrahlung event that occurs will be split into a number of events determined by the given radiative splitting factor N_{split} specified in the input file, and each photon from this event will be given a proportionally lower weight. This allows for the production of many more X-ray photons that can be used for calculations further down the track at the ionization chamber. Setting this value high enough can help counteract the inefficiency of bremsstrahlung photon production and produce some dose output without setting the number of electrons hitting the target to an unreasonably large value.

1.3.2.4. Directional Bremsstrahlung Splitting

Within the *BEAMnr* code, a distinction can be made between uniform bremsstrahlung splitting and directional bremsstrahlung splitting (DBS) [39]. Uniform bremsstrahlung splitting operates in the same way that the bremsstrahlung splitting VRT does in *egs_chamber*, each bremsstrahlung event is split into N_{split} events with each photon produced having a proportionally lower weight. While this provides a notable increase in efficiency, the issue with this technique lies in the fact most of the extra photons are produced in a direction such that they will never exit the X-ray tube. A large number of redundant photons being produced would inevitably add to the computation time through the production of secondary charged particles further down their particle tracks. DBS on the other hand is a much more powerful tool unique to *BEAMnr* which effectively restricts photon production in a user defined direction.

The DBS algorithm is much more complicated than that of normal bremsstrahlung splitting and therefore every aspect of the VRT will not be explored here, only details relevant to the implement of the technique in the thesis work [34]. The technique starts the same way uniform bremsstrahlung splitting does with bremsstrahlung photons being split N_{split} , with each photon having their weight decreased by a factor of N_{split}^{-1} . Then each particle resulting from the split is examined to determine whether it is within the user defined direction for splitting, referred to as the splitting field. If it is within the splitting field, the particle continues as normal, and if not a game of RR is played with a survival probability of N_{split}^{-1} from which surviving photons have their weights proportionally increased by N_{split} . This effectively removes most of the relevant photons outside the region of area of interest. In addition, various measures are taken to ensure the elimination of most charged particles in the field such

that in the end, the splitting field is composed primarily of low weight photons. This charged particle information can be recovered through the use of other inputs in DBS but this will not be used in the BEAMnrc model due to the beam being composed almost exclusively of photons. There are a few inputs required for the DBS VRT. This includes the splitting number N_{split} , the radius of the splitting field FS , and the SSD value at which this field size is defined.

The optimal values for each parameter in this VRT can be found in a similar manner to previous VRTs by calculating MC efficiency. The user manual suggests a high N_{split} value of around 5,000, and a splitting field size FS that matches the desired field. The field radius FS should be minimized as much as possible to improve efficiency, but remain large enough that the entire field of interest is covered. As detailed in the next section, DBS will not be optimized alone, it must be optimized together with the next VRT when they are being used simultaneously. Despite all the potential efficiency gains from DBS, the fact still remains that these bremsstrahlung events are extremely rare at the operating energies of the X-ray tube therefore there is potential for further efficiency gain.

1.3.2.5. Bremsstrahlung Cross Section Enhancement

Bremsstrahlung cross section enhancement (BCSE) is a VRT that was introduced in 2007 to attempt to alleviate the problem of low bremsstrahlung interaction frequency at low energies. By artificially increasing the interaction cross section of bremsstrahlung events occurring, they become more frequent and more photons are produced from each electron simulated [40]. The algorithm for the implementation of BCSE consists of enhancing the bremsstrahlung cross section by a user defined enhancement factor f_{enh} . Notably, the user must specify a material where the enhancement occurs, and in the case of the BEAMnrc

model, this material would be tungsten. Due to the nature of how this enhancement works, if the enhanced material is used anywhere else in the *BEAMnr* input file, such as for collimation further down the line, then a separate unique material data file must be created. This is due to the fact that the cross section values in the data file of the enhanced material is altered during the simulation and these altered values would cause issues if the material interacts with particles elsewhere. The photons produced from the enhanced region are given a proportionally lower weight, scaled down by f_{enh}^{-1} . To preserve the physics of the interaction, the charge particle that produced this photon then only loses the amount of energy provided to the emitted photon with a probability of f_{enh}^{-1} , the rest of the time the electron loses no energy during the interaction.

While BSCE can provide good efficiency gains, it has been found for low energy simulations that involve a small solid angle of emission, much higher efficiency gains are produced when BCSE is combined with DBS. When combining these algorithms, steps are taken to ensure the DBS algorithm is not disturbed. In particular, the splitting number is actually the product of the enhancement factor and the splitting number $f_{enh} \cdot N_{split}$ for all bremsstrahlung events excluding the events that occur within the medium chosen for enhancement with BCSE. The exception is all the events that occur within the enhanced medium, in which case the splitting number is set to N_{split} [40]. This results in bremsstrahlung events being split N_{split} times with a cross section of interaction enhanced by a factor of f_{enh} , effectively increasing photon production from the target by $f_{enh} \cdot N_{split}$.

1.4. Thesis Statement

The main goal of this thesis was to develop and test an accurate MC model of the X-ray setup used at Health Canada's Consumer and Clinical Radiation Protection Bureau biodosimetry laboratory. To that end, this was done through a multi-step approach:

- (1) Develop a schematic design of the XRAD-320 and recreate the geometry in EGSnrc
- (2) Use *egs_chamber*, *BEAMnrc*, and SpekPy to model the X-ray setup
- (3) Optimize *egs_chamber*, *BEAMnrc*, and SpekPy models using variance reduction techniques, with a special emphasis on the techniques unique to each specific application
- (4) Conduct a preliminary phase of testing for each of the models to check agreement with laboratory measurements
- (5) Improve the XRAD-320 design based on results from preliminary testing phase and information gathered from the manufacturer
- (6) Change models to match new design schematic and re-optimize variance reduction techniques
- (7) Conduct a final phase of testing for each of the models to check agreement with laboratory measurements

Based off the results found in the final phase of testing, an optimal model was chosen from the *egs_chamber*, *BEAMnrc*, and SpekPy models to accurately reflect the Health Canada laboratory setup.

2. Materials and Methods

2.1. Health Canada's Experimental Setup for Blood Irradiation

Generating a dose-response calibration curve for any biodosimetry technique requires irradiating biological samples, such as blood, to an appropriate range of dose values. Then the biological damage of interest can be scored and that data can be used to plot a calibration curve. In particular, for the DCA blood samples, drawn from healthy, non-irradiated volunteer donors, are irradiated and the biological damage is assessed at different dose values. At Health Canada, this irradiation is done through the use of a cabinet X-ray machine, the XRAD-320 (Precision X-ray, Madison, USA), the specifications of which are described below in Section 2.1.1. The X-ray machine is calibrated prior to irradiation with a gas-filled radiation detector, called an ionization chamber. Vials of blood are placed within blocks composed of water-equivalent material, referred to as phantoms, in the path of the radiation beam and irradiated to doses between 0 and 5 Gy. The resulting chromosome damage is quantified by counting the number of dicentric chromosomes per cell and graphed as a function of the dose to create the calibration curve, an example of which was shown in **Figure 2**.

2.1.1. XRAD-320

Health Canada uses the XRAD-320 (Precision X-ray) cabinet X-ray machine as the source of radiation to irradiate blood samples to create biodosimetry calibration curves. This system specializes in delivering precise doses of radiation to relatively small specimens, ranging from cells to small animals. The machine operates in the orthovoltage range (150kV-500kV) and is capable of delivering a maximum X-ray energy of 320 kV and a maximum X-ray tube current of 15 mA. In addition, several add-ons are available for the machine including beam conditioning filters, adjustable collimators, and adjustable shelving.

There are several key components that work together to produce a uniform, collimated X-ray beam for irradiating samples. Beginning at the point of X-ray production, the XRAD-320 is equipped with an MXR-321 X-ray tube, which uses a tungsten target placed at a 30° angle to convert incoming electrons to photons through the bremsstrahlung effect. Notably, the X-ray tube has 3 mm of inherent beryllium filtration. The purpose of this filtration, as well as the adjustable filtration further down the beam path is to change the shape of the beams intensity as well as remove lower energy photons from the beam. Following this is a primary lead collimator, which provides some initial shape to the beam exiting the X-ray tube. This beam can then be filtered by filters of varying materials. There are currently two interchangeable filters used with the XRAD-320 at Health Canada:

- Filter 1: 2.0 mm Al
- Filter 2: 1.5 mm Al + 0.25 mm Cu + 0.75 mm Sn

For additional filtration, materials can be taped to the exit window of the X-ray machine and for this project, a third filter was introduced in this manner. Filter 3 uses Filter 1 with an addition piece of metal composed of 0.13 mm of copper and 0.5 mm of aluminum so the effective filtration is:

- Filter 3: 2.5 mm Al + 0.13 mm Cu

It is also important to note that the machine can also be run with no filtration, meaning that the beam will only be affected by the inherent filtration. Once the beam has passed the filters, it will reach the monitor chamber (PTW 7862 parallel plate transmission chamber (PTW, Freiburg, Germany)). The purpose of this chamber is to monitor the radiation beam and check whether it matches the specifications provided by the user. The entrance and exit

windows of the chamber are composed of 2 mm of Kapton, a commercially available graphite coated polyimide, with approximately 2 mm thick air gap in between. Following this, the beam passes through a 1.5875 mm thick mirror, composed of borosilicate glass, and placed at a 45° angle which is the final component of the XRAD-320. The main purpose of this mirror is to redirect visible light through the beam path and out of the collimating jaws to illuminate the radiation field. Using the 0.635 cm thick lead collimators, the beam can be shaped into rectangular field with the side length ranging from 0.5 cm to 20 cm at a source-to-surface distance (SSD) of 50 cm. One final important piece of the XRAD-320 to consider with respect to modelling, is the adjustable shelf on which the sample rests. This shelf can provide SSD values ranging from 20 cm to 90 cm. The composition of the shelf is assumed to be stainless steel for the purposes of simulation. A picture of the inside of the XRAD-320 cabinet can be seen in **Figure 4**, with the full irradiation setup in place. Most of the components described above cannot be seen in this image as they are covered by casings so the positioning of these components along the beam path were estimated based on measurements of the casings.

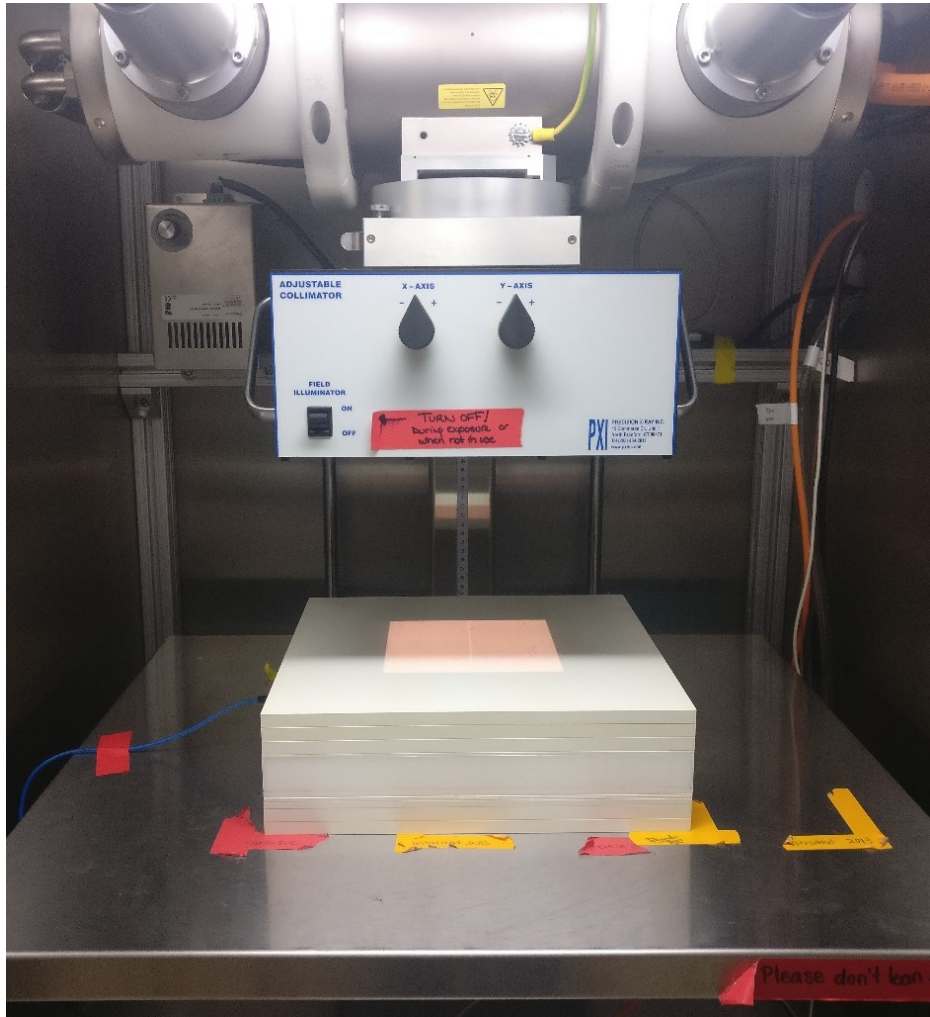


Figure 4: Picture of the inside of the XRAD-320 cabinet with the full experimental setup used for irradiation of blood vials for biodosimetry in place.

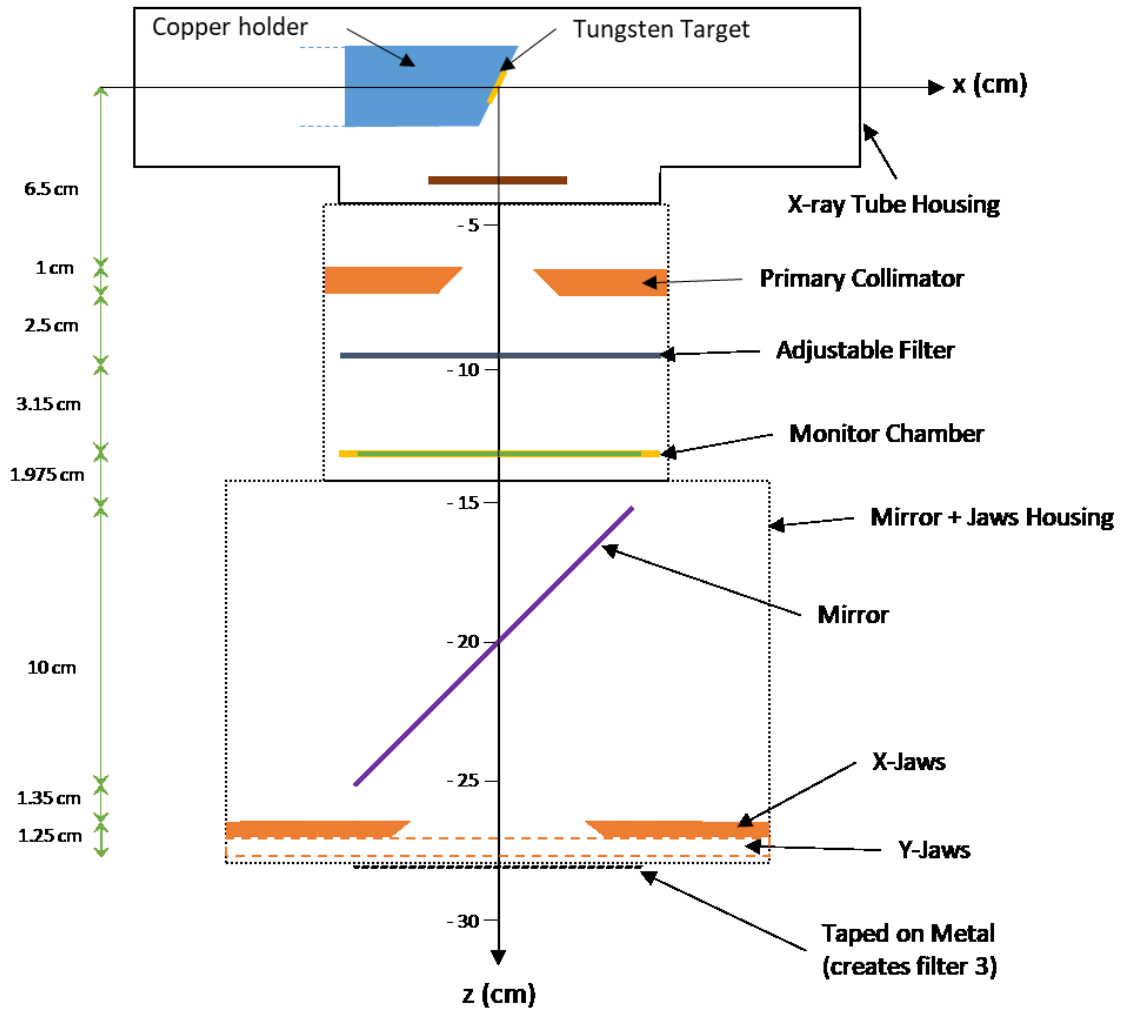


Figure 5: Schematic diagram of the X-ray machine shown in Figure 4, the measurements shown here were used in the final design of the MC models. Measurements in the x-axis are omitted as the scaling in the image in the x-axis is approximate.

2.1.2. PTW 30010 Ionization Chamber

Dose measurements are taken using the PTW 30010 ionization chamber (PTW), seen in **Figure 6**, in conjunction with the PTW UNIDOS T10002 electrometer (PTW). The electrometer is set to start collecting data right before the beam is turned on, after which it integrates the charge accumulated on the electrode until the end of the irradiation. This reading can then be converted into a dose value, but first it must be corrected with the expression shown in Equation (3).

$$M = M_{raw} \cdot P_{TP} \cdot P_{leak} \cdot P_{pol} \cdot P_{elec} \cdot P_{rp} \quad (3)$$

The above equation is composed of the electrometer reading M_{raw} , typically recorded in nanoCoulombs (nC), which is multiplied by various factors to account for different aspects of the measurement. The most important of these factors being P_{TP} , the air density correction factor, and P_{leak} , which accounts for measurement leakage or instrument drift. The other factors include P_{ion} , which accounts for incomplete collection of charge from an ionization chamber, P_{pol} , which accounts for the change in absolute value due to changing the sign of the collected charge, P_{elec} , which accounts for changes in electrometer sensitivity, and P_{rp} , which accounts for radial variation in the radiation intensity profile. For the purpose of measurements carried out in the experiments detailed in this thesis, most of these factors can be taken to be unity. The only factors that would not be unity are P_{TP} and P_{leak} . By recording the temperature (T) and pressure (P) of the room when measurements are taken, P_{TP} can be calculated using Equation (4).

$$P_{TP} = \frac{101.325 \text{ kPa}}{P} \times \frac{T + 273.15 \text{ K}}{295.15 \text{ K}} \quad (4)$$

In addition, P_{leak} can be calculated by taking into account the leakage rate (\dot{B}) and the time (t) required for the irradiation to occur using the relation defined in Equation (5).

$$P_{leak} = 1 - \frac{\dot{B}t}{M_{raw}} \quad (5)$$

To determine \dot{B} , one should take a reasonably long reading before actual measurements are taken with no radiation present. This provides a good estimate of the instrumental drift throughout subsequent irradiations and allows for a proper estimation of P_{leak} .



Figure 6: Image of the PTW 30010 ionization chamber used for electrometer measurements and calibration.

Once the correct reading M is calculated, the air kerma (K_a) and exposure (X) can be calculated using calibration coefficients established during instrument calibration through Equations (7) and (8).

$$K_a = MN_K \quad (7)$$

$$X = MN_X \quad (8)$$

The last calibration of the PTW 30010 ionization chamber was completed on May 8th, 2020 by the National Research Council (NRC), and these calibration coefficients were detailed in NRC Report IRS-2020-3082. For a generating potential of 135 kV, the coefficients were found to be:

$$N_K = 48.07 \pm 1.0\% \frac{mGy}{nC}, N_X = 5.485 \pm 1.0\% \frac{R}{nC} \quad (9)$$

And for a generating potential of 250 kV, they were reported to be:

$$N_K = 48.29 \pm 1.0\% \frac{mGy}{nC}, N_X = 5.510 \pm 1.0\% \frac{R}{nC} \quad (10)$$

Notably, these constants differ minimally but non-negligibly between the two chosen energies, indicating the importance of considering the X-ray energy used in one's irradiation.

With all of these constants and knowledge in hand, the electrometer reading can be converted to a dose measurement if the appropriate constants are considered for the situation. For the purposes of the experiments detailed in this report, ratios of measurements are taken

for comparison to code output. Considering the corrected reading equation and the air kerma equation, if two measurements are taken with the same conditions and the same energy, then a ratio of K_a values would provide the same result as a ratio of M_{raw} values as the constants would all cancel out. Therefore, these calculations will only be done in instances that do not involve ratios. Notably, when a ratio is taken of two measurements with different values of P_{TP} or P_{leak} , on different days for instance, then these constants need to be considered in the ratio.

2.1.3. Solid Water-Equivalent Phantoms

When measurements are taken with the ionization chamber, or the blood vials are irradiated, they are placed within blocks of solid water, a water-equivalent material, known as phantom. These blocks are squares of length 15 cm, but with varying thicknesses, allowing the irradiated sample to be placed at varying depths within the solid water. More specifically, the type of solid water material used for most of the blocks in these experiments is commercially known as RW3. Produced by PTW, this material is mainly made up of polystyrene (C_8H_8) taking up 98% of the fractional composition, while the rest is titanium oxide (TiO_2) [41]. In addition to these solid water phantoms, there are two special phantoms capable of holding blood vials as well as the ionization chamber for irradiation.

2.1.3.1. Single-slot Phantom

The first of the two special phantoms is the single-slot phantom. This phantom is fully composed of RW3 and has a slot carved out that can fit the ionization chamber or a blood vial. The ionization chamber cavity goes far enough into the phantom that the sensitive region of the ionization chamber can be positioned right at the center of the beam field. This phantom has a total thickness of 2 cm and additional blocks of solid water can be placed above

and below to create the desired depth in solid water. An image of the outside of this phantom can be seen in **Figure 7a**.

2.1.3.2. Multi-slot Phantom

The second special phantom is the multi-slot phantom, an image of which can be seen in **Figure 7b**. This phantom, custom designed and ordered from Radiation Products Design, Inc. (Albertville, Minnesota, United States), is capable of fitting the ionization chamber plus 7 blood vials at the same time. The schematic drawing used to produce the phantom can be seen in **Figure 8** that shows the location of the ionization chamber cavity in relation to the other cavities. There are a few notable differences that are important to consider when comparing the two special phantoms. The first is that the ionization chamber cavity is offset from the center, so it provides a more accurate estimate of the dose being received by the blood vials surrounding it since they are all the same distance from the center of the field. The next big difference is the presence of the 7 larger air cavities capable of holding blood vials of different sizes. These slots allow for irradiation of many samples simultaneously. The final notable difference between this phantom and the previous is that this phantom is completely composed of polystyrene instead of RW3. The difference between RW3 and pure polystyrene is non-negligible and must be considered when taking measurements with this phantom.

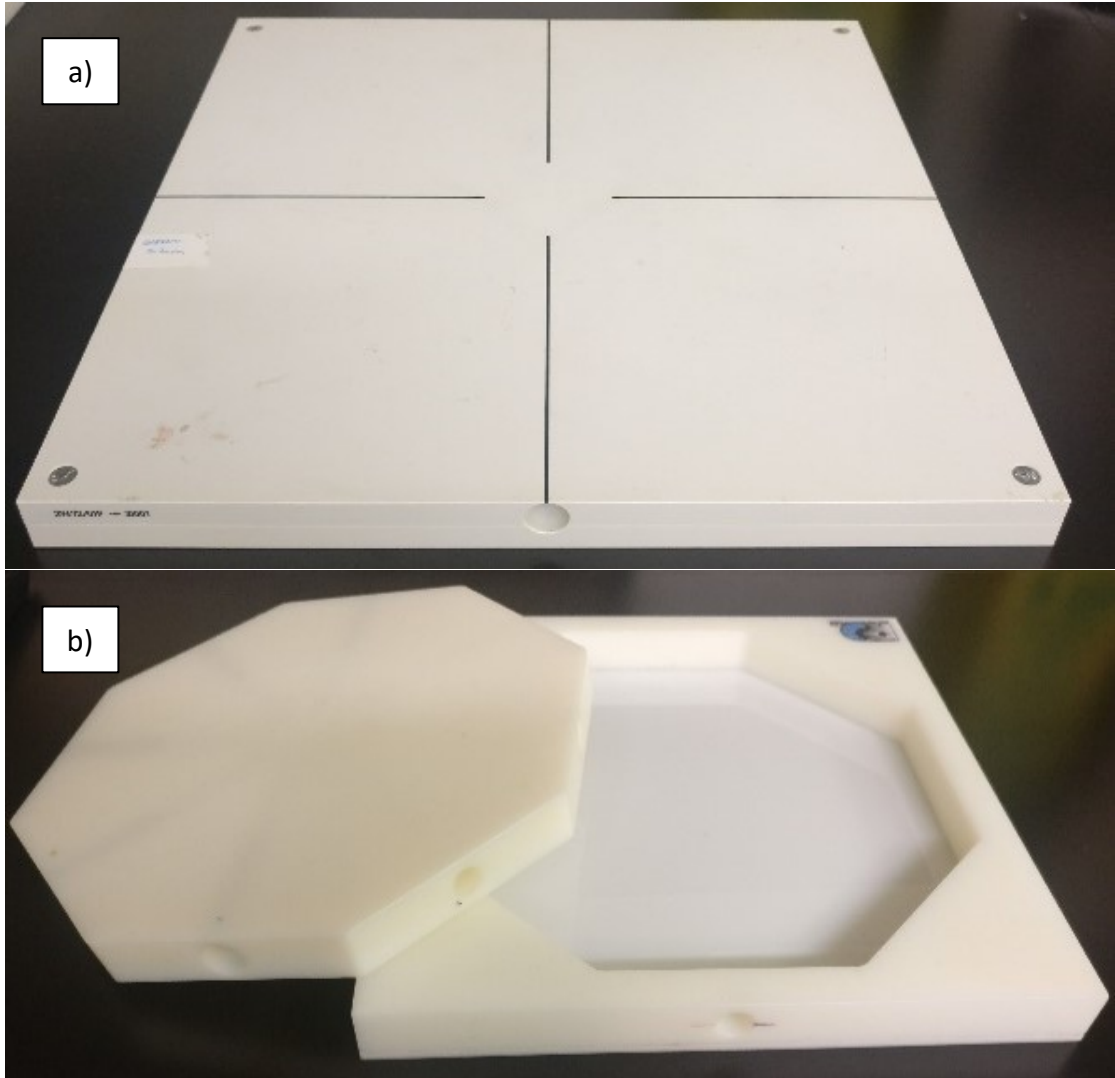


Figure 7: Images of the phantoms used to hold either the ionization chamber or blood vials for irradiation. The a) single-slot phantom contains 1 cavity for either the ionization chamber or a blood vial, while the b) multi-slot phantom contains 8 slots.

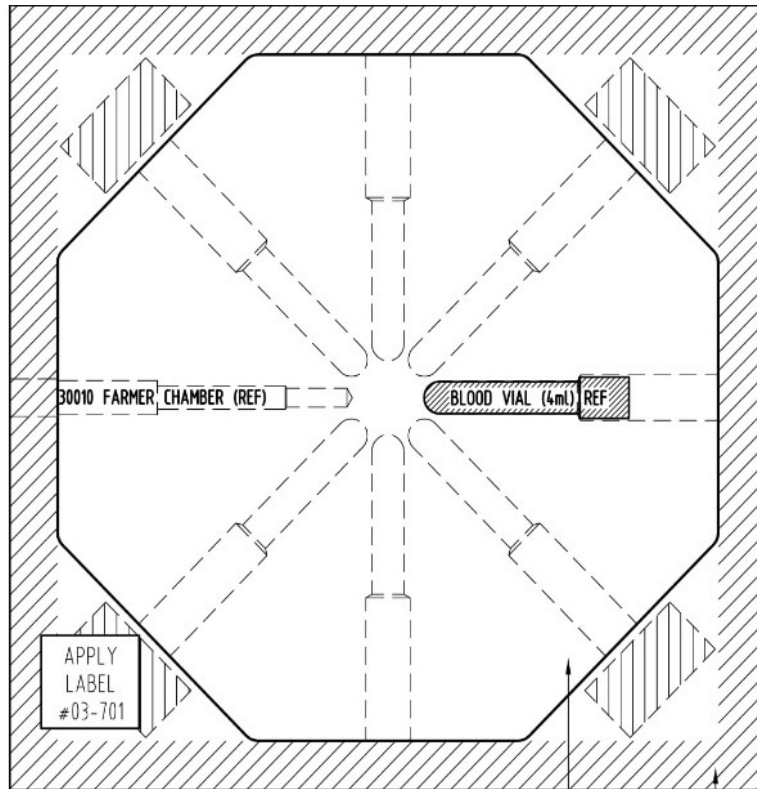


Figure 8: Schematic drawing of the multi-slot phantom provided by Radiation Products Design, Inc. showing the ion chamber and a blood vial in place.

2.1.4. Setup Error Estimation

When considering measurements in a laboratory, uncertainty can come from many different places, so it's important to consider all sources of error. Any measurement taken with an instrument will have some sort of instrumental error associated with it. In this case, the measurements are taken with an electrometer which has a digital display with precision down to the second decimal place. Therefore the instrumental error on any measurement taken in the experiments presented in this thesis will be ± 0.01 nC. In addition, statistical error can be accounted for by taking each measurement in triplicate and calculating the standard deviation. While combining these errors would provide a decent estimate of the actual error on the measurement, there are a few other sources of error that must be considered. These

discrepancies originate in the inherent uncertainty introduced in the setup procedure for any irradiation. The two main points of the setup that need to be analyzed are the field size and the SSD. The influence of these factors on the electrometer reading can be evaluated by studying them individually and also examining the reproducibility of the experimental setup.

The field size is determined by the collimating jaws in the XRAD-320 which are manually controlled by external knobs. To choose one's field size, the SSD is first chosen and set. Then the light field projected on to the stage is measured by a ruler and adjusted using the knobs until the desired field size is found. Alternatively, the chosen phantom can be placed such that the ionization chamber cavity is positioned at SSD, then the field size can be set on top of the phantom. While this method provides a less exact field size at the SSD, it can be accurate enough for most irradiations. In general, an exact field size can be difficult to set due to blurring at the edges of the field so this process must be given an error value to account for this discrepancy. After taking into consideration the difficulty of manually choosing a field size with the knobs, as well as the inaccuracy introduced by the edge blurring, an uncertainty of ± 0.05 cm on each side of the field would be appropriate. The simplest way to determine how this would directly impact the electrometer reading is to take measurements at several difference field sizes and use a line of best fit through that data to convert this uncertainty in field size to an uncertainty in nC. Based off of the inverse square law for radiation intensity, the expected trend is an inverse square scaling with the field size. Increasing the field size while holding the SSD and measurement area constant would have the same impact as increasing the distance from the source. Measurements were taken with field sizes ranging from 12 cm x 12 cm to 18 x 18 cm in the multi-slot phantom, with filter 1 in place, at 50 cm SSD, and an energy of 250 kV. Since a relatively small range is used, the trend can be approximated to a linear one with a good degree of accuracy for ease of error calculation and propagation.

Similarly, setting the SSD comes with its own associated error. This distance is determined by a ruler marked at the back of the interior of the cabinet and the stage is moved manually by turning a key at the control console. The stage travels a few millimeters with a small turn of the key so it can be difficult to precisely set the SSD. In addition, due to the SSD indicator being at the back of the cabinet, the value can be difficult to see and track as the stage is being moved. Taking all these factors into consideration, a similar uncertainty value of ± 0.05 cm will be given to this measurement as well. The exact same procedure was taken to determine the scaling of the SSD with electrometer reading as for the field size described previously. SSD values ranged from 48 cm to 52 cm, with measurements taken in the multi-slot phantom using a 15 cm x 15 cm field size, filter 1 in place, and an energy of 250 kV. Using a similar line of thought as earlier, a linear fit is valid.

An additional way to gauge the error introduced by the uncertainty in field size and SSD determination is to consider the reproducibility of setup. This refers to the experimenter's ability to recreate the setup each time a new set of measurements is required. It can be tested by repeatedly resetting up the irradiation setup and examining the change in electrometer reading in each of these setups. To estimate the error here, 5 measurements were taken with the entire phantom being disassembled and reassembled between each measurement. The multi-slot phantom was used with filter 1 in place at an SSD of 50 cm for 30 s exposures. Theoretically, this could account for errors in both field size and SSD but one thing to consider is that most measurements being compared were taken in the same session in the laboratory, so there was minimal change in the setup. Despite this, reproducibility was checked to compare the error estimated by this set of measurements to the error estimated by the field size and SSD scaling considerations made earlier. If there was a significant difference in

magnitude between the errors estimated in these two ways, this would be cause for concern and further investigation.

2.2. Monte Carlo Modelling through EGSnrc

2.2.1. Three Models

The experimental setup described above was modelled in three different ways within EGSnrc. More specifically, the 2021 version of EGSnrc [27] was used for all simulations. As previously mentioned, EGSnrc has several applications that can be used for this purpose. Each model presented here has advantages and disadvantages when it comes to code accuracy and efficiency. It is important to explore these options and pick an optimal model to use in this project. The most critical component of the exposure system when considering each of these models is the point where photons are created, the X-ray tube. As previously discussed, at the operating energies of the XRAD-320 photon production via the bremsstrahlung effect is very inefficient [37]. In MC simulations, photons are relatively computationally inexpensive to transport, but the electrons that produce those photons, as well as the secondary electrons produced further down the line will require a lot more computational power. Taking this into consideration, the number of electrons required for photon production in the X-ray tube in each model needs to be carefully considered as it will be the limiting factor when it comes to overall computational time and accuracy.

The overall specifications for the XRAD-320 cabinet X-ray machine were set the exact same wherever applicable for all three models. These specifications were derived from the previous studies that have simulated the XRAD-320 in EGSnrc previously [42]–[44], as well as assistance from the manufacturer. The workflow for the creation and validation of this model in three different ways in EGSnrc is presented in **Figure 9**. Initially, the model was

fully created using egs++ geometry within EGSnrc, and then because of the problem of inefficient bremsstrahlung, the SpekPy and BEAMnrc models were created. A preliminary phase of testing was done with the established geometry. To start this phase, the variance reduction techniques used in each model were optimized to achieve sufficiently low uncertainties from each simulation within a reasonable time period. Once this was complete, the models were compared to each other to assess the difference between them and work towards adjusting them until they were in agreement. In addition, each model was checked for agreement against an array of laboratory measurements and further assist in iterating the preliminary design. Additional information was also acquired about the XRAD-320 from the manufacturer to make the models more accurate. This included composition of the monitor chamber, the thickness of the mirror, the addition of the steel stage, and the composition of the two different solid water phantoms. Once these changes were implemented and a final design of the X-ray setup was drafted, the MC code for each of the three models were adjusted to reflect these geometrical changes. A final phase of testing was done that began with a re-optimization of variance reduction techniques, followed by a comparison of the models similar to the preliminary phase. The models were then tested against a complete set of laboratory measurements, with measurements being taken at different energies to provide a wider range of validation. Based on the results found in this final phase of testing, the best overall model could be chosen based on accuracy and efficiency to be used to create phase space files of the X-ray output to be used in the next phase of the project.

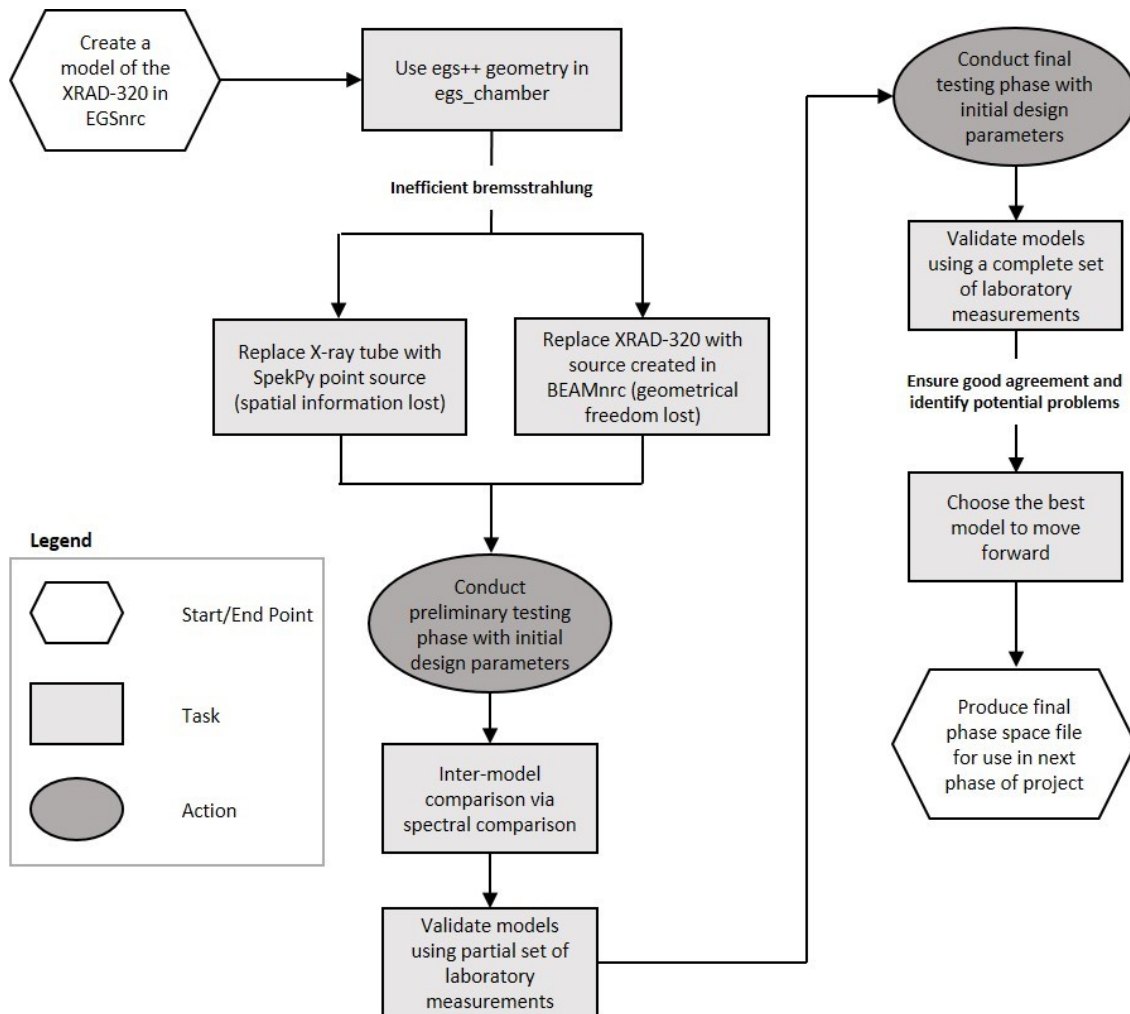


Figure 9: Flowchart for creation and testing of a Monte Carlo model of the XRAD-320 cabinet X-ray machine, created in three different ways using applications in EGSnrc.

2.2.1.1. egs++ Model

The first model is named the egs++ model because the entire simulation was done in *egs_chamber* with all components of the setup being built with egs++ geometry. The main component to consider is the egs++ geometry defining the X-ray tube. An input file containing the geometry of a previous version of the MXR-321 X-ray tube, namely the MXR-320 tube, was provided by Dr. Frédéric Tessier from the NRC. The full geometry is composed of cone stacks that have been dissected with planes and cleverly combined to produce a

tungsten target, a target holder, and an exit window for the photons. By comparing the specification sheets of the two X-ray tubes, the main difference was found to be in the target angle so once that part of the geometry was corrected and the X-ray tube was ready to be simulated. The source is set to be a point source of electrons using the EGS_ParallelBeam class. It is positioned such that the electrons start where the cathode in the X-ray tube should be and travel towards the tungsten target to create the X-rays required for the simulation. The body of the XRAD-320 detailed previous including the primary collimator, filter, monitor chamber, mirror, and collimating jaws, were modelled using the EGS_ConeStack class in egs++. The mirror and the jaws in particular were created by dissecting those regions with a set of planes. The full combined geometry can be seen pictured in **Figure 10** excluding the ionization chamber and phantom geometries. These geometries were also created in egs++ and placed at the end of each of the models described but they will be further discussed later on. All materials used in the model in **Figure 10**, as well as any materials required for ionization chamber and phantom geometries, are listed in **Table 1**.

Simulating the full X-ray tube brings about the issue of bremsstrahlung inefficiency, which is partially addressed by using one of the VRTs available in EGSnrc, bremsstrahlung splitting, which was discussed in more detail in Section 1.3.2. Having this along with other VRTs enabled and optimized, the simulation times are more reasonable as fewer electrons would be required to get the desired level of precision. In addition, this model offers the advantage of being very geometrically flexible, where the addition of geometry of any shape can be defined with relative ease. This is a stark contrast against the other model that models the entire X-ray tube, the BEAMnrc model, which has a much more rigid set of geometry definitions.

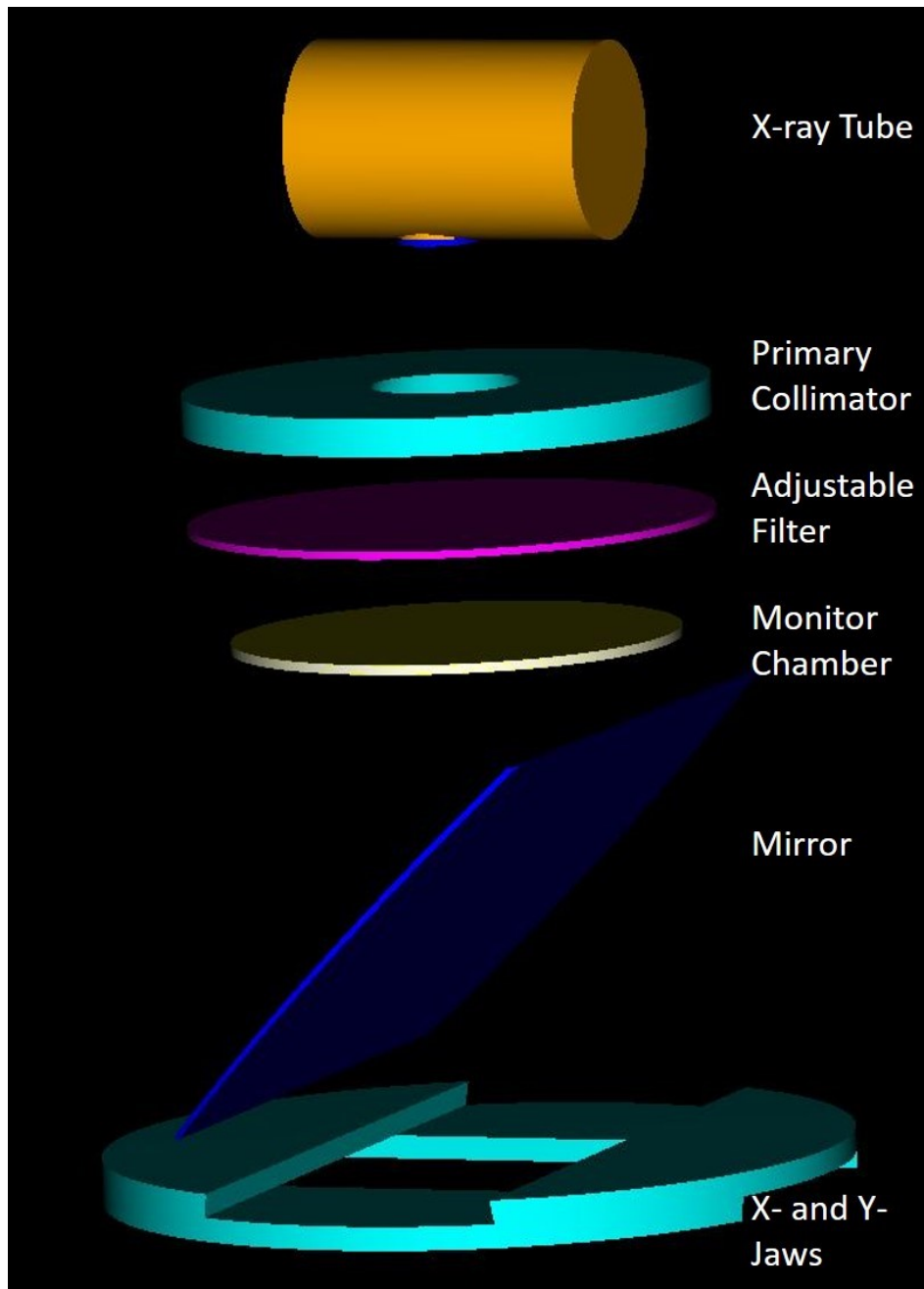


Figure 10: Partial view of the egs++ model focussing on the X-ray tube and the components that compose the XRAD-320 body, each being labelled on the right side of the figure. Produced using egs_view.

Table 1: List of materials used in EGSnrc simulations.

Material	EGSnrc Density Correction Filename (.density)	Elemental Mass Fractions	Mass Density ρ (g/cm^3)
Air	air_dry_nearsealevel	0.0001 C, 0.7553 N, 0.2318 O, 0.0128 Ar	$1.205 \cdot 10^{-3}$
Stainless Steel	steel_stainless_type302	0.001 C, 0.007 Si, 0.180 Cr, 0.010 Mn, 0.712 Fe, 0.090 Ni	8.060
Tungsten	tungsten	W	19.30
Lead	lead	Pb	11.35
Aluminum	aluminum	Al	2.700
Copper	copper	Cu	8.960
Germanium	germanium	Ge	5.323
Beryllium	beryllium	Be	1.848
Glass	glass_borosilicate__pyrex__cornin g7740	0.040 B, 0.539 O, 0.028 Na, 0.012 Al, 0.377 Si, 0.003 K	2.230
PMMA	polymethylmethacrylate__lucite__ perspex__pexiglas__	0.080 H, 0.600 C, 0.320 O	1.190
Kapton Polyimide Film	kapton	0.026 H, 0.691 C, 0.073 N, 0.209 O	1.420
Polystyrene	polystyrene	0.077 H, 0.923 C	1.060
RW3 Solid Water	rw3	0.076 H, 0.904 C, 0.008 O, 0.012 Ti	1.045
Tin	tin	Sn	7.310

2.2.1.2. SpekPy Model

The second of the three models, the SpekPy model, was created fully within the *egs_chamber* application as well. By using the *EGS_CollimatedSource* class, the entire MXR-321 X-ray tube can be replaced by a collimated point source of photons carrying the output spectrum of the X-ray tube. The main idea behind this approximation was that this limited the

need to simulate computationally expensive electrons when producing the X-ray beam. The spectrum used by the point source could be defined in two different ways. The first is to do it inline by typing out a list of energies and the associated probabilities of a particle having that energy. Alternatively, a tabulated spectrum can be defined and saved in an external file to be referenced in the code block. Using a spectrum file was a more viable option for this model due to the large number of energies required to get a precise spectrum. Each spectrum file must follow a specific format described in the BEAMnrc Users Manual [34], which is as follows:

.spectrum File Format

Line #	Contents	New Variable Definitions
1	SPEC_TITLE	SPEC_TITLE = 80-character maximum spectrum title
2	NENSRC, ENMIN, IMODE	NENSRC = number of energy bins in the spectrum histogram ENMIN = lower energy of first bin in MeV
3	ENSRC(1), SRCPDF(1)	ENSRC(1) = upper energy of bin 1 in MeV SRCPDF(1) = probability of finding a particle in bin 1
4	ENSRC(2), SRCPDF(2)	ENSRC(2) = upper energy of bin 2 in MeV SRCPDF(2) = probability of finding a particle in bin 2
⋮	⋮	⋮
NENSRC + 2	ENSRC(NENSRC), SRCPDF(NENSRC)	ENSRC(NENSRC) = upper energy of bin NENSRC in MeV SRCPDF(NENSRC) = probability of finding a particle in bin NENSRC

The challenge then became tabulating the spectrum output from the MXR-321 X-ray tube with enough precision to replace the entire tube. One effective way to calculate this spectrum is by using the software toolkit SpekPy [45], [46], which is capable of finding X-ray spectra output from an X-ray tube with user defined properties. The code for SpekPy is written in the python language, and to access the spectra from this toolkit, a simple python script must

be written by the user. Additional physics models [47]–[49] were incorporated into SpekPy to create SpekPy V2, which is the version used to generate the spectra used in this thesis. There are several mandatory selections that need to be made to produce a spectra including: the X-ray tube potential (kV), the tungsten anode angle, and the position to evaluate the spectrum. In addition, varying thicknesses of materials can be placed in the path of the beam to act as filtration including: air, beryllium, aluminum, copper, tin, tungsten, tantalum, and water. An example of a script is shown in **Figure 11** where a 250 kV spectrum is being produced for a 30° tungsten target with 3 mm of beryllium filtration. This spectrum is saved as a “.txt” file with a large header containing all the information reading the inputs, as well as the outputs, following by tabulated energies and probabilities. The formatting of the spectrum files output by SpekPy did not match the format required by EGSnrc, so a small python code was written to extract the correct information from the SpekPy output files and format this information in the EGSnrc style shown previously. With this new “.spectrum” file placed within the *egs_chamber* folder, it can be referenced and used in this SpekPy model to replace the entire MXR-321 X-ray tube. The rest of the XRAD-320, the ionization chamber, and the phantom were modelled using egs++ geometry, just as in the egs++ model.

```
1   ### Producing SpekPy spectra for XRAD-320 ###
2
3   # Import SpekPy as a package
4   import spekpy as sp
5
6   # Generate a spectrum (250 kV, 30 degree tube angle)
7   s = sp.Spek(kvp=250, th=30, dk=1)
8
9   # Apply inherent filtration of 3 mm Be
10  s.filter('Be', 3.0)
11
12  # Export spectrum to a text file
13  s.export_spectrum(file_name="example.txt", delim='')
```

Figure 11: Example code for producing a spectrum through SpekPy. This code would produce a 250kV spectrum for an X-ray tube with 3 mm of beryllium filtration, which is the case for the MXR-321.

2.2.1.3. BEAMnrc Model

The third and final model was created using the *BEAMnrc* application in EGSnrc, which specializes in simulating radiotherapy beams from linear accelerators. Input files in *BEAMnrc* are built completely differently than *egs_chamber* input files, as described in Section 1.3.1.2, where the simulated accelerator is a combination of component modules (CMs). There are a variety of different CMs available that can be arranged in any order, combined by a parallel plane between each other. To create the entire XRAD-320 in BEAMnrc, the following set of component modules were used in the order given [34], [35]:

1. XTUBE
2. CONESTAK
3. MIRROR
4. SYNCJAWS

First, the XTUBE CM defines the MXR-321 X-ray tube, without the inherent 3 mm of beryllium filtration. Then the next CM in the stack, CONESTAK, starts with the layer of inherent Be filtration, followed by the primary collimator, the filter, the monitor chamber, and the air gaps in-between all of these pieces. After this, the MIRROR CM is used to model the light mirror. And finally, the BEAMnrc model ends with the SYNCJAWS CM, which allows for the definition of the X and Y collimating jaws. A full diagram of the BEAMnrc model can be seen in **Figure 12**.

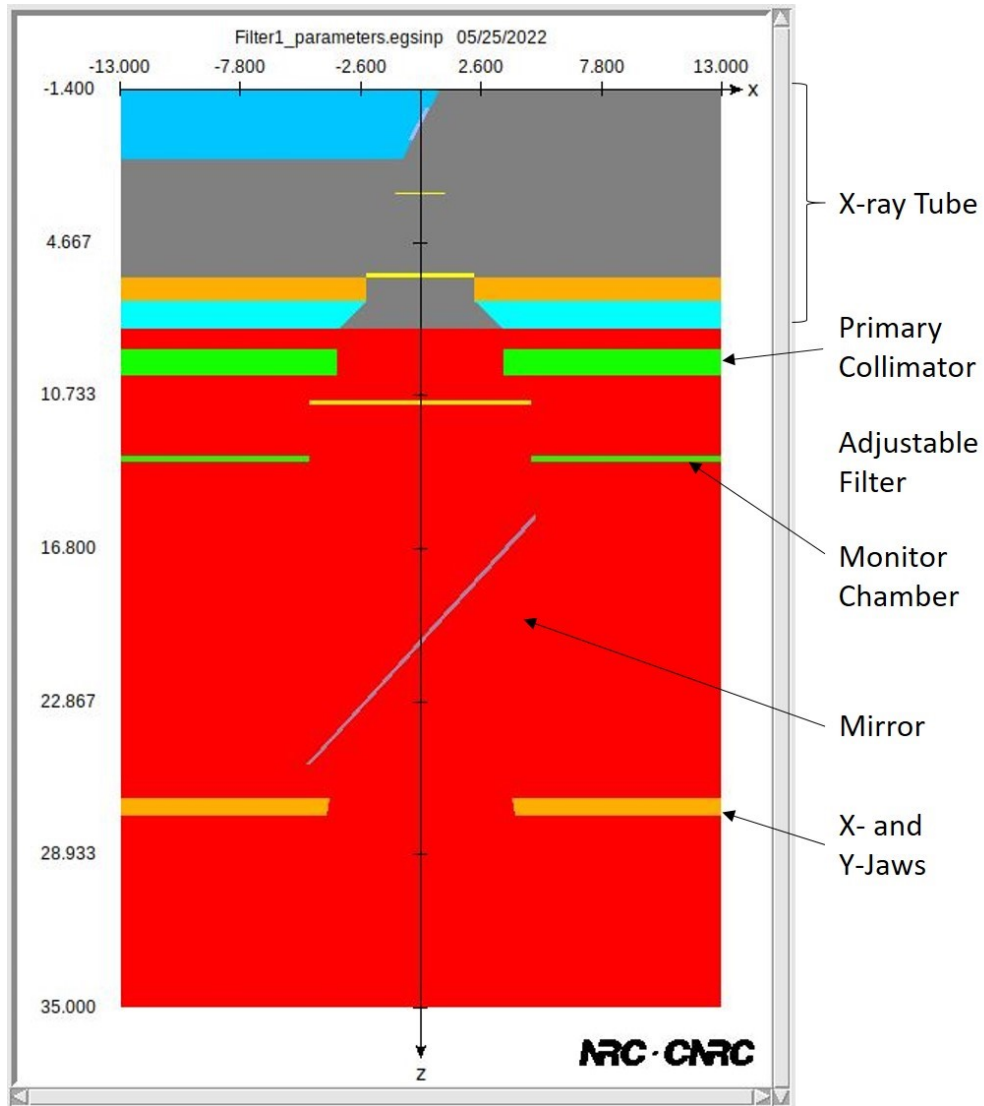


Figure 12: Schematic of the MC model of the X-ray machine created in the EGSnrc application *BEAMnrc*, visualized using the *BEAMnrc* GUI. Each component of the system is labelled similar to the *egs++* model shown in Figure 10.

Once this model in *BEAMnrc* was complete, it was integrated into *egs_chamber* such that the dose deposited in the ionization chamber could be scored. The phantom and the ionization chamber are the only pieces of geometry defined within *egs_chamber*, with the rest being accounted for within *BEAMnrc*. One way to use *BEAMnrc* in conjunction with *egs_chamber* is to use the *EGS_BeamSource* class, which allows the user to perform a full *BEAMnrc* simulation and output the resulting particles from the source location defined in *egs_chamber*. The main reason for moving this *BEAMnrc* model into *egs_chamber* for scoring was

that an ionization chamber like the PTW 30010 chamber could not be modelled within *BEAMnrc*. In addition, it offered the added advantage of being able to use *BEAMnrc* VRTs for photon production at the anode. In particular, DBS is extremely useful in this scenario where bremsstrahlung production is very inefficient. This VRT resulted in much larger gains in efficiency than radiative splitting because it allows the user to select a specific direction in which to increase photon production. In addition, bremsstrahlung cross section enhancement is another VRT that can be used in conjunction with DBS to further increase code efficiency. Taking all of this into consideration, the *BEAMnrc* model is something worth exploring alongside the other two.

2.3. Implemented Variance Reduction Techniques

A relatively large emphasis was placed on maximizing MC efficiency in this project, and the best way to do that was by optimizing the various VRTs implemented throughout the different models. As detailed in Section 1.3.2, the defining parameters for each VRT must carefully considered when implementing these techniques. All simulations used for optimization were carried out in a “Lubuntu” Linux virtual machine environment installed on an Acer Windows 10 machine. The system was allotted 11.344 GB of RAM from the 16.0 GB available. All simulations were run with a 2.50 GHz Intel Core i5-7300HQ CPU, with all 4 cores being available for use but parallel processing was never done for the purposes of VRT testing. The specifics of the simulations run for each VRT testing scenario is described later on as the techniques are introduced. But before these simulations can be run, the *EGSnrc* transport parameters, mentioned in Section 1.3.1.1, must be set. For the most part, default transport parameters were used and the only deviations from the default will be discussed here. Starting off, the global electron cutoff energy, ECUT, or the energy at which electrons

are eliminated and their energy deposited, was set to 0.512 MeV for all simulations. The equivalent parameter for photons, the global photon cutoff energy PCUT, was set to 0.001 MeV. In addition, the following options were used for their associated transport parameters:

- Brems Cross Sections = NRC
- Pair Cross Sections = NRC
- Pair Angular Sampling = KM
- Rayleigh Scattering = On
- Electron Impact Ionization = penelope

These transport parameters were chosen with an emphasis on getting accurate results for low energy simulations.

2.3.1. *egs_chamber* VRTs

The *egs_chamber* application is derived from the *cavity* application and therefore can use all of the VRTs implement within that application. Several forms of variance reduction have been implemented directly into the EGSnrc code, and are therefore available for use in some form by all user codes. Namely, this includes range rejection, bremsstrahlung splitting, and Russian roulette (RR) [32], which can all be useful in the *egs++* geometries created in *egs_chamber* in each model. In addition, there have been several VRTs implemented unique to *egs_chamber*, the most relevant of which for these simulations was photon cross section enhancement. Each of these techniques is defined by a set of parameters that must be specified within the variance reduction definition block in the input file. While there are studies that have explored optimal parameter choices for various scenarios [36], it is typically best to optimize one's own model individually. Due to the complexity of the geometries available, as

well as the wide range of possibilities in egs++, the optimal parameter choice will change non-negligibly.

2.3.1.1. Range-based Russian Roulette (RR)

The first VRT to optimize in range-based RR, which focusses on getting rid of excess electrons in the simulation to improve simulation time. The inner workings of the technique works as well as the associated parameters chosen here were discussed in Section 1.3.2.1. To turn on this, a “range rejection” block was defined within the “variance reduction” block in the input file described in Section 1.3.1.1. Within this block, the previously mentioned parameters were defined including: the “range rejection medium” which is the medium used for the electron range calculations, the energy below which range rejection is done E_{save} , the “cavity geometry” where the dose is being scored, and finally the rejection factor N_r . The rejection medium was chosen to be the medium with the lowest restricted stopping power outside the cavity, which was air in all three models. The E_{save} parameter was chosen to be 0.512 MeV in all simulations, preserving electrons with more than 1 keV of kinetic energy. The cavity geometry in all simulations was the same region defined in the calculation geometry block for dose scoring as this is the region of interest in all cases. Finally, the rejection factor N_r required careful consideration before a value was chosen. This parameter was optimized by testing a range of values and calculating the Monte Carlo efficiency in each simulation.

For all optimization simulation sets, a modified version of the SpekPy model was used. The PTW 30010 ionization chamber was placed in the multi-slot phantom placed at the origin. The source was chosen to be a point source of photons collimated to create a 10 cm x 10 cm field at 50 cm SSD. The source was given a spectrum produced by SpekPy for a 250 kV X-ray beam from the X-ray tube installed in the XRAD-320. All simulations were done with 10^8

histories. None of the components of the XRAD-320 were placed in the beam path to simplify the code further and reduce the overall simulation time. The choice was made to do this because the main point where most of the photon are produced and interact is where the ionization chamber is located, so anything along the beam path should not have a significant effect on the simulation time and thus need not be considered when optimizing the VRT.

2.3.1.2. Photon Cross Section Enhancement (XCSE)

Shifting the focus to photons, the XCSE VRT increased the photon interaction cross section by an enhancement factor γ_{XCSE} to increase the number of photons present in the simulation. Enhancement factors were assigned on a region-by-region basis, in particular, for the ionization chamber in a phantom, a thin cylinder surrounding the cylinder and everything inside that region was enhanced. The thickness of the cylinder was chosen with the mean free path (MFP) of electrons in mind because that would cover electrons outside the region that could potentially produce a relevant photon. To estimate the MFP of an electron in a material of interest, the total stopping power at a given energy can be found in the ESTAR database [50] can be used. In the case of the single- or multi-slot phantoms, the air slot region was chosen to be the entire air slot which the ionization chamber is placed in due for simplicity. Finally, one more consideration was made when using this VRT in the models presented. When used in conjunction with range-based RR, the rejection factor N_r could not be greater than or equation to the largest γ_{XCSE} in the geometry (see Section 1.3.2.2).

To enable XCSE, the value of “cs enhancement” was set to 1 in the variance reduction block. The only information provided to the code in this block is whether or not the VRT is enabled. The actual parameters of the VRT were defined in the calculation geometry within the scoring options block. A variable called “enhance regions” was defined within this block

and given a list of indices of regions used in the VRT separated by spaces. Another variable called “enhancement” was used to define the enhancement factor γ_{XCSE} associated with each region. This list of factors had the same length as the number of regions listed in the previous parameter. In addition, so that every listed region had the same enhancement factor, the “enhancement” parameter was set to a single negative value. This was especially useful when the factor was being changed often for optimization in simulations with a large amount of enhanced regions. In terms of the setup for optimizing the enhancement factor, the same simulation used in the previous section was used. Notably, when optimizing one VRT, all other VRTs were turned off such that they could be optimized in isolation.

2.3.1.3. Bremsstrahlung Splitting

The last VRT of importance available in *egs_chamber* is bremsstrahlung splitting, which splits each bremsstrahlung interaction into N_{split} events. To enable bremsstrahlung splitting, the variable “radiative splitting” was defined within the variance reduction block. The value of this parameter was set to the desired splitting number. Note that unlike the other two VRTs, if the radiative splitting factor was set to 0, the simulation skipped bremsstrahlung events entirely instead of turning bremsstrahlung splitting off. When determining values of N_{split} to test, it was important consider that while there is no theoretical maximum on the bremsstrahlung splitting number, there is an internal maximum number of particles allowed on the “STACK” at once, specified by the \$MXSTACK variable defined in the `array_sizes.h` file in the user’s *egs_chamber* directory. The default value of \$MXSTACK is 90,000 so all testing was done with this value set.

To optimize this VRT, a modified version of the `egs++` model was used. The source was chosen to be electrons which would hit the tungsten target in the X-ray tube to produce

photons. Instead of either of the described phantoms, a large 20 cm x 20 cm x 20 cm phantom composed of water was placed 55 cm away from the origin. A smaller pocket of air was created at the center of this phantom for the purpose of dose scoring. Since relatively long simulation times were required to get a good estimate of the overall dose produced by the beam, one of the transport parameters were changed for certain regions. In particular, the electron cutoff energy (ECUT) parameter, which corresponds to the energy at which an electron's trajectory will be terminated and its energy deposited to its surrounding region, was changed in the region around the tungsten target. The ECUT parameter in that region was set to 50 MeV so that any electron that was produced in the phantom would deposit in energy immediately and would be recorded. In addition, several regions in the X-ray tube geometry had their ECUT set to 50 MeV to improve overall simulation time for the testing runs by getting rid of irrelevant electrons. All simulations were carried out with 10^7 particle histories.

2.3.2. BEAMnrc VRTs

The *BEAMnrc* application has a separate set of VRTs implemented that are more geared towards optimizing particle production since its focus lies in simulating linear accelerators. The model described in Section 2.2.1.3 only uses the *BEAMnrc* application for the creation of the XRAD-320 itself, essentially providing a source of photons for the *egs_chamber* application. Therefore, the main thing to optimize is the bremsstrahlung interactions producing our photons. In contrast to *egs_chamber*, *BEAMnrc* was better equipped to deal with inefficient bremsstrahlung photon production because of the VRTs available to the user. Similar to the bremsstrahlung splitting technique, *BEAMnrc* offered the use of DBS, which boasted much larger efficiency gains in comparison. In addition, the VRT BCSE could be used to complement DBS and provide further increases in efficiency.

2.3.2.1. Directional Bremsstrahlung Splitting (DBS) and Bremsstrahlung Cross Section Enhancement (BCSE)

The BEAMnrc model used both directional bremsstrahlung splitting (DBS) and bremsstrahlung cross section enhancement (BCSE) VRTs at the same time. When used in conjunction, the optimal N_{split} value was not the same as it would have been with DBS alone so optimization must be done together. To optimize both techniques for their implementation in the BEAMnrc model, values of N_{split} and f_{enh} were found. It should be noted that the enhancement factor could be defined as either a constant value, or the incident electron kinetic energy dependant quantity that scales with a user defined enhancement power. For ease of optimization, the constant value was chosen. The other parameter that needed to be determined was the radius of the splitting field FS but as mentioned previously this parameter should match the size of the desired field. The field produced for all simulations in this project is 15 cm x 15 cm at an SSD of 50 cm. Therefore, FS was set to 15 cm, as per recommendations in the *BEAMnrc* user manual. The process for finding the optimal N_{split} and f_{enh} combination for a given simulation is detailed in the BEAMnrc user manual and includes the following two main steps:

1. An optimal BCSE factor is chosen based on the simulation type given in Table 1 of Section 6.5.2 of the BEAMnrc user manual. For a simulation in the orthovoltage range, f_{enh} of approximately 100 is recommended. The manual notes that the exact choice of the factor is not important because any loss in efficiency from not picking the exact optimal number will be made up for by finding the optimal N_{split} value.

2. Iterate through DBS splitting factors (N_{split}) and calculate MC efficiency for each simulation. Then fit calculated values to the quadratic function shown in Equation 11.

The derivation of the function being fitted is explained in Ali & Rogers 2007 [40].

$$\frac{N_i}{\epsilon} = A_2(N_i - 1)^2 + A_1(N_i - 1) + A_0 \quad (11)$$

With the A_0 and A_2 parameters from the quadratic, the optimal N_{split} value, denoted N_{split}^{opt} , can be found through the following equation:

$$N_{split}^{opt} = \sqrt{\frac{A_0}{A_2}} \quad (12)$$

For the optimization process described above, the same simulation set up used to optimize bremsstrahlung splitting in the previous section was used. The only difference being that the source was now an “egs_beam_source”, the same as the one used in the BEAMnrc model. This was placed in the geometry such that a 15 cm x 15 cm field was created at an SSD of 50 cm. One final logistical thing to note when doing this optimization was that the default maximum for the splitting number was 2,000, as set by the \$MAXBRSPLIT variable. This option could be changed by accessing the beamnrc_user_macros.morfran file found in \$HEN_HOUSE/omega/beamnrc. For all simulations run in this thesis involving *BEAMnrc*, \$MAXBRSPLIT was set to 2,000,000.

2.4. Procedures for Model Validation

Once completely built, all three models underwent validation through inter-model comparisons, as well as by comparisons to laboratory measurements. All measurements used for validation in the following sections were normalized in order to compare them to the values output by EGSnrc. The simulations used for validation were not run on the same

computer as the simulations used to optimize the variance reduction techniques discussed in Section 2.3. All simulations in this section were run on the Carleton Physics Research Compute Cluster, which is composed of several components:

- EGS component: 53 dual-CPU, Dell 1950 servers with 8 GB each, 244 cores
- ATLAS component: 51 dual-CPU, quad core Dell 1950 servers with 8 GB each, 376 cores
- Processing units: 1 dual-CPU, Dell R630, 24 cores

To make full use of this computational power, simulations were run in parallel, which refers to splitting a simulation into smaller simulations and running them simultaneously to combine the results later. For example, a single simulation could be split across 10 cores and each core would run a tenth of the total histories, effectively making the simulation 10 times faster to complete. The number of cores used for each simulation were chosen based on the estimated time predicted for a given simulation. Enough cores were used to reduce the simulation time to somewhere in the range of 2-10 hours, with a majority of simulations being run in around 4 hours. In addition, the same EGSnrc transport parameters described in Section 2.3 were used in all simulations here.

2.4.1. Spectral Comparison

The first phase of validation began with a cross comparison between models. There are many metrics that define an X-ray machine simulation that could be used here for the cross-validation, one of which being the X-ray spectra being output. To score the spectra, each model was moved to the cavity user code. Being the progenitor of *egs_chamber*, cavity is capable of receiving the same inputs that were fed into *egs_chamber*. All of the geometry definitions created in *egs_chamber* were easily transferred, only changing the scoring options block for the

input files for the two user codes. In this block, when the half-value layer (HVL) or free air chamber (FAC) calculation type was chosen, a fluence scoring block could be defined. Within this block the following parameters must be defined: minimum energy, maximum energy, bin size, and scale. The photon fluence was scored through a pre-defined circle of radius R around the point of measurement. The position and normal vector of this circle was specified within either the HVL or FAC scoring blocks. Since the spectrum was the only output required from this code, the values for the rest of the inputs in the HVL or FAC scoring blocks were required for the code to run but did not effect the spectra output so they were given random placeholder values.

To calculate the differential fluence ϕ_j for particles between energies E_j and E_{j+1} , the sum of the track lengths of all particles l_i crossing through the sampling volume V were used in Equation (13) below.

$$\phi_j = \frac{\sum_{i=1}^{N_j} l_i}{V} \quad (13)$$

In addition, using Equation (14) these differential fluences were summed to produce and report the total fluence:

$$\Phi = \sum_{j=0}^{N-1} \phi_j \quad (14)$$

The number of bins N in both equations was defined in the fluence scoring block, as well as the minimum and maximum energy values being sampled. The output spectra was scored in this fashion and extracted for any source and geometry defined within cavity. Therefore, once all 3 models were moved to *cavity*, several different spectra were produced. First, a spectrum

was produced for just the X-ray tube alone, where everything in the beam path other than the collimators were set to air. This served as a good initial point of validation and could also be used to replace the X-ray tubes from the BEAMnrc and egs++ models with point sources. Then, the spectra produced with each filter in place was scored and compared across all models. The spectra from the BEAMnrc model and the SpekPy model were simulated with 10^9 histories, while the egs++ model spectra were produced using 10^8 histories as the simulation times were too large with higher histories and that amount of particles produced sufficient data.

2.4.2. Phantom & Filter Comparison

The first set of laboratory validations involved comparing the dose recorded in each of the two variations of phantom described in Section 2.1.3. Measurements were taken with the ionization chamber placed at the same point within each phantom. For the slab phantom, the ionization chamber was placed as far into the phantom as possible, and this same position relative to the beam was replicated in the single-slot phantom. Since the cavity extends much further into the phantom for the single-slot, the ionization chamber was pulled back into position, and the wire was taped down to secure it in place during irradiation. The location of the ionization chamber within the phantom models created using egs++ geometry can be seen in **Figure 13**. All measurements were taken with the ionization chamber placed at an SSD of 50 cm and the field size was chosen to be 15cm x 15 cm. The X-ray tube current was also held constant at 10 mA for all measurements. Each setup had 4.5 cm of build up material above and below the ionization chamber, most being RW3, and some being polystyrene in the case of the multi-slot phantom. Finally, the temperature and pressure of the room was recorded at the beginning of the measurement session to be used later if required.

Measurements were taken for with the ionization chamber placed in each phantom, while changing the filtration and energy. The energies chosen to be studied were 200 kV, 250 kV, and 300 kV. At each of these energies, measurements with no filtration (denoted filter 0), filter 1, filter 2, and filter 3 were each taken in triplicate and averaged. The accumulated reading on the electrometer after each exposure was recorded and a ratio was taken for each unique measurement in the multi-slab phantom with the equivalent measurement in the single-slot phantom. The same set of laboratory measurements taken in the previous subsection were also used here to compare outputs between filters with the phantom held constant. For each energy value, the dose output from filters 1, 2, and 3, were normalized to the dose with no filtration in place. All simulations used for validation replicated the experimental setup described and were carried out for both models with 10^9 histories. The details of the VRT parameters used are discussed later.

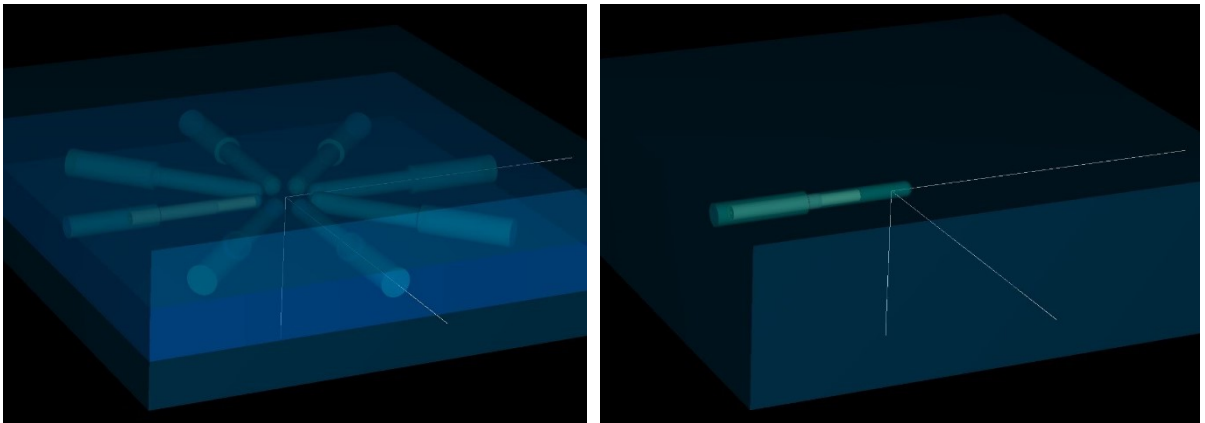


Figure 13: Solid water phantoms created in EGSnrc using egs++ geometry. Multi-slot phantom shown on the left, single-slot on the right. The ion chamber can be seen in both phantoms, placed at the same position relative to the origin.

2.4.3. HVL Validation

A standard way to characterize an X-ray beam is through the calculation of its HVL for a given material. The HVL is defined as the thickness of a material which will attenuate a beam of radiation to half of its original intensity. Radiation intensity is attenuated exponentially in the case of a mono-energetic beam but for a more complex source, the attenuation changes and can't be fit by a simple exponential. Therefore to find an accurate estimate of the HVL, an attenuation curve must be fit with a much more complicated function, ideally a smooth curve through each of the data points. A cubic spline interpolation was used in MATLAB R2019b, which involved fitting many cubic piecewise polynomials to produce a smooth curve. Other fits in MATLAB were explored but the cubic spline appeared to produce the best results so all HVL value estimations were done with this fit.

For the HVL measurements in the laboratory, dose was measured at 50 cm SSD from a 15 cm x 15 cm field in the multi-slot phantom. All measurements were taken with Filter 1 in place. To produce differing thicknesses of copper, sheets of copper were taped on to the end of the beam path in the same way a piece of metal is taped to the end of the machine for the creation of Filter 3. The thickness of copper were chosen based on the availability in the laboratory which were 0.5 mm, 1.0 mm, 2.0 mm, and 2.5 mm. In terms of incorporating this into the simulations, the input file for each model with filter 3 was slightly modified. This piece of metal secured to the end of the XRAD-320 is already defined in these input files so the only thing that needed to be changed was the thickness and composition of the sheet. For all simulations 10^9 histories were used with the exact same setup from the lab.

3. Results

3.1. Code Optimization Results

Due to the complex geometries involved, producing dose outputs with reasonably low uncertainties involved a large amount of computational time for all three models. In addition, each unique geometry created within EGSnrc had a unique set of circumstances that effected the optimal value that defines a VRT. Therefore it was important to optimize the parameters in each VRT on a simulation-to-simulation basis. Optimal VRT values were assessed early in the project with the initial geometry definition, however, throughout the course of the project, the geometry was edited as new information was gathered about the setup. In the end, it was determined that enough of the geometry was changed to warrant a reassessment of the optimal VRT values found at the beginning of the project. Where applicable and relevant, both sets of results are considered to analyze the effect that slight changes in geometry had on VRT techniques used in EGSnrc.

For each efficiency result presented here, wherever possible, each value graphed is normalized to the efficiency or dose value determined without VRT's enabled. This provides a gauge of the impact of the technique on the simulation since the absolute efficiency quantity is a value with little context. In addition, this allows for comparison between the efficiency gains provided by each technique above their respective non-optimized simulation.

3.1.1. Range-based Russian Roulette (RR)

There are several options of values to optimize when using range rejection in *egs_chamber*, but the most important value is the rejection factor N_r . This factor determines the probability that a given electron survives a game of RR played when conditions as described

in Section 2.3.1.1 are met. The results from the preliminary phase of testing is shown in **Figure 14a**, where the efficiency corresponding to rejection factors ranging from 0 (which corresponds to the simulation where no variance reduction was used) to 64 are plotted. The normalized efficiency appears to follow no discernable trend in this range of rejection factors, providing a maximum efficiency increase of 1.3 at a factor of 45. **Figure 14b** shows the dose output tracked across rejection factors normalized to the dose output with no VRT, which shows that almost all rejection factors are within uncertainty of the dose calculated with no variance reduction. When further rejection factors were tested, the efficiency decreased until it reached a value of around 1 and it remained there with increasing rejection value. This is reflected in **Figure 15**, where rejection values up to 256 were used in the same simulation setup, but when looking past a rejection factor of 64 there appears to be no efficiency gain from using range-based RR.

Once the single-slot phantom was introduced, as well as the steel stage on which the phantoms rest, this VRT was reassessed in a final phase of testing. The presence of the steel stage underneath the phantom brings about concerns of increased irrelevant electron production which could lead to larger efficiency gain. Using the exact same simulation parameters as from the preliminary phase, apart from the new geometry, the MC efficiency of various rejection values up to 64 were assessed and plotted on **Figure 16a**, along with the dose value being tracked on **Figure 16b**. The normalized dose is always within the uncertainty of the simulation with no variance reduction in place. The trends seen in the MC efficiency are a lot less erratic than in **Figure 14a**, with the efficiency rapidly increasing to a maximum at a factor of 32, providing a relative increase of 2.25. Furthermore, examining rejection factors up to 2,048 (**Figure 17**) shows a lack of the efficiency drop-off seen previously. For the larger set of rejection factors, the relative MC efficiency hits a maximum of 2.27 at the largest factor

plotted, 2,048. Overall, the efficiencies relative to the no VRT simulation are marginally higher in this new geometry setup, typically averaging around 2.0-2.2 at large factors. Despite the efficiencies only being marginally higher in the final phase of testing, the most important observation found here is that the efficiency gains do not drop off at high rejection factors. This will be useful when combining with the next VRT that was optimized, XCSE.

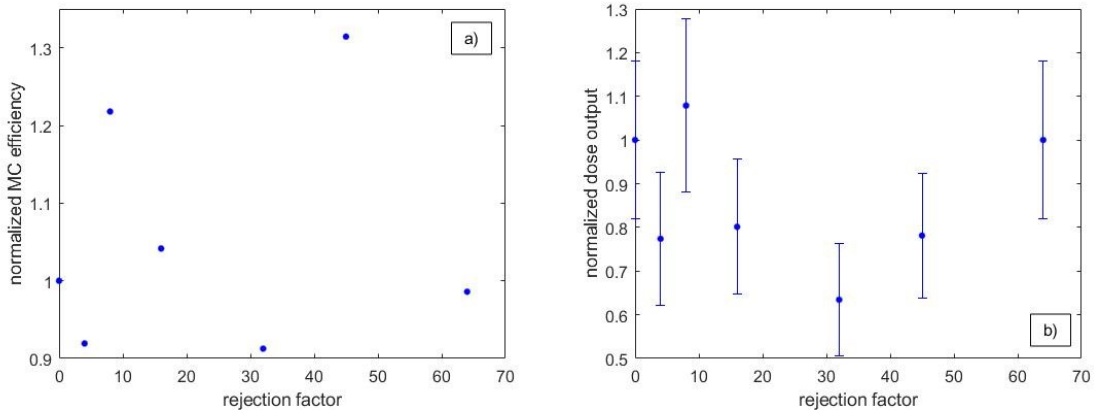


Figure 14: Results from the preliminary phase of optimizing range-based RR. a) MC efficiency normalized to the efficiency with no VRT is plotted against rejection factor with a polynomial fit overlaid. b) The dose output normalized to the output with no VRT is plotted against rejection factor to track the variation in output with increasing rejection factor.

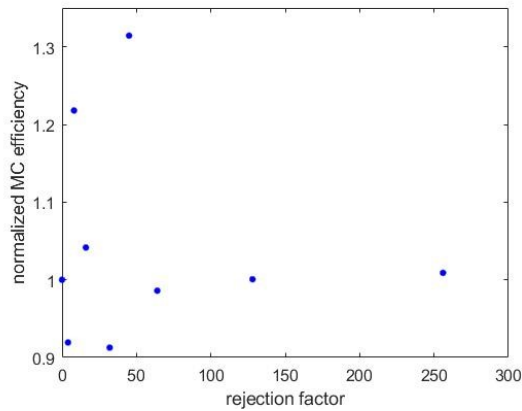


Figure 15: Normalized MC efficiency plotted against rejection factor for the preliminary phase of testing considering a larger range of factors than presented previously in Figure 14a.

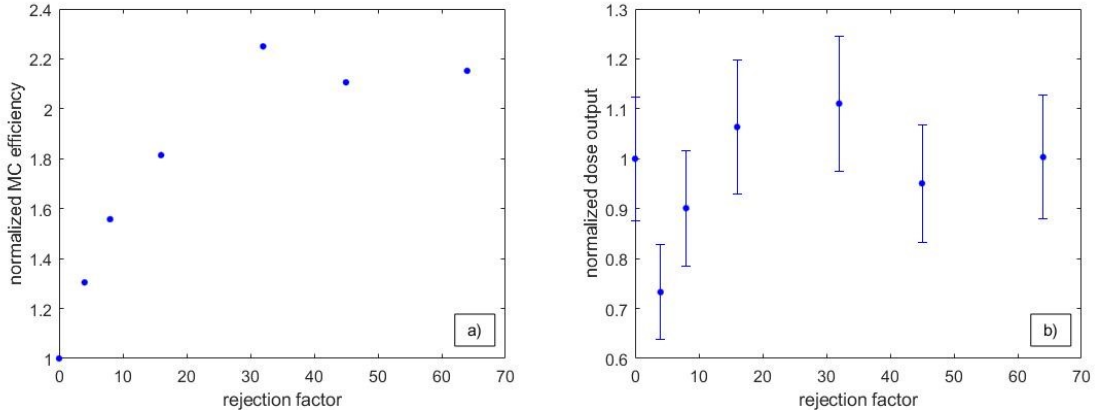


Figure 16: Results from the final phase of optimizing range-based RR with a new geometry setup. The normalized MC efficiency corresponding to rejection factors are shown in a), and associated dose output normalized to the output with no range-based RR in place in b).

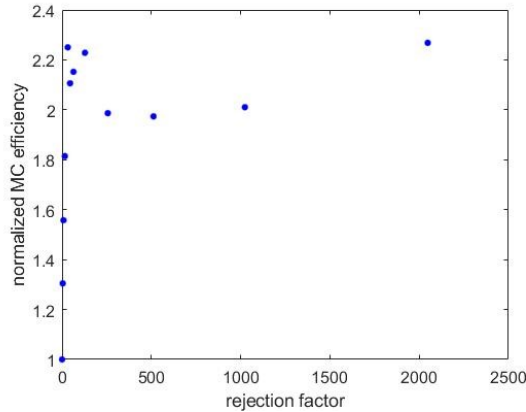


Figure 17: Normalized MC efficiency plotted against rejection factor for the final phase of testing considering a larger range of factors than presented previously in Figure 16a.

3.1.2. Photon Cross Section Enhancement (XCSE)

The main focus in XCSE is the enhancement factor γ_{XCSE} , the factor by which the interaction cross section of photons is artificially increased. To find an optimal value, a large range of values were assessed as efficiency was found to continuously increase until a factor of around 600, when the efficiency started to plateau and drop off. A plot of this optimization can be seen on the left of **Figure 18a**, with the dose as a function of γ_{XCSE} plotted in **Figure 18b**. A general polynomial like trend can be seen in this efficiency curve, similar to the rejection curve seen in the previous section. Notably there is a lot less variation with increasing factor

values, producing a better fit. This data set was fit with a 2nd degree polynomial to find the factor that maximizes the MC efficiency, plotted on top of the data points in **Figure 18a**. The efficiency values span a large range and from the fit, the optimal γ_{XCSE} value is calculated to be 677, corresponding to an efficiency gain of approximately 138. Reviewing the normalized dose values in **Figure 18b** for each of these XCSE factors, they are found to be consistent with the value found in the simulation with no VRT.

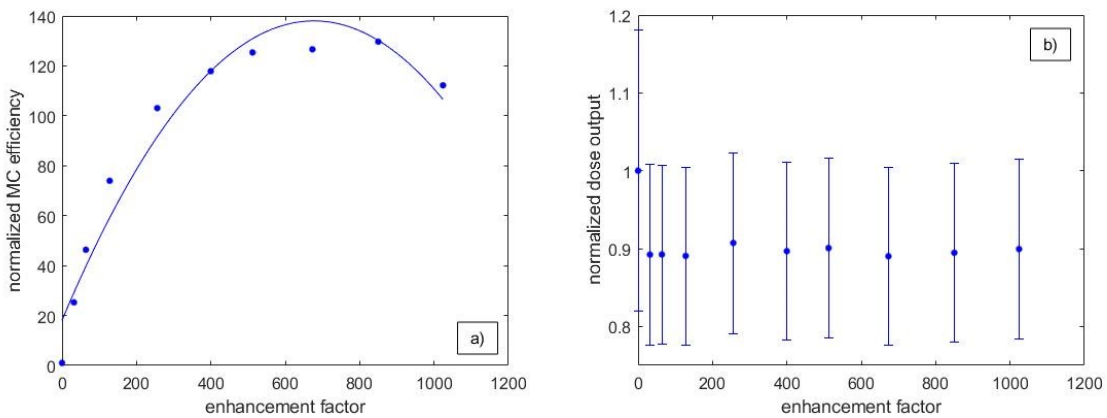


Figure 18: Results from the preliminary phase of optimizing XCSE. a) MC efficiency normalized to the efficiency with no VRT is plotted against the enhancement factor with a polynomial fit overlaid. b) The dose output normalized to the output with no VRT is plotted against the enhancement factor to track the variation in output with increasing rejection factor.

With the addition of the steel stage, the optimization simulations were rerun with the multi-slot phantom. This phantom was used instead of the single-slot phantom used in the final phase of optimization in the previous section because it is more complicated and was thought to benefit more from this VRT. The results can be seen in **Figure 19a**, where larger γ_{XCSE} factors were tested in addition to the previously tested set. The efficiency gain in this new geometry from XCSE is notably larger, reaching values of 250 before starting to decrease. Again, using a 2nd degree polynomial fit, the optimal value was calculated to be 1,388, corresponding a relative efficiency gain of 319. The normalized dose output value was again tracked for every simulation in **Figure 19b**, and all values fall within uncertainty of the original

simulation with no variance reduction implemented. Therefore, the general consensus from both phases of testing is that large values of the XCSE factor will provide substantial efficiency gains without having an effect on dose. In addition, the curve plateaus near the maximum efficiency value, meaning that there are a range of XCSE factors that would provide efficiency gains very close to the maximum value.

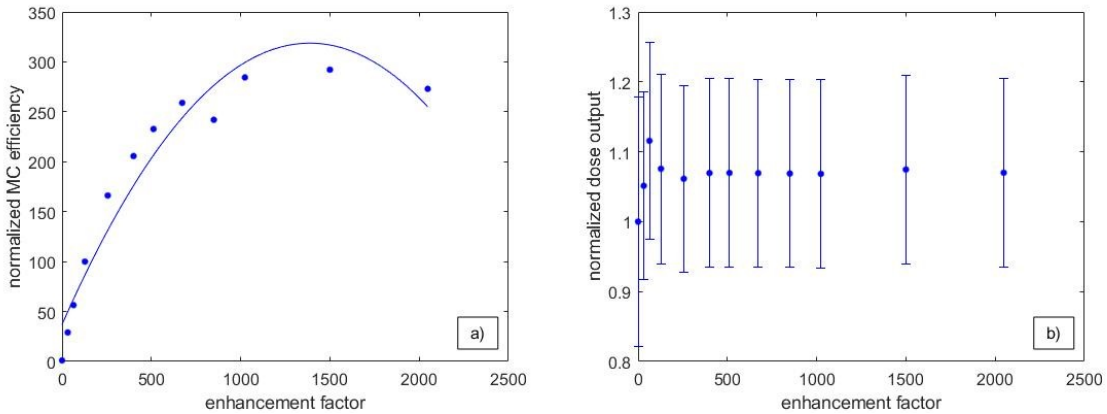


Figure 19: Results from the final phase of optimizing XCSE with a new geometry setup. The normalized MC efficiency corresponding to enhancement factors are shown in a), and associated normalized dose output in b).

3.1.3. Bremsstrahlung Splitting

The bremsstrahlung splitting VRT is focussed around the point of X-ray production at the tungsten anode in the X-ray tube, increasing the photons output from a single bremsstrahlung event. The only parameter needed here is the splitting number N_{split} so a range of values were chosen and tested for a simplified version of the egs++ model. The normalized efficiencies of these simulations are shown in **Figure 20a**, with the dose being tracked in **Figure 20b**. Visually inspecting the graph, there is no clear trend similar to those seen for the two previous VRTs optimizations, therefore no fit was applied. There is, however, a clear splitting number that produced the largest efficiency in the range tested. With N_{split} set to 100, the relative MC efficiency reached its maximum of 6.29. Looking at the dose outputs corresponding to these values, there appears to be a clear and large discrepancy

between the dose output with no variance reduction, and all the doses when bremsstrahlung splitting is turned on. All of the doses recorded with this VRT enabled are within uncertainty of one another, but the average dose when this technique enabled was found to be over 14% higher than the simulation with no VRT.

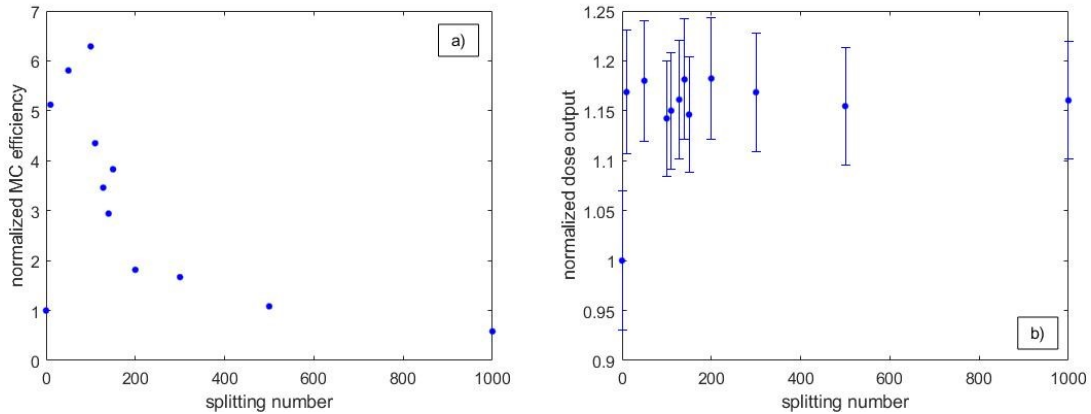


Figure 20: Results from the preliminary phase of optimizing the radiative splitting number for the bremsstrahlung splitting VRT. a) MC efficiency is plotted against splitting number. b) Normalized dose output is tracked against splitting number.

As the model of the XRAD-320 itself was updated, with the components within it being adjusted, these tests were rerun. In addition, the regions in the X-ray tube that had their ECUT value set to 50 MeV to reduce the simulation time were reset to the global ECUT value, as it was suspected this might have created the dose discrepancy seen in **Figure 20b**. Since the fundamental point of optimization, the bremsstrahlung production at the tungsten target, never changed, only a few values of N_{split} were retested to check whether the optimal value could have changed from the minor geometrical changes to the XRAD-320 body. The efficiency gain from enabling bremsstrahlung splitting was found to be marginally larger, with the largest relative gain being 7.93 at a splitting number of 50 (**Figure 21a**). In addition, it is important to note that the relative dose values for the cases with bremsstrahlung splitting enabled are now within uncertainty of the simulation with no VRTs, seen in **Figure 21b**. This is an important distinction from the previous set of tests. Therefore, from the final phase of

testing, this VRT has been confirmed to have a minimal influence on the dose and provide good efficiency gain for an optimal splitting value of 50. Similar to the previous VRT, there does appear to be a range around the maximum efficiency point that would provide similar levels of efficiency gain, providing flexibility in the choice of splitting number.

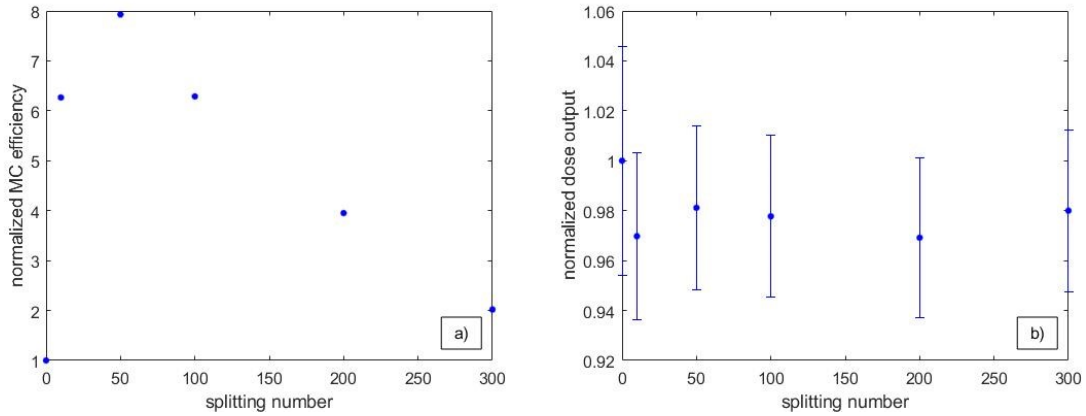


Figure 21: Results from the final phase of optimizing the radiative splitting number for the bremsstrahlung splitting VRT. a) MC efficiency is plotted against splitting number. b) Normalized dose output is tracked against splitting number.

3.1.4. Directional Bremsstrahlung Splitting (DBS) combined with Bremsstrahlung Cross Section Enhancement (BCSE)

When using DBS with BCSE, they must be optimized together. The best way to perform this is to hold the parameters of one of these values constant and optimize the other. Based on recommendations given in the BEAMnrc user manual [34] the enhancement factor was set to 100 and a range of splitting numbers were tested to evaluate efficiency. Following the procedure detailed in the BEAMnrc manual and described at the end of Section 2.3.2.1, **Figure 22A** was created by using a range of N_{split} values.

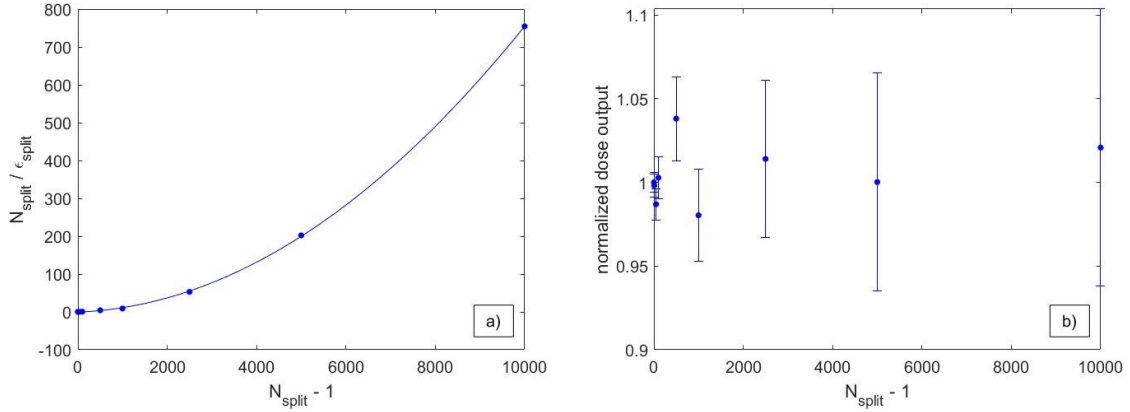


Figure 22: Results from optimizing the DBS VRT when combined with the BCSE VRT at an enhancement factor of 100.

From the quadratic fit in **Figure 22a**, the following coefficients for Equation 11 were found to be used in the optimization calculation:

$$\begin{aligned}
 A_2 &= 7.098 \cdot 10^{-6} \\
 A_1 &= 4.550 \cdot 10^{-3} \\
 A_0 &= 4.216 \cdot 10^{-1}
 \end{aligned}
 \tag{15}$$

Using Equation 12 defined in Section 2.3.2.1 for the optimal directional bremsstrahlung splitting number, N_{split}^{opt} was calculated to be:

$$N_{split}^{opt} = \sqrt{\frac{A_0}{A_2}} = 244
 \tag{16}$$

Therefore, based on this analysis, the optimal splitting number is 244 for an enhancement factor of 100. As with the previous VRT optimizations, the dose output and associated uncertainties were also tracked for each of these simulations and plotted in **Figure 22b**. Notably, these dose values are not normalized to a simulation with no VRT in place unlike all dose tracking graphs shown previously. The values were still normalized, but to a N_{split} value

of 10. This is due to the fact that the simulation without VRT was too long to be run in a reasonable amount of time and was not required for the analysis to determine N_{split}^{opt} . Nonetheless, it was still possible to examine how the doses plotted compared to each other to ensure that changing the DBS splitting number did not have a large impact on the dose. In general, the uncertainty was found to increase with increasing splitting number but all the dose values plotted were within uncertainty of each other.

3.1.5. Summary of Optimal VRT Parameters

With all of the VRT optimization calculations complete, all VRTs explored in this thesis were found to have optimal values that should be used when they are implemented. These values are summarized in **Table 2**. There were typically two phases of testing done for each VRT, a preliminary and a final, where the final phase was done after the geometry was updated, providing two separate optimal values of the VRT parameter. Both of these quantities are provided in the table to highlight the change in factor between phases of testing. In addition, the table indicates which EGSnrc model uses each VRT optimized. All models use range-based RR and XCSE, while bremsstrahlung splitting is unique to the egs++ model, and DBS combined with BCSE are unique to the BEAMnrc model. Also listed in the table are the values implemented in the input files used for validation in Section 3.3 and most are seen to differ from the final optimal value calculated. This is explored further on in the thesis in Section 4.1.4.

Table 2: Summary of VRT analysis, showing optimal parameters found (for both preliminary and final testing phases) compared to what was actually implemented and which models they were implemented in.

VRT	Variable	Calculated Optimal Value	Implemented Value	Used in model?		
				egs++	SpekPy	BEAMnrc
Range-based RR	N_R	Prelim.: 45 Final: 2,048	512	Yes	Yes	Yes
XCSE	γ_{XCSE}	Prelim.: 677 Final: 1,388	512	Yes	Yes	Yes
Brems. Splitting	N_{split}	Prelim.: 100 Final: 50	100	Yes	No	No
DBS	N_{split}	Prelim.: N/A Final: 244	1,000	No	No	Yes
BCSE	f_{enh}	N/A	100	No	No	Yes

3.2. Inter-model Comparison

Before validation was done against measured laboratory results, it was important to do a simple comparison across all three models. Since there are variations in the techniques used to produce each X-ray spectrum, as well as differences in the VRTs that are applied, checking the agreement of the spectra produced would ensure consistency.

3.2.1. Spectral comparison

Several spectra can be compared from each model with varying levels of filtration and energies. The first spectrum produced for comparison is the spectrum output from the MXR-321 X-ray tube. As mentioned, the reasoning for this is that if the spectra here do not match, there is a fundamental mismatch between each of the models that must be addressed before moving forward. The output spectra from each of the three models can be seen in **Figure 23a** for the typical operating energy of 250 kV. There appears to be no noticeable difference in the locations of the peaks of the spectra produced by each model, however there is a slight difference in the magnitude of the peaks. The SpekPy model produces the largest peaks, followed by BEAMnrc, and then egs++ models. This difference can be more clearly seen in

by subtracting the spectra from each other. Since the egs++ model was the first model used, the other two spectra were subtracted from its spectrum for a closer comparison. The resulting spectra can be seen in a semi-log plot on **Figure 23b** and further visually confirm the prior observations. A general observation that becomes clear when looking at the subtracted spectra is the relatively large fluctuations in the egs++ spectrum compared to the relatively smooth BEAMnrc and SpekPy spectra. In addition to the typical operating energy of 250 kV, two other energies were used to produce spectra. The spectra X-ray tube operating at 200 kV can be seen in **Figure 24**, and the spectra at 300kV are shown in **Figure 25**. Similar observations can be made in that the spectra match well except at the peaks where small differences in magnitude can be seen.

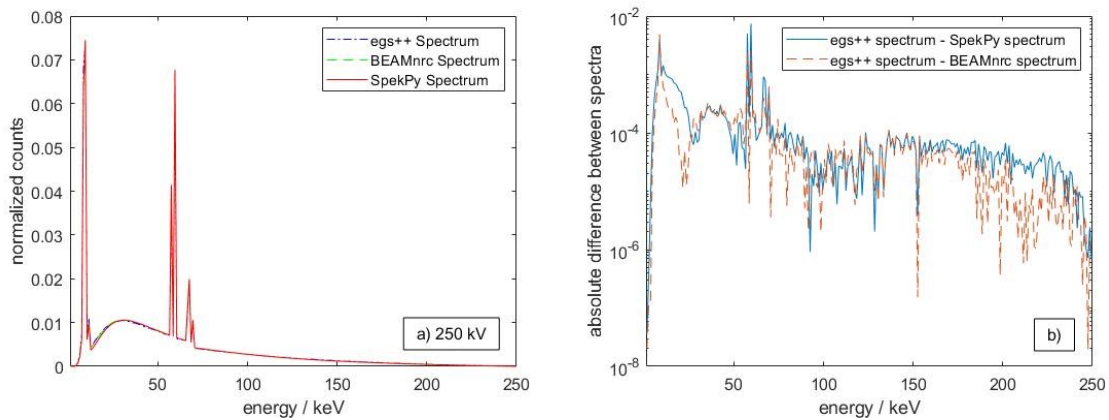


Figure 23: Comparing spectra produced by all three models with only the MXR-321 simulated in vacuum at 250 kV. The spectra are overlaid in a), and the difference between the egs++ model and the SpekPy and BEAMnrc models are shown in b).

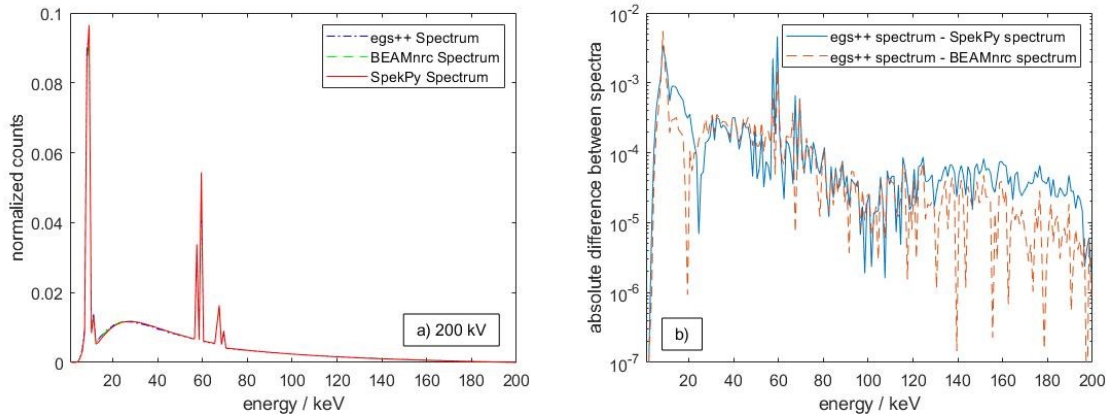


Figure 24: Comparing spectra produced by all three models with only the MXR-321 X-ray tube simulated in vacuum at 200 kV. The spectra are overlaid in a), and the difference between the egs++ model and the SpekPy and BEAMnrc models are shown in b).

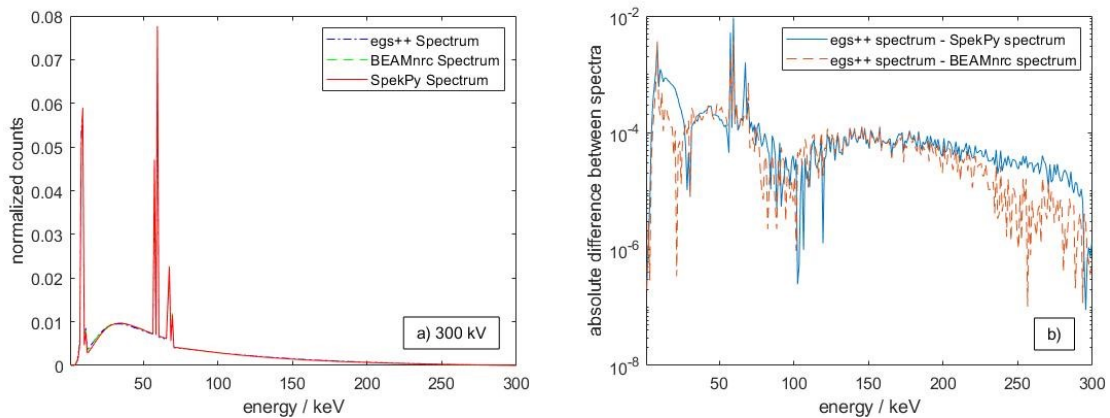


Figure 25: Comparing spectra produced by all three models with only the MXR-321 X-ray tube simulated in vacuum at 300 kV. The spectra are overlaid in a), and the difference between the egs++ model and the SpekPy and BEAMnrc models are shown in b).

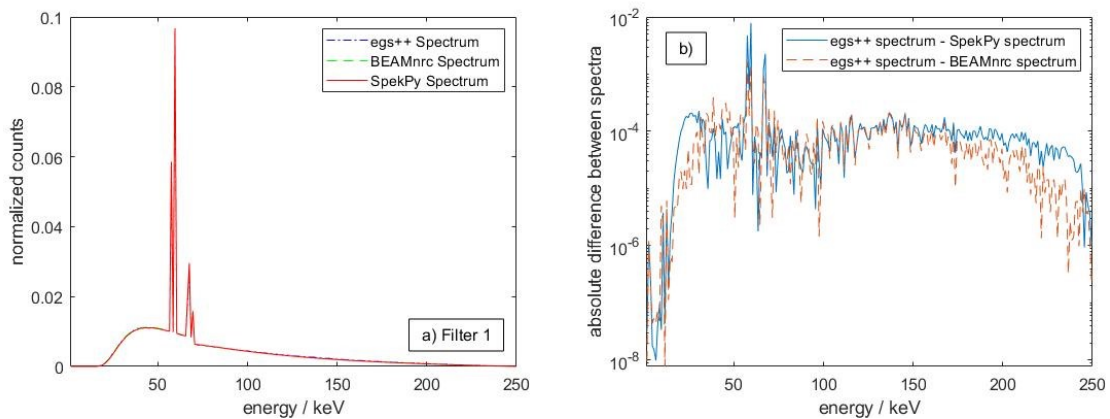


Figure 26: Comparison of spectra produced by each model for the full XRAD-320 simulated with Filter 1 in place. The spectra are overlaid in a), and the difference between the egs++ model and the SpekPy and BEAMnrc models are shown in b).

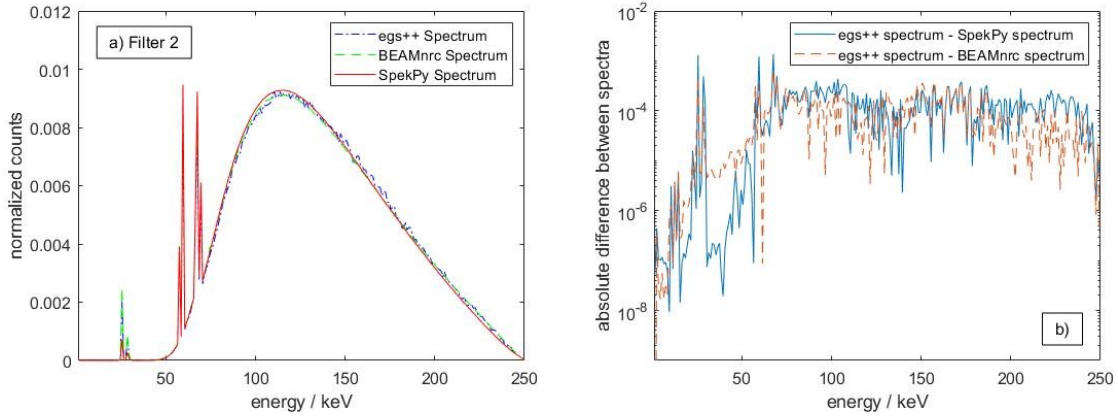


Figure 27: Comparison of spectra produced by each model for the full XRAD-320 simulated with Filter 2 in place. The spectra are overlaid in a), and the difference between the egs++ model and the SpekPy and BEAMnrc models are shown in b).

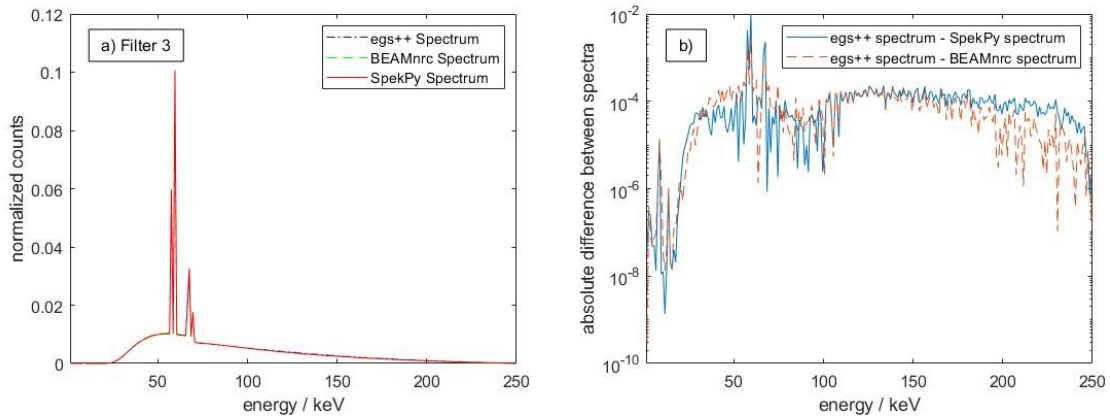


Figure 28: Comparison of spectra produced by each model for the full XRAD-320 simulated with Filter 3 in place. The spectra are overlaid in a), and the difference between the egs++ model and the SpekPy and BEAMnrc models are shown in b).

Next, the spectra produced with the entire XRAD-320 geometry and each of the three filters in place was plotted for each model. The plots can be seen in **Figure 26**, **Figure 27**, and **Figure 28** for filter 1, filter 2, and filter 3, respectively. Similar to the previous set of plots, the spectra from the BEAMnrc and SpekPy models were subtracted from the egs++ model for ease of comparison. The general trend as the level of filtration increases (Filter 1 \rightarrow Filter 3 \rightarrow Filter 2) is that the spectrum shifts more and more towards higher energies, with the lower part of the spectrum being selectively filtered out. In the most filtered beam, the characteristic X-ray peaks have reduced in magnitude to the point of being comparable to the rest of the

spectrum, further indicating the shift towards higher energy photons. In addition, on both graphs for this beam in **Figure 27**, relatively large fluctuations can be seen in the egs++ spectrum in comparison to the other spectra. This is further reflected on the subtracted spectra on the **Figure 27b**.

For all levels of filtration, the spectra appear to match well between all three models with some discrepancies seen at lower energies as well as the characteristics peaks seen similar to the previous spectra. Notably, the egs++ spectra appear to become less and less smooth as the level of filtration increases, which can be seen when comparing the graphs on the right.

3.3. Validating Models with Laboratory Results

With the models compared, the next step is to validate them by evaluating their level of agreement with laboratory measurements. This was done through a phantom comparison, a filter comparison, as well as an HVL calculation. Each of these forms of validation serve a purpose in examining different parts of the model to help diagnose any potential discrepancies that might be seen between the simulations and laboratory measurements. Before this can be done, the setup error must be estimated to provide better context to the values measured in the lab.

3.3.1. Setup Error Estimation

The uncertainties on the measurements made in the laboratory must be accurately estimated before they can be compared to the simulated values. The main unknown error quantity in this setup is the error introduced from setting up the phantom and ionization chamber in the correct position for irradiation in each measurement instance. To do this, a setup error scaling was derived for error in SSD and field size. In addition, a setup consistency

check was done as an independent way of gauging the error in the setup for comparison to the scaling method.

The results of the error scaling estimation can be seen graphically for the SSD in **Figure 29**, and for field size in **Figure 30**. Note that since square fields were being used for field size, the value being tracked as a surrogate for field size is the side length. Each set of data for the SSD and field size error analyses were fit with lines to approximate their relationship to the electrometer reading. The slope in **Figure 29** was found to be -1.897 nC/cm , indicating that the dose output decreases with increasing SSD. As for the field size effect, **Figure 30** shows a slope of 1.191 nC/cm for the linear relationship between field size and electrometer reading, indicating an increase in dose with field size. These values can be converted to uncertainties by estimating the margin of error on determining either the SSD or the FS. This was determined to be approximately 0.05 cm for both SSD and FS by considering the measurement devices used to set these values. As a result, an error value of 0.190 nC was added to account for variation in SSD, and for FS an addition error value of 0.119 nC was considered. This error estimation was done with filter 1 in place and with the ionization chamber placed in the multi-slot phantom, so these static values were converted to percentage errors by using measurements done with this same setup used for validation later. The percentage error for SSD was calculated to be 0.186% and 0.118% for field size. Since these are independent error values, they can be combined in quadrature ($\sigma_{setup} = \sigma_{SSD} \oplus \sigma_{FS}$) to produce a total combined setup error estimate. The combined setup error was calculated to be 0.219% to be incorporated into each electrometer reading.

To check the validity of this error scaling, the reproducibility of each measurement was checked through repeat measurements of the same quantity but with the entire setup being

moved out and back into position before each measurement. Averaging the five measurements taken produced a standard deviation of 0.036 nC, which is approximately 0.184% of the average. Comparing this to the combined error from the scaling calculation, the scaling calculation is slightly higher but the difference is relatively small. Therefore, the error on all laboratory measurements was a combination of the statistical error and the setup error.

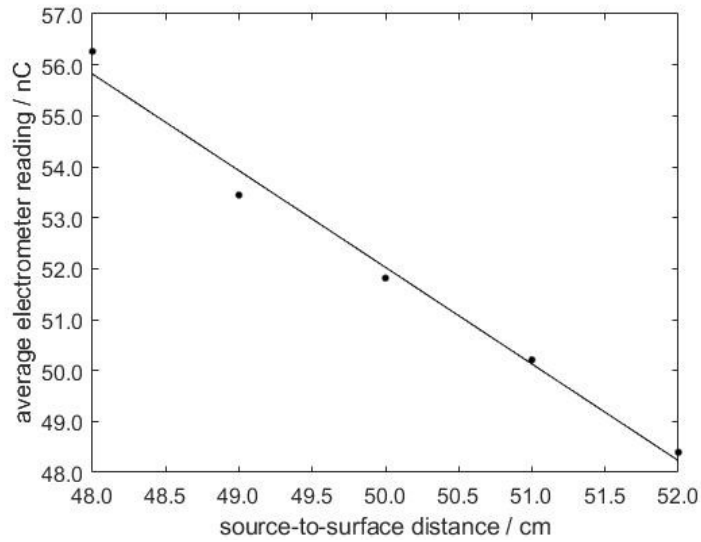


Figure 29: Estimation of the error contribution from setting the source-to-surface distance using a linear fit. Statistical error bars on quantities too small to be pictured.

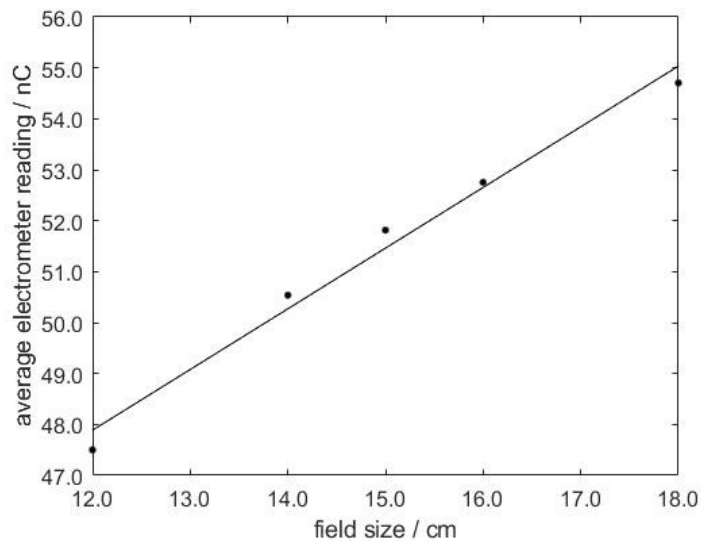


Figure 30: Estimation of error contribution from setting field size using a linear fit. Square fields were always used with the field size values plotted corresponding to a side length. Statistical error bars too small to be pictured.

3.3.2. Phantom Comparison

The first point of validation for the BEAMnrc and SpekPy models was an output ratio comparison between the two types of phantoms defined previously. The electrometer reading recorded in the multi-slot phantom was divided by the reading recorded in the single-slot phantom to produce the following ratio:

$$\text{Ratio} = \frac{\text{Multi-Slot Phantom Output}}{\text{Single-Slot Phantom Output}} \quad (17)$$

This ratio was evaluated in the laboratory and calculated in EGSnrc using the two models for validation. This was done for all three filters previously described, and for three different energies: 200 kV, 250 kV, and 300 kV. These ratios can be seen in the form of three graphs, one for each energy, in **Figure 31a**, **Figure 31b**, and **Figure 31c**, respectively.

The main overall trend seen for almost every ratio is that using the multi-slot phantom produces a noticeably higher dose than the single-slot phantom. This is especially significant for low attenuating filters such as filter 1, where the ratio between multi- and single-slot phantoms reaches a high of 1.0674 ± 0.0046 for the laboratory measurement at an energy of 200 kV. As energy increases, the general trend seen is that the ratio decreases for all filters. To statistically compare the values from the simulations to the lab, a Student's t-test was used to calculate t-value for each data point for the BEAMnrc and SpekPy models. For the 200kV dose output ratios, both models were found provide values statistically consistent with laboratory measurements except for filter 3 in the BEAMnrc model, which was slightly underestimated. For 250 kV in the BEAMnrc model, only the ratio for filter 2 agreed with laboratory measurements within uncertainty, and for the SpekPy model, both filters 1 and 2 were within uncertainty. Finally for 300 kV, all dose output ratios for both models were found

to be within uncertainty of the laboratory measurements. In summation, both models performed at a similar level, with SpekPy outputting slightly more accurate ratios in some cases than BEAMnrc. In general, dose output ratios between the two phantoms for most cases were accurately reproduced by the models.

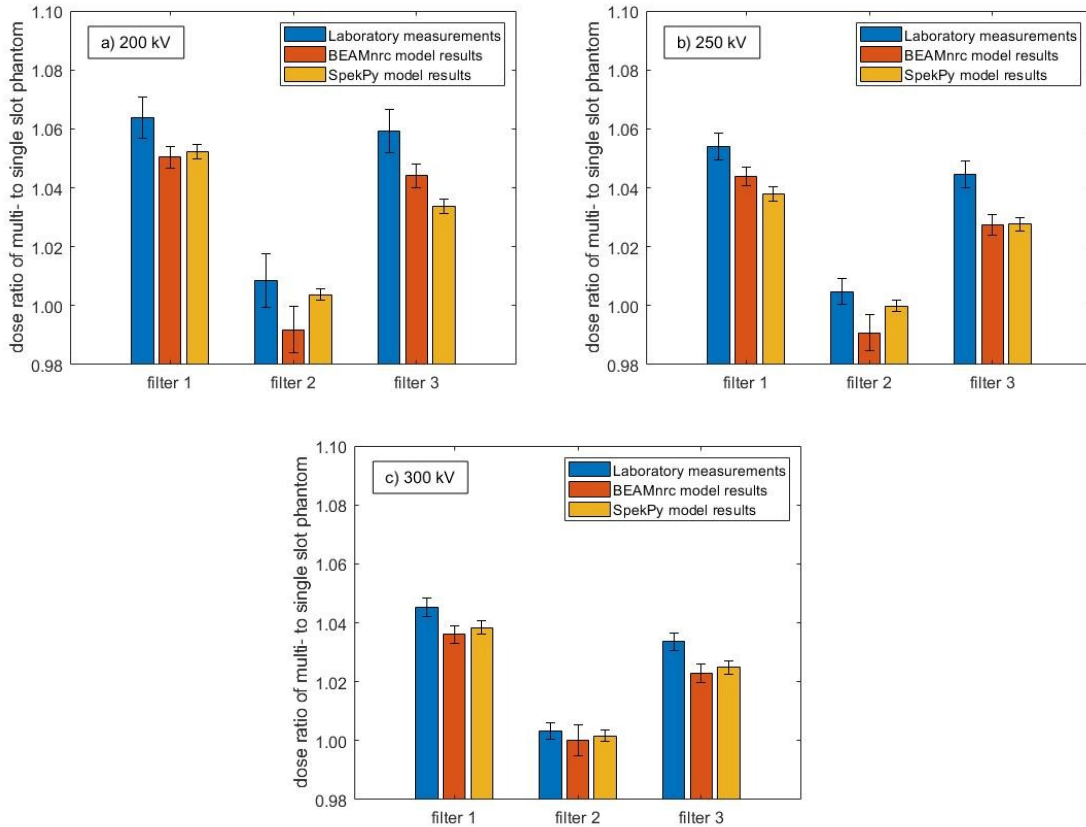


Figure 31: Validation results for phantom comparison, done for each model with each filter. Phantom comparison done for three different energies: a) 200 kV, b) 250 kV, and c) 300 kV.

3.3.3. Filter Comparison

The second point of validation was a ratio of outputs with differing filtration in place, where the electrometer reading was taken with different filters with everything else held constant. The multi-slot phantom was used with an energy of 250 kV. A ratio was taken

between readings with each of the three filters previously described and the reading output with no filtration in place using Equation 18.

$$\text{Ratio} = \frac{\text{Reading Output with Filter (1, 2, or 3)}}{\text{Reading Output with no filter}} \quad (18)$$

Figure 32 shows the percentage difference of the electrometer reading ratios taken in the laboratory and the dose output ratios from the BEAMnrc or SpekPy models. The points are arranged in order of level of filtration or beam hardness, going from lowest to highest. As beam hardness increases, the discrepancy between the simulation and laboratory increases significantly, reaching over 15% in the case of SpekPy for filter 2. Overall a large discrepancy is seen between laboratory and both simulations, even for the filter with the best agreement filter 1, the discrepancy is relatively large compared to the errors at 2%.

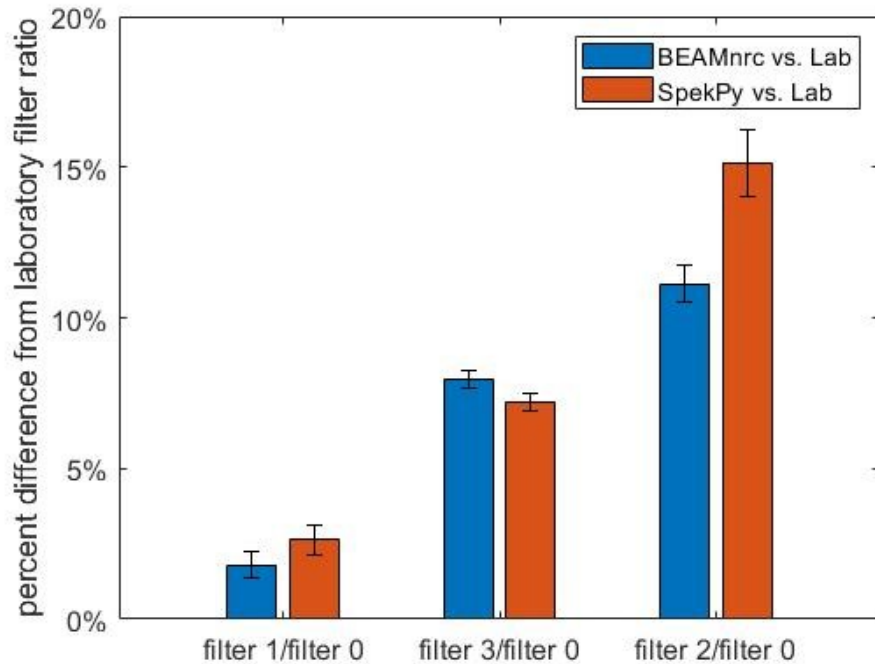


Figure 32: Percentage difference between simulations and laboratory measurements for three filters normalized to the output with no filter in place for both the BEAMnrc and SpekPy models.

3.3.4. HVL Comparison

The final set of data used to validate the EGSnrc models is the determination of the HVL of copper. To calculate the HVL from the laboratory and each of the simulations being considered, an attenuation curve was created and displayed in **Figure 33**. Each value graphed was normalized to the output measured or calculated with only filter 1 in place and no copper filtration and fit with a cubic spline function in MATLAB R2021b. Using this fit to calculate the HVL value produces a thickness of 0.5931 mm for the laboratory measurements, 0.5711 mm for the BEAMnrc model data, and 0.5635 mm for the SpekPy model data. The BEAMnrc HVL differed from the laboratory by 3.71%, while the SpekPy HVL differed by 4.99%. Looking at the curves themselves, it appears to that in general, laboratory measurements predict a higher output until the thicknesses of copper get over 1.5 mm, then the simulations predict a higher dose.

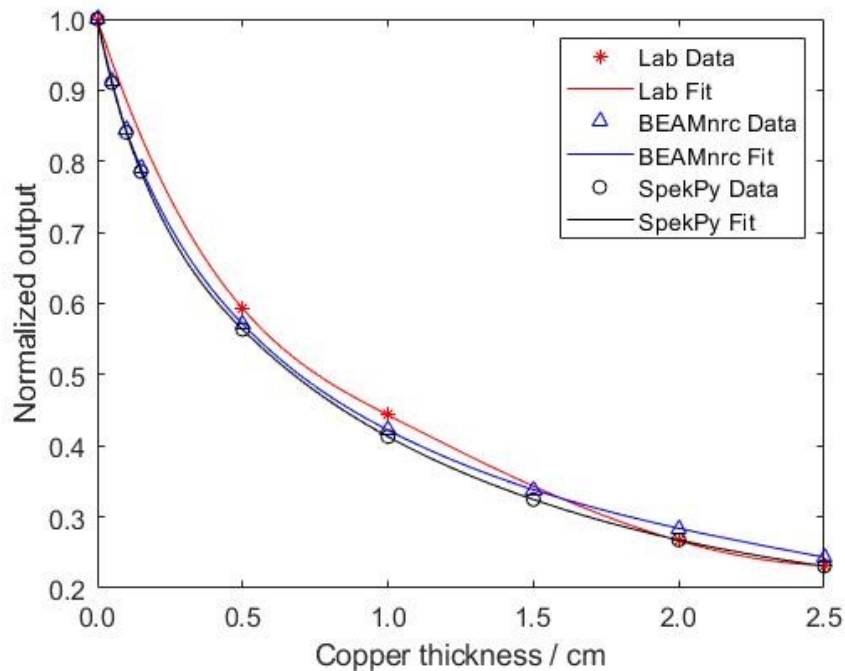


Figure 33: Attenuation curve plotted for copper to compare laboratory measurements to MC model output. Each set of points was fit using a cubic spline in MATLAB R2021b and the HVL was calculated for each curve. Error bars too small to be visualized.

4. Discussion

4.1. Choosing Variance Reduction Parameters

The validation of these MC models required many long simulations to be run, therefore the analysis of the efficiency gain and the influence of each technique on the dose was an important consideration. Choosing a perfectly optimal set of parameters was not necessarily required; the main goal was instead to reduce the simulation time to a reasonable value while still producing acceptable uncertainties on calculated values. In general, simulations times of 4-6 hours were sought along with an uncertainty below 0.5%. Simulation times for these high-precision simulations could be heavily reduced by clever implementations of the VRTs but in the case of some of these simulations, further reduction of simulation time was required. This was done through parallel processing on the Carleton computing cluster, as discussed previously in Section 2.4. The combination of VRTs and parallel processing allowed for all SpekPy and BEAMnrc model simulations to be run in a reasonable amount of time while producing an acceptable uncertainty.

A few considerations went into choosing the parameters used for each VRT including the amount of efficiency gained, the additional computational time incurred, and the effect on the output dose value. The amount of efficiency gained was used to gauge whether the VRT was worth implementing. Computational time added was tracked to ensure that the simulation could still be run in a reasonable amount of time. Finally, the dose tracking proved important because it served a dual purpose: it allowed the visualization of which factor was affecting the efficiency and thus allowed the determination of whether each VRT was affecting the computational time, uncertainty, or both, and it provided a way to ensure that the dose would remain relatively unchanged after a VRT was implemented.

4.1.1. Range-based RR and XCSE

Since both models considered for validation end in *egs_chamber*, there were two VRTs that could always be applied, XSCE and range-based RR. These two techniques were optimized separately to evaluate their individual efficiency improvement capabilities to be combined in the final simulation set. The separate optimization, however, failed to consider that for the particle weights to work out properly when the two VRTs interact, the rejection factor must be equal to or larger than the enhancement factor in a given region. Therefore, while optimization of both techniques simultaneously was important, the one that provided the most efficiency gain should take precedence in determining the “minimum” value that either the enhancement or rejection factor could be.

The optimizing range rejection in the preliminary testing phase showed efficiency gains of around 2-3 times compared to the simulation with no VRTs. In terms of the dose output, it remained relatively statistically consistent through each simulation as compared to the no VRT case, but the fluctuation in dose for some rejection factors was non-negligible and thus needed to be considered when choosing a rejection factor as well as implementing the VRT in general. In addition, when examining the dose output tracking graph, it was noted that the uncertainty did not change much from factor to factor so it was evident that the variable that was being improved by range-based RR was the computational time. This aligned with expectations as the removal of excess electrons being tracked outside the region of interest would mean the simulation has fewer computationally expensive electrons to track through the rest of the simulation, resulting in a decrease of computational time. As the rejection factors increased, the relative efficiency decreased back down to unity and remained there. This could be explained by minimal electrons being produced outside the cavity region with

enough energy to be relevant to the output dose so an increase to the rejection factor past a certain point would have no effect. This would also explain the relatively small efficiency gains seen from this technique compared to others in these simulations. Optimizing XCSE showed much better efficiency gains, with the maximum relative efficiency gain reaching values of 138. The dose output was consistent through all the simulations, but notably, the uncertainty on the simulation with no VRT was much larger than the rest. As the enhancement factor increased, the uncertainty was found to decrease drastically, indicating that this VRT affected the uncertainty, and the computational time was found to increase as the factor increased. Therefore, when optimizing XCSE, it was a balancing act between the best uncertainty and computational time. Based on the fit to the data, this was expected to occur at an enhancement factor of 677. The simultaneous increase in computation time and decrease in uncertainty was due to the large number of additional photons being produced in the enhanced region. Despite photons being relatively inexpensive to transport, the number of calculations required for dose being deposited in that region still increased the computational time in a non-negligible way. At a certain point, efficiency started to decrease because more and more photons were being produced at higher enhancement factors but provided less and less additional information. This resulted in a steady increase in the computational time but a decrease in the rate of reduction of the uncertainty. After the preliminary phase of testing for the initial design of the geometry, it was concluded that range-based RR was not required and solely XCSE would be used. If the rejection factor were to be set higher than enhancement factors that produce near maximum efficiency, there would be no effect seen from range-based RR.

In the final testing phase, the optimization of both VRTs changed slightly to reflect the change in geometry. Range-based RR showed similar efficiency gains but was found to not drop off at high rejection factors. In fact, the relative efficiency was sometimes larger for some

large rejection factors. With the addition of the steel stage, and the use of the single-slot phantom instead of the multi-slot phantom in the simulation, many more electrons would be produced near the region of interest. Therefore, it would make sense that this VRT would still have an effect at large rejection factors. Notably, no clear trend was seen to allow a fit for this new set of data, so the factor had to be chosen more carefully by considering the efficiency gains recorded. The factor that showed the largest efficiency gain was 2,048, so this was considered the new “optimal” factor; looking at the VRT in a broader sense, this also supports use of larger rejection factors to match enhancement factors. As for the final testing phase for XCSE, the efficiency gains appeared to be moderately larger for this new geometry, and the optimal factor was predicted to be larger. Based on the fit, an enhancement factor of 1,388 was expected to produce a maximum relative efficiency of 319, almost 2.3 times larger than the maximum from the preliminary phase. Notably, the efficiency curve remained relatively flat from a factor of 512 to around 1,024 with no significant increase, so a selection of an enhancement factor in this range would suffice. The main conclusions made from the final phase of optimizations was that a higher enhancement factor would provide larger efficiency gains, and range-based RR could be reintroduced because high rejection factors could be used.

4.1.2. Bremsstrahlung Splitting

The most important VRT to optimize for the egs++ model was bremsstrahlung splitting. Without this VRT in place, the uncertainties on calculated values would be unreasonably high, and the spectra produced would be inaccurate and unreliable. From the preliminary phase of optimization, bremsstrahlung splitting was found to be unreliable in terms of the effect it had on the dose output. A large point of concern with this technique was the large difference between doses calculated with and without the VRT. As stated previously,

for the final testing phase the ECUT in the regions around the X-ray tube were set back to the global ECUT value. This rectified the discrepancy in calculated dose values at the cost of a notable increase in the overall simulation time. In addition, the relative efficiency gains were also found to be larger with this setting change and the new geometry. The general trend found in both phases of testing was that the efficiency increased rapidly as the splitting number increased and reached a maximum. The efficiency then decreased rapidly and at large values this decrease slowed down. After a certain point, the relative efficiency dropped below 1, indicating that the simulation had become less efficient when using this VRT. This was because, after a certain point, the rate at which uncertainty decreased from the increase in number of photons from the X-ray tube became smaller than the rate at which the computational time increased. Large splitting numbers provide very good uncertainty values but at the cost of large computation times, so much so that using a lower splitting number and increasing the number of histories in the simulation was more efficient. This was also exemplified by the large decrease in error bars that were noted in the dose tracking graphs as the splitting number increased. In addition, one thing to consider was that unlike directional bremsstrahlung splitting, the bremsstrahlung events that were occurring in other locations the X-ray tube geometry were being split as well. This could cause an increase in computation time that was not accompanied by a decrease in the uncertainty as these photons might not reach the sensitive region of the ionization chamber. A potential solution to this could be to consider using the region-by-region ECUT setting in a more careful manner than the application here and place some shielding to get rid of excess photons that do not need to be tracked.

4.1.3. DBS and BSCE

Using the procedure recommended in the BEAMnrc manual, the optimal parameters for both BCSE and DBS were found. From the calculation done using the fit parameters, the optimal N_{split} for DBS was found to be 244. The dose was tracked alongside each factor and the uncertainty was found to increase with increasing directional splitting number but the computational time drastically decreased. Therefore, using both of these VRTs in conjunction produced large gains in efficiency, so much so that it was difficult to determine the point of normalization that was typically used. Fortunately, the method to calculate the optimal splitting value N_{split}^{opt} does not require a normalized MC efficiency. Based on a smaller simulation, a run with no VRT using the same number of histories used to produce the other runs ($1 \cdot 10^5$) would take over 91 hours. While the efficiency cannot be calculated from the computational time alone, it does serve as a good point of discussion. When N_{split} was set to lowest value used in the analysis of 1, the computational time was 3,582 seconds, a factor of 90 smaller than the estimated case with no VRTs. The time also further reduced to less than 15 seconds with a splitting number of 500, which was a reduction in computational time of over 20,000 fold. This may seem unreasonably large but one must consider that this again does not translate directly to efficiency and once the increase in uncertainty was considered, the relative efficiency would be smaller, but still substantial. Especially when compared to its much weaker counterpart in the egs++ model, this VRT provided significant efficiency improvements to the BEAMnrc model.

4.1.4. Optimized Models

Based on all the efficiency curves seen throughout the model optimization, it is apparent that the proper selection of variance reduction parameters is quintessential to maximizing the potential of each VRT. In some cases, these VRTs are the only reason these simulations can produce usable dose outputs in a reasonable amount of time. Despite the emphasis on determining the exact optimal parameter for each VRT, in reality the exact value used was not important as long as it is relatively close to the optimal value. This could be seen by examining most of the efficiency curves where the curve plateaued near the point of maximum efficiency. Therefore, a range of parameter values surrounding the maximum value could be used to provide efficiency gains close to the maximum efficiency. The optimal values calculated from the preliminary and final phases of testing were summarized in the second column of **Table 2**, and the values implemented in the code used to produce the validation results are listed in the third column of the table. For the most part, the exact optimal values calculated were not used. With range-based RR, from the final phase of testing, the value that produced the highest efficiency was 2,048, but instead a value of 512 was used to match the XCSE factor. This was due to the final phase of testing the RR VRT being incomplete as the validation simulations were being run and a factor of 512 providing sufficient efficiency gains. This leads to the reasoning for the choice of 512 for the enhancement factor in XCSE. This value was chosen based on the recommendation of a researcher knowledgeable of the inner workings of EGSnrc who recommended the factor be a power of 2 (Dr. Martin Martinov, personal communication, December 2nd 2021). The final phase of XCSE testing did find a much larger value for the enhancement factor, but this factor was again chosen prior to the completion of the final phase of optimization and was found to provide sufficient gain in the new geometry to continue with. As stated earlier, the efficiency gain reached a plateau around

this value in the preliminary phase of testing and a little higher in the final phase but 512 still provided a good efficiency gain compared to the maximum. For the bremsstrahlung splitting VRT, the splitting number was set to 100 as found in the preliminary phase of testing, but the model was not able to produce a good uncertainty value. In the end, the egs++ model, which provided the most geometrical accuracy, was dropped because of an unknown interaction between the VRTs that was causing random spikes in the uncertainty that made simulations unreliable and the desired uncertainty unreachable for any of the egs++ simulations. The final two VRTs, DBS and BCSE, only had one parameter to be optimized when combined as the other could be determined from the literature. The optimal value for DBS was found to be 244 but 1,000 was used in the simulations run for validation. This was a preliminary value that was found to provide good efficiency through initial testing so it was used in place of the optimal value until the optimization analysis was completed. Further simulations required when moving forward to produce the phase space files will implement the optimized value.

4.2. Spectral Comparison between Models

Before validation can be performed, it was important to first ensure consistency between all the models. This inter-model comparison was conducted by means of a comparison of the photon spectrum produced at the same point from each model. One general note that could be made for all the spectral comparisons is that on a large scale, the spectra were consistent throughout. This is true from the model of just the X-ray tube as well as with increasing levels of filtration. In addition, the spectra produced match expectations well. In the spectrum from just the X-ray tube, the K-shell and L-shell emission lines can be seen at the expected energies for a thick tungsten target [51], [52]. The effects from the increasing levels of filtration are also within expectations. Moving to filters with greater

absorption (filter 1 → filter 3 → filter 2), the lower energies should be selectively filtered out, resulting in an overall higher energy spectrum. The intensity of the beam would also be reduced accordingly but since these are comparisons between normalized spectra, this reduction was not immediately apparent. Some differences were noted between the spectra were magnified when looking at subtracted spectra for each energy and level of filtration. For the most part, differences were seen in the magnitude of the characteristic peaks for the K-shell (and L-shell for some cases) emission lines, as well as in general at low energies. Considering the percentage of the spectrum that these peaks make up, these differences should be noted but not a source of concern.

For the SpekPy model, the spectrum itself was extremely important as it determined the performance and accuracy of the model. For all spectra, and all simulations performed in general, particles were considered down to an energy of 1 keV and this was an area where discrepancies were seen. An inaccurate spectrum at these low energies would not directly affect the dose output as these low energy photons would not be contributing much energy deposition. Where this discrepancy had an effect is due to this part of the spectrum taking up a certain portion of the fluence, reducing the overall intensity of the beam, resulting in a lower dose output. This could be tested by simply cutting off the spectrum at a higher value and using that spectrum for the SpekPy model. When so tested, such a spectrum was indeed found to produce higher dose outputs. Therefore, the energy at which the spectrum was cut off was an important factor to consider when using the SpekPy model in addition to the actual cut-off energy for photons in the simulation. For the simulations considered for validation, the full spectrum down to 1 keV was used, but as displayed earlier, the dose was underestimated by both the SpekPy and BEAMnrc models, and this might be a potential source of this underestimation.

4.3. Model Validation

Once the models were compared and verified to produce relatively similar spectra, the next step was to validate these models with laboratory data. Overall, the results from all three types of validation revealed some errors in the BEAMnrc and SpekPy models. Notably, for the validation against laboratory measurements, the choice was made to exclude the egs++ model. One of the main issues with this model was the large uncertainty on the uncertainties from the simulation. After a certain number of histories, the uncertainty would jump up to a much larger value, and then begin reducing again as more histories were calculated. A possible reason for this could be the presence of particles with large statistical weights, or fat particles, in the area of interest. If such a particle entered the sensitive region of the ion chamber, the uncertainty for the recorded value in that region would increase by a notable margin, which is aligned with the observations made when attempting to troubleshoot the issues with the egs++ model. Fixing this error would require tracking these fat particles to find their origin and addressing the issue from its root but this proved too time consuming to complete in this thesis work. In addition, a large number of histories was required to register a useful dose value in general so it was impractical to use for validation with laboratory measurements. Therefore, the model was used for the spectral comparison but it was excluded from validation with laboratory measurements. The reason it could be used for the spectral comparison is that a large scoring field is used to score the spectrum in *cavity*, so the issues with the uncertainties were not seen as there was no complex geometry involved.

For the validation, only ratios were used when comparing the simulated results to laboratory measurements. In general, absolute absorbed dose values can be difficult to calculate using EGSnrc. One immediate problem to consider is the fact that MC code involves

specifying the exact number of particles involved in a simulation, not the actual dose being output by the X-ray machine. It would be almost impossible to figure out exactly how many photons are reaching the ionization chamber for a given choice of X-ray tube settings. A much simpler approach to validate each model is to use ratios of measurements, eliminating the need for absolute measurements. In addition, the range of methods used for validation allowed for some troubleshooting into the discrepancies seen between these EGSnrc models and the laboratory measurements. The filter comparison allowed for an investigation of the accuracy of the XRAD-320 body geometry by changing internal components (the filter) and comparing those two states of the system. In contrast, the phantom comparison focussed on the components outside the XRAD-320, and checked whether potential errors in the body geometry would cancel out when a ratio was taken between two states of the system where the XRAD-320 body was unchanged. Finally, as the HVL measurement is a standard method of characterizing the output from an X-ray machine, it was considered an important part of the model validation.

Before discussing the validation results, it is important to first briefly discuss the errors associated with each value being considered. As mentioned previously, EGSnrc outputs a relative statistical uncertainty that scales with the number of particle histories in the simulation. For a more accurate estimate on the uncertainty of the dose calculation, other factors have to be considered outside of statistical variations. One example is the uncertainty on the interaction cross sections that EGSnrc uses for its calculations. These values have associated errors and these uncertainties would be incorporated in a more rigorous treatment of the error. Future work should consider the impact of these uncertainties and account for them in the simulation uncertainties.

4.3.1. Phantom Comparison

The first type of laboratory validation was the phantom comparison, where a ratio was taken between the doses recorded inside the multi-slot phantom and the doses inside the single-slot phantom. Based on the geometries involved, the expectation was that the ionization chamber in the single-slot phantom would measure a higher reading as it has more solid water surrounding it. This would mean a much higher probability of more photons/electrons scattering into the sensitive region of the ionization chamber and being recorded. The results for all levels of filtration, however, indicated that the opposite appeared to be the case in both the laboratory and the simulations. The main reason was found to be the difference in material composition of the slabs that made up the multi- and single-slot phantoms. As described in Section 2.1.3.2, the multi-slot phantom is composed partially of polystyrene, with the rest being RW3 solid water. The single-slot phantom, on the other hand, is completely composed of RW3. The important thing to consider with radiation beam attenuation is the electron density ratio of these materials when compared to liquid water. RW3 has a ratio of 1.010 relative to water, while polystyrene had a ratio of 1.027 [41]. From this, one would expect the phantom composed of polystyrene to register a larger reading, despite the presence of air gaps when compared to the RW3 phantom.

In general, the ratio was consistently largest for all scenarios with filter 1 and decreased with increasing levels of filtration. For filter 2, the ratio was close to 1 and all laboratory measurements and simulation results were within statistical variance. Comparing the results across energies for the different filters, the ratio was highest for 200 kV, decreased at 250 kV and decreased further for 300 kV. This trend was seen for both laboratory and simulations results. Looking at the actual values of the ratios and comparing between laboratory and

simulation results, there appeared to be a consistent discrepancy. The general trend seen for both models was that they consistently underestimated the dose output when compared to the equivalent laboratory measurements even when ratios were statistically consistent, with both models overall performing similarly but the SpekPy model yielding marginally better results. The most likely cause of the discrepancy between the simulations and laboratory measurements was an inaccuracy in the assumptions made for the specifications of the model. Mainly this included the lack of information on the spacing of the different components along the beam path, as well as not accounting for the backscatter from the enclosure between the monitor chamber and the jaws. The expectation was that the BEAMnrc model would agree better with laboratory measurements due to the much more accurate geometrical modelling of the X-ray production but this was not the result found in this study. Due to the SpekPy model originating from a point source, there would be fewer photons scattered away from the sensitive region of the ionization chamber as compared to the BEAMnrc model. This would cause an increase in the dose recorded from the SpekPy model and might explain the discrepancy seen between the models.

4.3.2. Filter Comparison

The next method of laboratory validation was the filter comparison, which involved the ratio between the readings from a filtered beam to readings with no filtration other than the inherent beryllium filter. The measurements were done for an energy of 250 kV within the multi-slot phantom. All ratios were found to be inconsistent with laboratory measurements for both the SpekPy and BEAMnrc models. This discrepancy was seen to increase with increasing levels of filtration. For filter 1, the discrepancy was around 2% for both models, which was on par with the discrepancies seen for the ratios between phantoms, but jumped

to above 10% for the highest level of filtration, filter 2. In addition, while the discrepancies were around the same for both models for filters 1 and 3, for filter 2 there was a large difference where BEAMnrc provided a much better estimate of the ratio. For filter 2, the percentage difference from the laboratory ratio for the BEAMnrc model was almost 4% smaller than the SpekPy model. This matched expectations as the BEAMnrc model is the more geometrically accurate model and therefore should better estimate the large amount of scatter from filter 2.

In general, this filter comparison provided a good test of the accuracy of the components used to build the XRAD-320 body. A large discrepancy between the ratio outputs at different levels of filtration found in the laboratory and simulated in both models could be indicative of two issues. The first being that the materials attenuating the beam and/or their thicknesses are incorrect, leading to an overall underestimation of the dose. This would result in a larger discrepancy in the more attenuating filters because if the X-rays are over or under-scattered while travelling through the XRAD-320, the filter would amplify the problem. The second possible issue could be that the model is missing the white plastic casing seen in the image of the full setup in **Figure 4** that surrounds the area between the monitor chamber and the output window for the beam. Depending on the composition of the material of this casing, it could result in enough backscatter that the dose output could be affected, increasing the overall dose recorded. Missing this component in the models could mean that the dose is being underestimated, and this would again have a greater affect the beams with higher levels of filtration.

4.3.3. Half-Value Layer (HVL) Comparison

As a final method of laboratory validation, the HVL of copper was determined for the models and compared to laboratory measurements. The attenuation data for different thicknesses of copper filtering the beam were plotted from the laboratory and each of the EGSnrc models and each data set was fit with a cubic spline function in MATLAB R2021b. It was found that the BEAMnrc HVL differed from the laboratory value by 3.71%, while the SpekPy HVL differed by 4.99%. Looking at the curves, it appeared that, in general, laboratory measurements predicted a higher output until the thicknesses of copper exceeded 1.5 mm and then the simulations predicted a higher dose. The trends with thin copper are in line with previous observations that the models underestimate the dose. To account for the trends with thicker copper, similar arguments as earlier can be made about the inaccuracies in the model with regards to backscatter and component positioning. A combination of errors could result in either an increase or a decrease in the relative dose output measured. Overall, the discrepancy in HVL calculations between laboratory and simulations is relatively larger than the discrepancies seen for the phantom output ratios. This further indicates that the issue lies within the internal geometry definitions of the XRAD-320. Comparing the accuracy of each of the models, it is clear that the BEAMnrc model is the most accurate, being almost 1.3% closer to the laboratory measurement.

5. Conclusion

5.1. The Best Model

Three different Monte Carlo models of the irradiation setup used at Health Canada to irradiate blood samples for biodosimetry were presented in this thesis. The models were validated through an inter-model comparison, followed by a comparison to laboratory measurements of a few quantities of interest. Comparing the spectra between each model showed good agreement across all models. For the validation with laboratory measurements, the egs++ model was excluded as it was not able to produce outputs with acceptable uncertainty values. Based on the results presented in this thesis, the BEAMnrc model was determined to be the best model. It matched egs++ well in the spectral comparison, provided the best results in the filter comparison and the HVL calculation, and performed similarly to the SpekPy model in the phantom comparison. Overall, it provided better efficiency gains as compared to egs++ as well as more efficient simulation times, and is more representative of the real-life scenario of the scattering from the X-ray tube than the SpekPy model. While there is still a relatively small issue with underestimation of the output as compared to laboratory measurements, the BEAMnrc model has been determined to be the optimum MC model of the X-RAD 320 cabinet X-ray system at HC.

5.2. Future Work

The discrepancy between laboratory results and simulation will be further investigated in order to identify the causes and improve the model. This will focus on accurately modelling the white plastic casing between the monitor chamber and the output window of the XRAD-320 by acquiring information from the manufacturer. In addition, the internal contents will be further verified to ensure that nothing attenuating the beam was excluded from the model.

Once the BEAMnrc model produces favorable results within error of the laboratory results, the output of the simulation can be saved in the form of a phase space file, which records the phase space information of all particles in a given area. This can replace the entire BEAMnrc source and further improve simulation times.

As the project moves forward, the focus will shift to radiobiology as the calibration curves for the laboratory can be produced using the results from the EGSnrc simulation as the source. To do this, another software capable of doing radiobiological simulations will be used to calculate the biological damage needed to generate calibration curves. There are many MC softwares for modelling biological responses to radiation but one of interest is TOPAS-nBio. It is similar to EGSnrc in that it only requires proper creation of input files to run simulations. The phase space files produced by BEAMnrc can be used as a source in TOPAS nBio. In addition, to produce a space-equivalent calibration curve, the radiation environment in space must be modelled. Finally, by comparing the biological damage from the X-ray irradiations to those from the space radiation environment, X-ray equivalent dose estimates can be converted to the true dose received by the astronauts during their mission.

6. References

- [1] S. J. McMahon, J. Schuemann, H. Paganetti, and K. M. Prise, “Mechanistic Modelling of DNA Repair and Cellular Survival Following Radiation-Induced DNA Damage,” *Scientific Reports*, vol. 6, no. 1, pp. 1–14, 2016.
- [2] E. J. Hall and A. J. Giaccia, *Radiobiology for the radiologist*, 7 ed Lippincott Williams & Wilkins, 2012.
- [3] M. T. Sproull, K. A. Camphausen, and G. D. Koblentz, “Biodosimetry: A Future Tool for Medical Management of Radiological Emergencies,” *Health Security*, vol. 15, no. 6, pp. 599–610, 2017.
- [4] M. Satyamitra, F. E. Reyes Turcu, N. Pantoja-Galicia, and L. Wathen, “Challenges and Strategies in the Development of Radiation Biodosimetry Tests for Patient Management,” *Radiation Resesarch*, vol. 196, no. 5, pp. 455–467, 2021.
- [5] E. A. Ainsbury *et al.*, “Review of retrospective dosimetry techniques for external ionising radiation exposures,” *Radiation Protection Dosimetry*, vol. 147, no. 4, pp. 573–592, 2011.
- [6] International Atomic Energy Agency, “Cytogenetic Dosimetry: Applications in Preparedness for and Response to Radiation Emergencies,” IAEA, Vienna, 2011.
- [7] G. A. Alsbeih, K. S. Al-Hadyan, N. M. Al-Harbi, S. S. Bin Judia, and B. A. Moftah, “Establishing a Reference Dose–Response Calibration Curve for Dicentric Chromosome Aberrations to Assess Accidental Radiation Exposure in Saudi Arabia,” *Frontiers in Public Health*, vol. 8, 2020.
- [8] A. A. Edwards, “The use of chromosomal aberrations in human lymphocytes for biological dosimetry,” *Radiation Research*, vol. 148, no. 5 suppl., 1997.
- [9] Y. Lusiyanti, M. Syaifudin, T. Budiantari, S. Purnami, and D. Ramadhani, “Development of dose-response calibration curve for dicentric chromosome induced by X-rays,” *Genome Integrity*, vol. 10, no. 2, 2019.
- [10] T. H. Ryu, J. H. Kim, and J. K. Kim, “Chromosomal aberrations in human peripheral blood lymphocytes after exposure to ionizing radiation,” *Genome Integrity*, vol. 7, no. 1, pp. 3–5, 2016.
- [11] P. G. S. Prasanna *et al.*, “AFRRI’s Gamma-Ray, X-Ray, and Fission-Neutron Calibration Curves for the Lymphocyte Dicentric Assay: Application of a Metaphase Finder System,” *Armed Forces Radiobiology Research Institute*, 2002.
- [12] B. Yao *et al.*, “Estimation of the biological dose received by five victims of a radiation accident using three different cytogenetic tools,” *Mutation Research/Genetic Toxicology Environmental Mutagenesis*, vol. 751, no. 1, pp. 66–72, 2013.
- [13] F. N. Flegal, Y. Devantier, L. Marro, and R. C. Wilkins, “Validation of QuickScan dicentric chromosome analysis for high throughput radiation biological dosimetry,” *Health Physics*, vol. 102, no. 2, pp. 143–153, 2012.
- [14] A. Vaurijoux *et al.*, “Strategy for population triage based on dicentric analysis,” *Radiation*

Research, vol. 171, no. 5, pp. 541–548, 2009.

- [15] Q. J. Liu *et al.*, “Assessment of retrospective dose estimation, with fluorescence in situ hybridization (FISH), of six victims previously exposed to accidental ionizing radiation,” *Mutation Research/Genetic Toxicology Environmental Mutagenesis*, vol. 759, pp. 1–8, 2014.
- [16] V. S. T. Goh *et al.*, “Construction of fluorescence in situ hybridization (FISH) translocation dose-response calibration curve with multiple donor data sets using R, based on ISO 20046:2019 recommendations,” *International Journal of Radiation Biology*, vol. 95, no. 12, pp. 1668–1684, 2019.
- [17] J. F. Barquinero, G. Stephan, and E. Schmid, “Effect of americium-241 α -particles on the dose-response of chromosome aberrations in human lymphocytes analysed by fluorescence in situ hybridization,” *International Journal of Radiation Biology*, vol. 80, no. 2, pp. 155–164, 2004.
- [18] L. A. Beaton-Green, S. Lachapelle, U. Straube, and R. C. Wilkins, “Evolution of the Health Canada astronaut biodosimetry program with a view toward international harmonization,” *Mutation Research/Genetic Toxicology Environmental Mutagenesis*, vol. 793, pp. 101–106, 2015.
- [19] W. Schimmerling, “The space radiation environment: an introduction,” *NASA Technical Paper*, 2011.
- [20] L. C. Simonsen, T. C. Slaba, P. Guida, and A. Rusek, “NASA’s first ground-based galactic cosmic ray simulator: Enabling a new era in space radiobiology research,” *PLoS Biology*, vol. 18, no. 5, 2020.
- [21] S. Trovati *et al.*, “Human exposure to space radiation: role of primary and secondary particles,” *Radiation Protection Dosimetry*, vol. 122, no. 1–4, pp. 362–366, 2006.
- [22] I. Getslev, S. Rumin, N. Sobolevsky, M. Ufimtsev, and M. Podzolko, “Absorbed dose of secondary neutrons from galactic cosmic rays inside the International Space Station,” *Advances in Space Research*, vol. 34, no. 6, pp. 1429–1432, 2004.
- [23] U. Kulka *et al.*, “Biodosimetry and biodosimetry networks for managing radiation emergency,” *Radiation Protection Dosimetry*, vol. 182, no. 1, pp. 128–138, 2018.
- [24] B. Hidding *et al.*, “Laser-plasma-based Space Radiation Reproduction in the Laboratory,” *Scientific Reports*, vol. 7, no. 1, pp. 1–6, 2017.
- [25] J. W. Norbury *et al.*, “Galactic cosmic ray simulation at the NASA Space Radiation Laboratory,” *Life Sciences in Space Research*, vol. 8, no. 8, pp. 38–51, 2016.
- [26] P. Andreo, “Monte Carlo simulations in radiotherapy dosimetry,” *Radiation Oncology*, vol. 13, no. 1, pp. 1–15, 2018.
- [27] I. Kawrakow, D.W.O. Rogers, E. Mainegra-Hing, F. Tessier, R. W. Townson, B.R.B. Walters. EGSnrc toolkit for Monte Carlo simulation of ionizing radiation transport, doi:10.4224/40001303, [release v2020] 2000.
- [28] D. W. O. Rogers, “Fifty years of Monte Carlo simulations for medical physics,” *Physics*

in Medicine and Biology, vol. 51, no. 13, 2006.

- [29] A. F. Bielajew, H. Hirayama, W. R. Nelson, and D. W. O. Rogers, “History , overview and recent improvements of National Laboratory for High Energy Physics National Research Council of Canada,” *Technical Report*, PIRS-0436 (National Research Council of Canada), 1993.
- [30] I. Kawrakow, “Accurate condensed history Monte Carlo simulation of electron transport. I. EGSnrc, the new EGS4 version,” *Medical Physics*, vol. 27, no. 3, pp. 485–498, 2000.
- [31] I. Kawrakow, “Accurate condensed history Monte Carlo simulation of electron transport. II. Application to ion chamber response simulations,” *Medical Physics*, vol. 27, no. 3, pp. 485–498, 2000.
- [32] I. Kawrakow and D. W. O. Rogers, “The EGSnrc Code System : Monte Carlo Simulation of Electron and Photon Transport,” *Technical Report*, PIRS-701 (National Research Council of Canada), 2003.
- [33] I. Kawrakow, E. Mainegra-hing, F. Tessier, R. Townson, and B. Walters, “The EGSnrc C++ class library,” *Technical Report*, PIRS-898 (National Research Council of Canada), 2011.
- [34] D. W. O. Rogers, B. Walters, and I. Kawrakow, “BEAMnrc Users Manual,” *Technical Report*, PIRS-0509(A)revL (National Research Council of Canada), 2021.
- [35] D. W. O. Rogers, B. A. Faddegon, G. X. Ding, C. M. Ma, J. We, and T. R. Mackie, “BEAM: a Monte Carlo code to simulate radiotherapy treatment units,” *Medical Physics*, vol. 22, pp. 503–523, 1995.
- [36] J. Wulff, K. Zink, and I. Kawrakow, “Efficiency improvements for ion chamber calculations in high energy photon beams,” *Medical Physics*, vol. 35, no. 4, pp. 1328–1336, 2008.
- [37] E. Ali, “Making the EGSnrc/BEAMnrc system more efficient, accurate and realistic in simulating kilovoltage x-ray systems,” MSc Dissertation, Carleton University, 2007.
- [38] D. Sheikh-Bagheri, I. Kawrakow, B. Walters, and D. W. O. Rogers, “Monte Carlo Simulations: Efficiency Improvement Techniques and Statistical Considerations,” *Integrating New Technologies into the Clinic: Monte Carlo and Image-Guided Radiation Therapy - Proceedings of 2006 AAPM Summer School*, pp. 71–91, 2006.
- [39] I. Kawrakow, D. W. O. Rogers, and B. R. B. Walters, “Large efficiency improvements in BEAMnrc using directional bremsstrahlung splitting,” *Medical Physics*, vol. 31, no. 10, pp. 2883–2898, 2004.
- [40] E. S. M. Ali and D. W. O. Rogers, “Efficiency improvements of x-ray simulations in EGSnrc user-codes using bremsstrahlung cross-section enhancement (BCSE),” *Medical Physics*, vol. 34, no. 6, pp. 2143–2154, 2007.
- [41] A. A. Schoenfeld, D. Harder, B. Poppe, and N. Chofor, “Water equivalent phantom materials for 192Ir brachytherapy,” *Physics in Medicine & Biology*, vol. 60, no. 24, pp. 9403–9420, 2015.

- [42] R. Azimi, P. Alaei, E. Spezi, and S. K. Hui, “Characterization of an orthovoltage biological irradiator used for radiobiological research,” *Journal of Radiation Research*, vol. 56, no. 3, pp. 485–492, 2014.
- [43] R. Pidikiti *et al.*, “Dosimetric characterization of an image-guided stereotactic small animal irradiator,” *Physics in Medicine & Biology*, vol. 56, no. 8, pp. 2585–2599, 2011.
- [44] J. Lee and S. Ye, “Development of Graphene Ion-Chamber for Radiation Dosimetry,” *Proceedings of the KNS 2016 Autumn Meeting*, 2016.
- [45] G. Poludniowski, A. Omar, R. Bujila, and P. Andreo, “Technical Note: SpekPy v2.0—a software toolkit for modeling x-ray tube spectra,” *Medical Physics*, vol. 48, no. 7, pp. 3630–3637, 2021.
- [46] R. Bujila, A. Omar, and G. Poludniowski, “A validation of SpekPy: A software toolkit for modelling X-ray tube spectra,” *Physica Medica*, vol. 75, no. February, pp. 44–54, 2020.
- [47] A. Omar, P. Andreo, and G. Poludniowski, “A model for the energy and angular distribution of x rays emitted from an x-ray tube. Part I. Bremsstrahlung production,” *Medical Physics*, vol. 47, no. 10, pp. 4763–4774, 2020.
- [48] A. Omar, P. Andreo, and G. Poludniowski, “A model for the energy and angular distribution of x rays emitted from an x-ray tube. Part II. Validation of x-ray spectra from 20 to 300 kV,” *Medical Physics*, vol. 47, no. 9, pp. 4005–4019, 2020.
- [49] A. Omar, P. Andreo, and G. Poludniowski, “A model for the emission of K and L x rays from an x-ray tube,” *Nuclear Instruments and Methods in Physics Research Section B: Beam Interactions with Materials and Atoms*, vol. 437, no. 15, pp. 36–47, 2018.
- [50] M. J. Berger, J. S. Coursey, M. A. Zucker, et al., “ESTAR, PSTAR, and ASTAR: computer programs for calculating stopping-power and range tables for electrons, protons, and helium ions (version 1.21),” 1999.
- [51] P. Andreo, D. Burns, A. Nahum, J. P. Seuntjens, and F. Attix, *Fundamentals of ionizing radiation dosimetry*, John Wiley & Sons, 2017.
- [52] E. B. Podgorsak, *Radiation Physics for Medical Physicists*, Springer, 2006.